Post-beamforming Filtering for Enhanced Contrast Resolution in Medical Ultrasound

A DISSERTATION
SUBMITTED TO THE FACULTY OF THE GRADUATE SCHOOL
OF THE UNIVERSITY OF MINNESOTA
BY

Yayun Wan

IN PARTIAL FULFILLMENT OF THE REQUIREMENTS
FOR THE DEGREE OF
Doctor Of Philosophy

Dr. Emad S. Ebbini, Adviser

October, 2010

Acknowledgements

I would like to express my deepest gratitude to my advisor Prof. Emad S. Ebbini who introduced me to the fascinating field of medical ultrasound imaging. He has been so supportive all through the years in the coursework, research and various professional trainings for PhD study. Without him, I do not think I could have accomplished so much in my PhD study.

I am also thankful to Prof. Mostafa Kaveh, Prof. Ahmed Tewfik, Prof. James Leger and Prof. Taner Akkin for serving on my oral exam committee and final defense committee, reviewing my thesis as well as giving helpful comments and suggestions.

I appreciate all the help from many lab colleagues. I would like to thank: Dr. Dalong Liu for his guidance and help in data acquisition of ultrasound imaging system and various algorithm implementation aspects such as CUDA programming for GPU; Mr. John Ballard for his help and corporation on experiment setup; Mr. Andrew Casper for his help on Matlab MEX programming setup and the presentation of the poster in Ultrasonic Symposium 2009.

This work was funded by NIH grant HL 071538 from NHBLI and NIH grant EB 006893 from NIBIB. I would also like to thank the Minnesota Supercomputing Institute for Advanced Computational Research for their support of supercomputing resources for our simulation work and data analysis.

Dedication

To those who held me up over the years

Abstract

This thesis research addresses the use of post-beamforming pseudoinverse filtering algorithms for restoring contrast resolution in pulse-echo medical ultrasound imaging. Limited contrast resolution is probably the single most important limitation of ultrasound compared with leading medical imaging modalities. While speckle is a major contributor to the loss of contrast resolution, other significant contributors are low SNR and reverberations. We have investigated the use of coded excitation, together with a 1D post-beamforming pseudoinverse filter, in improving the SNR and reducing reverberation leading to enhanced contrast resolution, especially for deeper target. Experimental demonstration of the algorithm was carried out on a dual-mode ultrasound array (DMUA) prototype intended for use in image-guided noninvasive surgery [1]. We have successfully used coded excitation with receive pseudoinverse filtering to improve the resolution about 30% while maintaining the signal to noise ratio, reducing reverberation artifact. In addition, this result in conjunction with other techniques such as spatial directivity and gain compensation significantly improve the imaging field of view of the DMUA system.

With the advent of digital beamforming in array imaging, coarse aperture sampling is identified as another significant contributor to the loss of contrast resolution, especially in high frequency ultrasound (HFUS) imaging applications. This loss results from well-known beamforming artifacts (e.g. grating lobes), which produce "filling effects" in low-contrast targets (e.g. cysts and blood vessels). To address this issue, a 2D post-beamforming filtering approach was formulated from a discretized model of the transmit-receive 2D wavefront resulting from a given beamforming operation. This 2D filter operates on a collection of beamformed A-lines (e.g. from a linear array) with coefficients obtained from the regularized inversion of the 2D Fourier transform of the 2D

point spread function of the array. This is highly significant due to the fact that direct inversion of the imaging matrix for a typical HFUS imaging scenario requires on the order of 100T flops. This was enabled by deriving the imaging operator on a 2D Cartesian grid which, under realistic simplifying assumptions, was shown to be represented by a matrix with a Toeplitz-block block Toeplitz (TBBT) structure. The dimensions of the TBBT are extremely large, which renders the direct inversion impractical, both in terms of memory requirements and number of operations. However, the large TBBT matrix has an asymptotically equivalent Circulant-block block Circulant (CBBC) matrix with equivalent eigenvalues. The CBBC is easily inverted using a finite-size 2D discrete Fourier Transform. Not only is this approach computationally efficient, it also results in a robust, physically meaningful regularized inversion. In particular, the approach transforms a usually ill-posed inverse problem to a well-posed filtering problem in k-space (through a 2D FFT). An important result from this study is that the spatial and contrast resolutions vary monotonically with the regularization parameter, β. This result is of practical significance as it allows for the selection of the optimal value of β in much the same way as time gain compensation, *e.g.* slider or dial. Using FIELD®, we present simulation data to demonstrate the tradeoff between contrast and spatial resolution. The results demonstrate the well-behaved nature of the point spread function (PSF) with the variation in a single regularization parameter. This characteristic of the pseudoinverse filter enables a parameter-controlled and more importantly, user-controlled imaging performance. These results are supported by image reconstructions from a simulated cyst phantom obtained using a finely sampled array and a coarsely sampled array. These results are also verified by image reconstructions obtained from Sonix RP system imaging a quality assurance phantom with contrast targets, optical nerve head in porcine eye *in vitro* and human carotid artery *in vivo*.

Contents

Acknowledgements **i**

Dedication **ii**

Abstract **iii**

List of Tables **ix**

List of Figures **x**

1 Introduction **1**

1.1 Ultrasound Imaging: A Historical Overview 1

1.2 Current Status 2

1.3 The Future of Ultrasound: New Opportunities and New Challenges . . . 3

1.4 Scope of the Thesis Research 4

1.5 Spatio-temporal Wavefronts and k-space Analysis 6

1.6 Contributions of this Thesis Research 7

1.7 Applications 8

1.8 Organization of the Thesis 9

2 Post-Beamforming Pseudoinverse Filter **10**

2.1 Introduction 10

2.2 System Model 11

2.3 1D PIO Filter 14

2.4 Structure Properties 16

2.5 Circulant-Block Block Circulant Matrix Approximation 17
2.5.1 Asymptotically Equivalent Circulant Matrices 17
2.5.2 Asymptotically equivalent CBBC Matrices 18
2.6 Inversion of the CBBC Matrix and Derivation 19
2.6.1 Diagonalize the Circulant Blocks 19
2.6.2 Block-Diagonalize the Block Circulant Matrix 20
2.6.3 k-Space Inverse Filtering 21
2.6.4 Inverse 2D FFT 21
2.7 2D PIO Design 22
2.8 The 2D PIO Filter in Spatial-Temporal Form 23
2.9 The Implemented Filtering Algorithm with GUI 27
2.10 Summary 27

3 Enhanced Image Resolution of DMUA **30**
3.1 Introduction 30
3.2 DMUA Prototype 33
3.3 Coded Excitation 34
3.3.1 Coded Waveforms 36
3.3.2 Receive Filter 37
3.4 1D Post-Beamforming PIO Filter Design for Coded Excitation 38
3.5 Simulation and Experiment Setup 40
3.5.1 Simulation Models 40
3.5.2 Experiment Data Collection 40
3.5.3 Imaging Targets 41
3.5.4 Synthetic Aperture Imaging 41
3.6 Assessment of Imaging Performance 43
3.6.1 Spatial Resolution 43
3.6.2 Contrast 44
3.7 Results 44
3.7.1 Verification of Simulation Model Using Wire Target Array 44
3.7.2 Special Considerations 44
3.7.3 Coded Excitation Results Using 1D Pseudoinverse Filter 51

3.8 Conclusion 55

4 Contrast Enhancement for High Frequency Ultrasound Imaging 56

4.1 Introduction 56
4.2 Simulation Results 58
4.2.1 25 MHz Small-Footprint HFUS Array Prototype 58
4.2.2 35 MHz Small-Footprint HFUS Array Prototype 75
4.3 Quality-Assurance Phantom Results 78
4.4 *In Vitro* and *In Vivo* Results 83
4.4.1 Porcine Eye *In Vitro* 83
4.4.2 Carotid Artery *In Vivo* 87
4.5 Conclusion 94

5 Conclusion and Future Work 95

5.1 Conclusion 95
5.2 Future Work 97
5.2.1 Multi-parameter regularization 97
5.2.2 Application to phased-array imaging 98
5.2.3 Combined with Coded Waveform Design 98
5.2.4 Quantitative Multi-Dimensional Vascular imaging 98

Bibliography 100

Appendix A. DMUA Transducer Design: A Simulation Study 112

A.1 Introduction 112
A.2 Transducer Bandwidth 113
A.3 Transducer Geometry 117
A.3.1 Lateral Sampling 117
A.3.2 Elevation f-number 126
A.4 Modified DMUA Design for Improved Image Quality 126
A.5 Conclusion 129

Appendix B. Simultaneous Imaging Tissue Motion and Flow Velocity in Quantitative Vascular Imaging **134**
B.1 Introduction 134
B.2 Phase-Coupled 2D Speckle Tracking 136
B.3 Results and Discussion 137
B.3.1 Data Acquisition 137
B.3.2 Strain Computation 138
B.3.3 Experimental Phantom Result for 2D Speckle Tracking 138
B.3.4 *In Vivo* Experiment 141
B.4 Conclusion 152

List of Tables

3.1 CR Values for Selected Regions. 50
3.2 Egg phantom speckle correlation cell size. 54
4.1 Contrast ratio of the images from the cyst phantom. 73
4.2 Contrast ratio of the images from the cyst phantom. 80
A.1 Cyst Diameter Measurement from Image Data. 121
A.2 CR Values for Cyst Phantom. 122
A.3 PSF Characteristics for 64- and 128-Element DMUAs. 125
A.4 PSF Characteristics for 64-Element DMUA with Different Elevation Heights. 127

List of Figures

1.1 Ultrasound array imaging system. 5

2.1 A 1D linear array system model where the scattering is assumed to result from scatters with random amplitudes on the Cartesian grid. 12

2.2 Frequency responses in k-space for generic apertures with different values of d_e: 0.5λ-4λ, f-number = 2 and fractional bandwidth of 60%. Patterns are displayed using a 50-dB dynamic range with lateral direction along the horizontal axis and axial direction along the vertical axis. 24

2.3 The frequency response of a 2D PIO filter in k-space for a generic linear array with $d_e = 2\lambda$ using $\beta = 0.01$, 0.3 and 10. 25

2.4 The kernel of a 2D PIO filter in spatial domain for a 25 MHz linear array with $d_e = 2\lambda$ using $\beta = 0.3$. The axial direction is along the vertical axis and the lateral direction is along the horizontal axis, both in mm scale. 26

2.5 The GUI of the 2D PIO filtering algorithm. 28

3.1 Dual-mode ultrasound array geometry. The array elements are shown segmented in the elevation direction. This segmentation is for simulation purposes only. 35

3.2 Illustration of the pseudo-inverse compression filter frequency response designed for a Gaussian chirp transmit waveform. The effect of the regularization parameter, β, on the frequency response of the PIO is also shown. 39

3.3 Geometry of the wire target array phantom. The center wire was positioned at the geometric focus of the DMUA. 42

3.4 Grayscale images (50 dB) of the wire target array phantom using SA pulse-echo data. 45

3.5 Grayscale image (50 dB) of the wire target array shown in Figure 3.3 using (3.6) with simulated SA pulse-echo data. 47
3.6 Grayscale images (50 dB) of a simulated uniform scatterer phantom and the CIRS Model 55 3D quality assurance phantom using experimentally collected SA pulse-echo data. 49
3.7 Frequency response of designed pseudoinverse filter. 52
3.8 Grayscale images (50 dB) of the CIRS Model 55 quality assurance phantom using experimentally collected SA pulse-echo data. A chirp transmit pulse was used together with matched filter, (a), and a PIO filter, (b). . 53
4.1 Grayscale images (60 dB) of the PSFs, the vertical coordinate is axial direction, the horizontal coordinate is lateral direction and both are in mm. 61
4.2 Comparison of Axial and Lateral PSFs for 0.5λ pitch and 2λ pitch. . . . 62
4.3 Lateral PSFs, filtered by 2D PIO filter with regularization parameter $\beta =$ 0.001, 0.1 and 1. 63
4.4 Axial PSFs, filtered by 2D PIO filter with regularization parameter $\beta =$ 0.001, 0.1 and 1. 64
4.5 Spatial resolutions of results filtered by 2D PIO filter with sweeping regularization parameter β. 65
4.6 60 dB gray scale representation of the PSF filtered by 2D PIO filter with β=0.1. 66
4.7 Grayscale images (50 dB) obtained from the cyst phantom, the vertical coordinate is axial direction, the horizontal coordinate is lateral direction and both are in mm; (a) conventional beamforming using a Nyquist sampled array; (b) conventional beamforming using a coarsely sampled array (2λ). 69
4.8 Grayscale images (50 dB) obtained from the cyst phantom, filtered by the regularized 2D PIO filter, the vertical coordinate is axial direction, the horizontal coordinate is lateral direction and both are in mm. (a) β = 0.01, (b) $\beta = 0.1$, (c) β= 0.3, (d) $\beta = 1$, and (e) $\beta = 10$. 70

4.9 Lateral line plots through cyst center at z = 12 mm for different values of β. The loss of lateral resolution can be clearly seen for $\beta = 10$ while the loss of contrast is clear for $\beta = 0.01$. 71
4.10 Axial line plots through cyst center at x = 0 mm for different values of β. One can observe a minimal loss in resolution for $\beta = 10$ in the axial direction while the loss of contrast is clear for $\beta = 0.01$. 72
4.11 Contrast ratio vs. the regularization parameter β in logarithm scale (the dotted line with circle). MGR vs. the regularization parameter β in logarithm scale (the dashed line with cross). 74
4.12 Grayscale images (50 dB) obtained from the cyst phantom, the vertical coordinate is axial direction, the horizontal coordinate is lateral direction and both are in mm. (a) Conventional beamforming using a Nyquist sampled array; (b) conventional beamforming using a coarsely sampled array (2λ); (c) full k-space with $\beta = 0.3$; and (d) 2-D kernel with $\beta = 0.3$. 76
4.13 Grayscale images (50 dB) obtained from the cyst phantom, the vertical coordinate is axial direction, the horizontal coordinate is lateral direction and both are in mm. (a) Conventional beamforming using a Nyquist sampled array; (b) conventional beamforming using a coarsely sampled array (1.2λ); (c) conventional beamforming using a coarsely sampled array (2λ); (d) full k-space with $\beta = 0.3$. 79
4.14 Contrast ratio vs. the regularization parameter β in logarithm scale (the dotted line with circle). MGR vs. the regularization parameter β in logarithm scale (the dashed line with cross). 81
4.15 Spatial resolutions of results filtered by 2D PIO filter with sweeping regularization parameter β. 82
4.16 Grayscale images (50 dB) obtained from the cystic target and high contrast target at depth of 4 cm in CIRS Model 040 quality assurance phantom, the vertical coordinate is axial direction, the horizontal coordinate is lateral direction and both are in mm. 84

4.17 Grayscale images (50 dB) obtained from the cystic target and high contrast target at depth of 2 cm in CIRS Model 040 quality assurance phantom, the vertical coordinate is axial direction, the horizontal coordinate is lateral direction and both are in mm. 85
4.18 CR vs regularization parameter β in logarithm scale. 86
4.19 Grayscale images (60 dB) of the *in vitro* porcine eye, the vertical coordinate is axial direction, the horizontal coordinate is lateral direction and both are in mm. 88
4.20 The frequency response of the 2D PIO filter in k-space, applied to the carotid artery data with the regularization parameter β=1. 90
4.21 The grayscale image (50 dB) of the right carotid artery, the vertical coordinate is axial direction, the horizontal coordinate is lateral direction and both are in mm. 91
4.22 The grayscale image (50 dB) of the right carotid artery, filtered by the 2D PIO filter, the vertical coordinate is axial direction, the horizontal coordinate is lateral direction and both are in mm. 92
4.23 Contrast ratio of results filtered by 2D PIO filter with sweeping regularization parameter β. 93
A.1 Grayscale images (50 dB) of the PSF with 40%, 60% and 80% bandwidths, (a) - (c). A lateral profile of the 40% PSF is shown in (d) to demonstrate the sidelobe structure. 115
A.2 Axial & lateral resolutions and lateral sidelobe level vs. bandwidth for the 1 MHz DMUA. 116
A.3 Grayscale images (50 dB) of a simulated phantom with a cyst at [0 0 100] mm with radius = 6 mm; (a) 40% bandwidth; (b) 60% bandwidth; (c) 80% bandwidth. 118
A.4 Axial line plots (at x=0 mm) from the image data shown in Figure A.3(a) - (c). 119
A.5 Grayscale images (50 dB) of a simulated phantom with a cyst at [20 0 100] mm with radius = 6 mm; (a) 40% bandwidth; (b) 60% bandwidth; (c) 80% bandwidth. 120

A.6 Grayscale images (50 dB) of a simulated phantom with cysts at [0 0 70] mm, [0 0 100] mm, [0 0 130] mm and [0 0 160] mm with radius = 6 mm; (a) 40% bandwidth; (b) 60% bandwidth; (c) 80% bandwidth; 123
A.7 Grayscale image (50 dB) of the PSF of a 128-element, 40% bandwidth DMUA using the same aperture as the current DMUA. 124
A.8 Grayscale image (50 dB) and a lateral profile of the PSF of a 64-element DMUA with element height, $h = 25$ mm (elevation f-number = 4). . . . 128
A.9 Geometry of a modified DMUA: a 128×4-element array that can be configured as 64×1 array in therapy mode and 128×1 array in imaging mode. 130
A.10 Grayscale image (50 dB) of the point spread function for the modified DMUA design. 131
A.11 Grayscale image (50 dB) of the wire target array using the modified DMUA design. 132
B.1 The cross sectional grayscale (50 dB) image (a) and the axial displacement field (b) of the 4-mm flow channel in the ATS phantom, the vertical coordinate is axial direction, the horizontal coordinate is lateral direction, both of the axises and color bar are in mm; therefore the displacements are between -39.2 μm and 56.5 μm. 139
B.2 The axial strain and axial shear strain of the 4-mm flow channel cross sectional walls. 140
B.3 The axial and lateral displacement fields from the flow phantom results are color-coded and overlaid on the B-mode gray scale images. Distances and displacements are given in mm. 142
B.4 The axial strain and axial shear strain of the 4-mm flow channel longitudinal walls. 143
B.5 The lateral strain and lateral shear strain of the 4-mm flow channel longitudinal walls. 144
B.6 The periodic average flow velocity obtained from the tracked fluid displacements within the 4-mm flow channel in the ATS phantom and the corresponding periodic channel diameter computed from the tracked channel wall displacements. 145

B.7 The total displacement vector waveforms within the channel at different time instances. 146
B.8 The cross sectional grayscale (50 dB) image of the carotid artery, the vertical coordinate is axial direction, the horizontal coordinate is lateral direction, both are in mm. 148
B.9 The axial and lateral displacement fields of the carotid artery cross sectional view, the vertical coordinate is axial direction, the horizontal coordinate is lateral direction, both of the axises and color bar are in mm. 149
B.10 The axial strain and axial shear strain of the carotid artery cross sectional vessel walls. 150
B.11 The lateral strain and lateral shear strain of the carotid artery cross sectional vessel walls. 151
B.12 The lateral and axial displacements of the carotid artery are color-coded and overlaid on the B-mode gray scale images. 153
B.13 The lateral and axial strains and sheer strains of the carotid artery are color-coded and overlaid on the B-mode images. 154
B.14 The change of vessel diameter and average flow velocity obtained from local 2-dimensional displacement field. 155
B.15 The ECG signal from the same patient using the Sonix RP system. . . . 156

Chapter 1

Introduction

1.1 Ultrasound Imaging: A Historical Overview

Ultrasonic imaging has been well developed and widely applied in clinical applications for many years. While imaging tissue using ultrasound may be dated back to 1930s [2], 2D pulse echo ultrasound was first introduced in the 1950s with the seminal paper by Wild and Reid [3] based on the authors' research at the University of Minnesota. Almost simultaneously, they reported on a study of their system for detecting breast tumors [4, 5]. Today, B-mode ultrasound is used as a supporting role in the FDA-approved mammography [6].

It is clear that ultrasound imaging benefited greatly from advances in radar technology during World War II. For example, the concept of time gain compensation, also introduced by Wild and Reid [4], was based on a similar technique applied to radar signals. This represents an example of using a simple signal processing technique to compensate to a known deterioration of ultrasound echoes from deeper targets due to the attenuation phenomenon. Signal processing continued to play an increasingly more significant role in ultrasound imaging, limited primarily by realtime considerations. Recent advances in ASIC, FPGA, and GPU technologies and successful incorporation of these technologies on ultrasound scanners have spurred what appears to be a new revolution in this imaging technology. Sophisticated realtime signal processing is allowing for the implementation of new imaging modalities on ultrasound scanners, e.g. elastography [7], harmonic and pulse inversion imaging [8], thermography [9]. Of course,

Doppler ultrasound has benefited greatly from realtime signal processing since the early days of heterodyne receivers [10] and phase-quadrature demodulation [11] for extracting forward and reverse flow.

Ultrasound imaging has also been benefited greatly from advances in transducer technology that have led to the introduction of array transducers [12], beamforming and dynamic focusing [13], and digital beamforming [14]. Dynamic focusing can be thought of as a pre-beamforming aperture processing technique that compensates for the effects of focusing to extend the imaging field of view (FoV) of pulse-echo ultrasound. Digital beamforming and dynamic focusing allowed for significant improvement in image quality for B-mode ultrasound as can be easily seen from a review of the image galleries provided by various vendors for their latest scanners.

1.2 Current Status

Today's ultrasound scanners (medium to high end) routinely support additional imaging modes like contrast-enhanced ultrasonography (CEUS) [15], elastography [16], *etc.* These new modes are in addition to Doppler, which has been standard on ultrasound equipments for many years. CEUS utilizes microbubble ultrasound contrast agents (UCAs) [15] to improve imaging blood perfusion with the ultimate goal of imaging the microvasculature. Algorithms with various degrees of signal processing sophistication have been proposed [8, 17]. We are still working towards the ultimate goal of CEUS imaging, but the results obtained so far are quite exciting, especially in the area of imaging myocardial perfusion. Elastography is also thriving and is becoming increasingly available on existing scanners following the method proposed by Ophir *et al.* More recently, a specialized scanner, the Aixplorer, has been developed to implement the supersonic shear wave imaging developed by Fink *et al* [18].

Despite the tremendous progress and improvement in image quality for B-mode ultrasound, a fundamental limitation remains. Compared to other medical imaging modalities (e.g. X-ray CT, MRI, etc.), B-mode ultrasound offers relatively low soft-tissue contrast. This is primarily due to the *speckle* phenomenon, but other contributors are low SNR (deep targets), reverberations (cysts and blood vessels), and beamforming artifacts

in coarsely sampled apertures. The ultrasound imaging literature is replete with publications and patents on spatial and frequency compounding for contrast restoration [19]. These are typically applied to the grayscale (envelope-detected, log-compressed) image data and are of little interest to us. This thesis research is more concerned with contrast-restoration methods applicable to the RF data pre- or post-beamforming. The rationale behind this is that most interesting applications of ultrasound (e.g. elastography and thermography) require correlation processing in the RF domain. Therefore, the most useful contrast restoration algorithms are those leading to reduced clutter and other artifacts leaving the RF signal components, including speckle[1] , intact.

1.3 The Future of Ultrasound: New Opportunities and New Challenges

Progress in ultrasound imaging continues to occur at an impressive pace. Many leading researchers believe that we are at the cusp of another revolution in this imaging modality (and in ultrasound-enabled modalities like elastography). This is enabled by realtime signal processing (both algorithms and hardware platforms) and advanced transducer technology. There are several frontier areas within the field of medical ultrasound. For example:

1. Realtime 3D echocardiography (RT3D) is becoming available from major vendors (Philips, GE, and Siemens), thanks to the development of 2D matrix array transducers and miniature element-side electronics. Full heart scans with volume rates in the 15 - 20 volume per second (vps) are available. Nyquist sampling of the 2D apertures necessary for acceptable quality RT3D is not likely to occur in the foreseeable future. Therefore, 3D imaging with coarsely-sampled apertures will continue to be used for years to come, necessitating methods for reducing the well-known artifacts due to coarse sampling.

2. HFUS arrays operating in the range of 25 - 50 MHz. In this area, advances in transducer technology allow for the design and fabrication of linear arrays with center-to-center spacing in the range of 1 - 3 λ (wavelength), with 2λ being typical

[1] Thermography and elastography use speckle tracking for imaging tissue deformations.

[20–28]. Based on expert assessment of the current state-of-the-art transducer technology, this limitation is likely to remain a challenge in the foreseeable future. Therefore, reducing the beamforming artifacts is expected to play a major role in the successful use of HFUS arrays in medical applications.

3. Dual-mode ultrasound array (DMUA) structures for imaging and therapy [29]. The concept of DMUA has been introduced recently, thanks to advances in piezo-composite transducer technology. DMUAs have special characteristics, dictated by therapeutic design considerations, which results in degradation of their imaging performance. Specifically, DMUAs generally sample concave apertures (for improving therapeutic focusing gain) and utilize elements with dimensions larger than a wavelength (to preserve power transfer efficiency in therapeutic mode). The concave geometry creates highly non-uniform imaging field of view (IxFOV). In addition, reverberation effects are confounded by the use of the concave geometry. Therefore, special consideration of these characteristics of DMUAs are needed for acquiring good image quality.

1.4 Scope of the Thesis Research

We are interested in approaches for contrast restoration from clutter resulting from imaging wavefront propagation. A physical model for wave propagation is assumed and is used as a basis for any simplifying assumptions when appropriate, e.g. range-shift invariance for wavefronts near the focus or in the far fields of unfocused apertures. Attenuation, aberration, and reverberations can be accounted for if necessary, but homogeneous tissue model is assumed at this point.

A special emphasis is put on array imaging as array transducers become more dominant in both clinical ultrasound and pre-clinical HFUS. The benefits of arrays in ultrasonic imaging are well understood for their electronic scanning capability and amply demonstrated by their wide use in clinical scanners. The general scheme of a modern ultrasound array imaging system in terms of signal processing and filtering chain is illustrated in Figure 1.1. The imaging performance of this system is usually determined by a few key components, classified as transmit waveform design, aperture design &

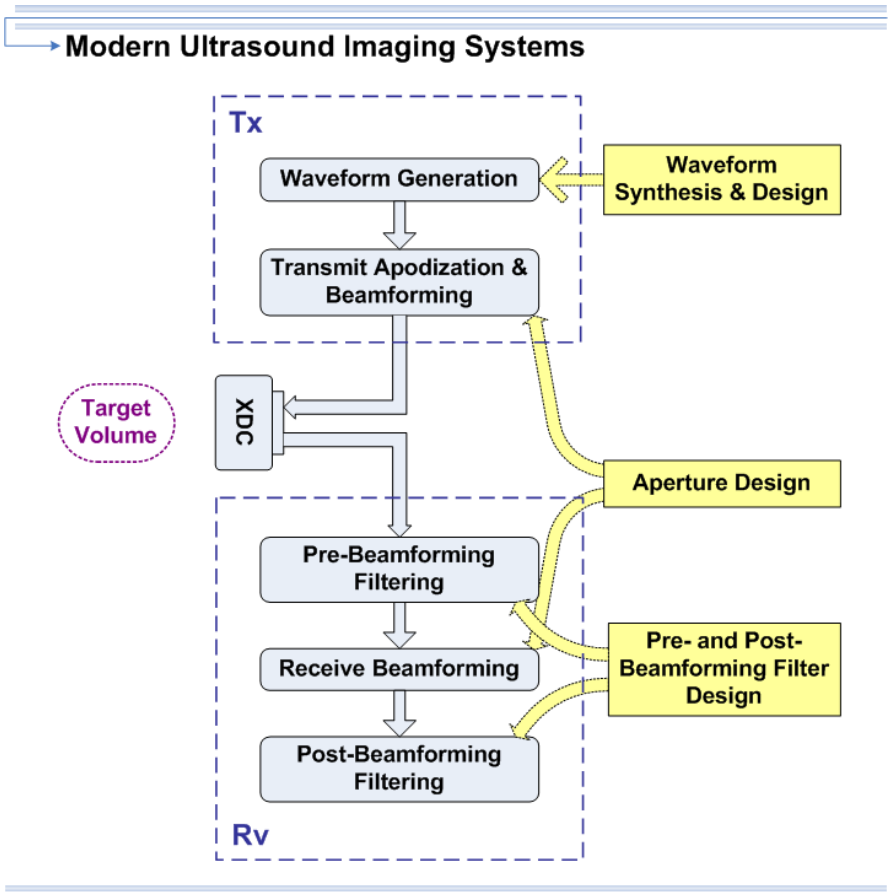

Figure 1.1: Ultrasound array imaging system.

beamforming, pre- or post-beamforming receive filter design and image processing. Following the signal flow, the Waveform Synthesis & Design block summarizes the design process of the transmitted waveforms, considering both optimization and the specifications of waveform generators. The transmitted waveforms are spatial-filtered for beam focusing, steering or sidelobe reduction by apodization and beamforming. Both Waveform Design block and Aperture Design block usually involve field simulations and rely on the knowledge of ultrasound imaging mechanism. The transmitted electrical signals are transformed to acoustic signals by the array transducer and propagated into the imaging field. The echoes generated by the target volume propagate back, received by the transducer. In the receive section, the received echoes are filtered before receive beamforming in certain cases, but it is less often than post-beamforming filtering in commercial scanners due to high complexity. Similar to transmit beamforming, receive beamformer acts as a spatial-matched filter for signals from different directions. The beamformed data are usually filtered by a post-beamforming filter, such as a simple band-pass filter for better imaging performance. After filtering, the received data is post-processed for better image quality with imaging processing techniques, such as decimation or interpolation, log compression, contrast & edge enhancement, speckle reduction *etc.*

1.5 Spatio-temporal Wavefronts and k-space Analysis

Based on the above description, we see that the fundamental analysis of the ultrasound array imaging system involves the 'understanding of the wave propagation with the designed transmit waveform, aperture and receive filtering operations. The ultrasound wave propagates in a 3D space plus a time axis. Because most of the array transducers have focusing lens in front of the elements focusing the beams in the elevation direction, ultrasound imaging presents a cross-section image of the tissue volume. This means that the 2D cross section results from a 3D slice determined by the beam width in the elevation direction. Therefore, we will use k-space, 2D spatial frequency domain, methods for characterizing and analyzing ultrasound array imaging systems. This approach is based on linear system theory [19], and it is very intuitive to use the spatial- or temporal-frequency domain representations of ultrasound system impulse responses

and scattering functions to understand and analyze imaging systems.

1.6 Contributions of this Thesis Research

The main contribution of this dissertation is deriving a 2D post-beamforming pseudoinverse filter from the array imaging model using spatial frequency domain analysis. (Pseudo)inverse and matched filtering has been successfully used in ultrasonic imaging to restore axial resolution, primarily in conjunction with coded excitation [30–34]. The algorithm in [30,35] employs a filter bank for parallel processing of echo data from multiple directions from a single beamforming operation. The coefficients of the filters were computed based on a regularized inverse of a discretized 2D (axial-lateral) pulse-echo propagation operator from the array to the region of interest (ROI). For a single A-line, the sampled beamformer output is related to the scatterer distribution within the ROI by a discretized propagation operator (matrix) as described in [30]. The propagation operator was represented as a block row matrix with each block representing the array response in a given lateral direction. Using the range-shift invariance assumption [30], the matrix elements of the propagation operator were represented as Toeplitz. This allowed for the use of the computationally-efficient discrete Fourier transform (DFT) in finding a pseudoinverse operator resulting in the filter bank implementation for the parallel imaging in multiple directions from a single beamforming operation. In principle, the filter bank could be designed to remove some of the beamforming artifacts, but this is limited to the removal of uncorrelated grating-lobe components from the desired beam direction(s). Therefore, the PIO is more effective in decoupling echoes from different directions in conjunction with multi-modal coded excitation, i.e. several distinct codes are transmitted simultaneously with single receive beamforming of echoes from the ROI. In the case of the DMUA, we have used this post-beamforming filtering, together with coded excitation to improve the uniformity of the IxFOV, improve the axial resolution and reduce reverberations for the DMUA systems currently being used at our laboratory [1].

In addition, the single-line model for the 1-dimensional pseudoinverse filter is extended to include data from multiple A-lines (up to a frame) by axial and lateral shifting of the 2D impulse response of the single-line beamforming operation. This

discretized propagation model results in a system matrix with attractive properties for computationally-efficient inversion. Not only does this approach improve the computational efficiency and reduce the storage cost of the implementation, but it also transforms a usually ill-posed inverse problem to a well-posed FFT problem. In addition, the original inversion operation in spatial-temporal domain is transformed into multiplication operation in 2-dimensional frequency domain, preceded and followed by FFT-order DFT operations. Furthermore, regularization is used to avoid the noise amplification due to the inversion of small eigenvalues of the operator (or Fourier coefficients in the frequency domain). As demonstrated by the simulation results, our regularization approach leads to well-behaved PSFs with properties that change gradually with increasing values of the regularization parameter, β. In particular, the axial and lateral dimensions of the PSF increase approximately as a sigmoid function with respect to $\log \beta$. Similarly, the mainlobe-to-gratinglobe (energy) ratio (MGR) increases approximately as a sigmoid function with respect to $\log \beta$.

1.7 Applications

This characteristic of the pseudoinverse filter enables a parameter-controlled and, more importantly, user-controlled imaging performance. In the case of the HFUS, we have used the 2D pseudoinverse filtering algorithm for restoring the contrast resolution of the imaging system by mitigating the degrading effects of the grating lobes resulting from conventional beamforming using coarsely-sampled apertures. The 2D post-beamforming pseudoinverse filter can also be applied to suppressing artifacts inside of blood vessels before quantitative imaging of vascular structure. It is obvious that eliminating the artifacts helps detecting the speckle formed from the moving blood cells, consequently leading to a better estimation of the flow especially in the vicinity of the vessel walls. These regions are essential for a good hymodynamics modeling or a good diagnosis for disease status. More other applications can be benefited by this pseudoinverse filtering technique with good understandings of the needs and bases of these applications. In those areas, the algorithms are developed with an eye on real-time implementation. Advances in VLSI technology have made it possible to implement increasingly sophisticated signal processing algorithms in real time at sampling rates suitable for the full

range of medical ultrasound applications. New technologies have also been adopted for these types of ultrasound signal/image processing algorithms such as using parallel computing *e.g.* CUDA programing for GPU or powerful FPGAs. Not only is this available for receive chain processing, but it is also available for arbitrary waveform generation and signal synthesis in the transmit chain. Given the variety of applications and array geometries in ultrasound imaging, it may be useful to envision a general framework for the transmit/receive chain of the imaging system. The block diagram shown in Figure 1.1 includes the major components of a modern ultrasound imaging system. Within this framework, one could design and implement signal processing algorithms along the transmit-receive chain that collectively serve to improve the image quality. An obvious example is coded excitation on transmit with inverse or matched filtering for signal compression on receive. The coded transmit waveforms themselves could be the result of signal synthesis algorithms (e.g. transmit-mode matched or inverse filtering).

1.8 Organization of the Thesis

The dissertation is organized into five chapters. Chapter 2 defines the linear array imaging system model which serves as a basis for all the derivations to our algorithm. The 1-dimensional pesudoinverse filter is also introduced in Chapter 2. Then Chapter 2 gives the mathematical derivations, explanation of underlying physics and the representations of the 2D pseudoinverse filter in both k-space and spatio-temporal forms. The design tradeoffs and implementation are also explained in this chapter. Chapter 3 describes applying the 1-dimensional pseudoinverse filter to improve the resolution of the image guidance of the dual-mode ultrasound array (DMUA) system. The DMUA system is used for minimally invasive treatment of cancer and other tissue abnormalities using high intensity focused ultrasound (HIFU) and monitoring the surgery using diagnostic-level pulse-echo ultrasound in one array. In Chapter 4, the 2D pseudoinverse filter is applied to restore lost contrast due to beamforming artifact caused by coarse sampling of array aperture. Finally Chapter 5 draws the conclusion and gives suggestions for future work.

Chapter 2

Post-Beamforming Pseudoinverse Filter

2.1 Introduction

Pseudoinverse and matched filterings have been successfully used in ultrasonic imaging to restore axial resolution, primarily in conjunction with coded excitation [30–34]. Coded excitation has been well accepted as a means of increasing signal energy for larger penetration depth under the FDA regulation on the signal peak energy. A receive filter is needed in this case for compressing the elongated pulses to recover system resolution. The proposed pseudoinverse filter bank in [30, 35] could be also used for removing uncorrelated grating-lobe components from the desired beam direction(s), decoupling echoes from different directions in conjunction with multi-modal coded excitation, i.e. several distinct codes are transmitted simultaneously with single receive beamforming of echoes from the ROI. This is useful for achieving fast frame rate ultrasound imaging, *e.g.* in 3D ultrasound imaging for Cardiology. This filter is operated on a single A-line, the sampled beamformer output and related to the scatter distribution within the ROI by a discretized propagation operator (matrix) as described in [30]. That's why we call it a one-dimensional pesudoinverse operator (PIO) filter.

In this dissertation, we propose a 2-dimensional post-beamforming filtering algorithm derived from a multiple-scan linear array imaging system model. The single-line model is extended to include data from multiple A-lines (up to a frame) by axial and

lateral shifting of the 2D impulse response of the single-line beamforming operation. In principle, the filter is derived from 2-dimensional system response with information in not only the temporal direction (or the axial direction) but also the lateral direction. Based on this understanding, we are expecting this 2-dimensional filter is capable of recovering scatterer distribution from various imaging artifacts which can not be filtered by 1D filters, such as the beamforming artifact due to coarse sampling in the lateral direction.

The 2D PIO filtering algorithm is derived from the matrix formation of a one-dimensional linear array imaging model [30]. Given the fact that the received spatio-temporal echo data is the convolution of the imaging object and the array of shifted spatio-temporal system impulse responses, the process of retrieving the original object information corresponds to the inversion of the array of shifted spatio-temporal system impulse responses or the linear array propagation matrix. Note that the propagation matrix already takes into account the transducer excitation and the aperture apodization if there is any. However, this direct inversion method requires the inversion of a matrix with huge dimensions, consequently, unfeasible due to the impractical computational cost and lost of precision. A simple and efficient inversion method is derived and explained in the following subsections.

2.2 System Model

We begin by defining a uniform grid in the imaging field as shown in Figure 2.1 and assuming scatterers with random amplitude distribution at the grid points. The number of grid points within a range interval $[z_{min}, z_{max}]$ in the axial direction, N, determines the axial sampling rate. Similarly, the number of grid points in the lateral direction (or the number of scan lines) within $[x_{min}, x_{max}]$, M, determines the lateral sampling rate. We assume the grid spacing is small with respect to the correlation cell size of the imaging system in both directions. Note that the grid shown in Figure 2.1 represents a subregion of the imaging volume for purposes of reconstructions. Scattering from outside this region must be accounted for by the simulation model for the received echo data.

Define $s_{m,q}$ as the scatterer strength at grid location (m, q) ($m \in [1, M]$, $q \in [1, N]$),

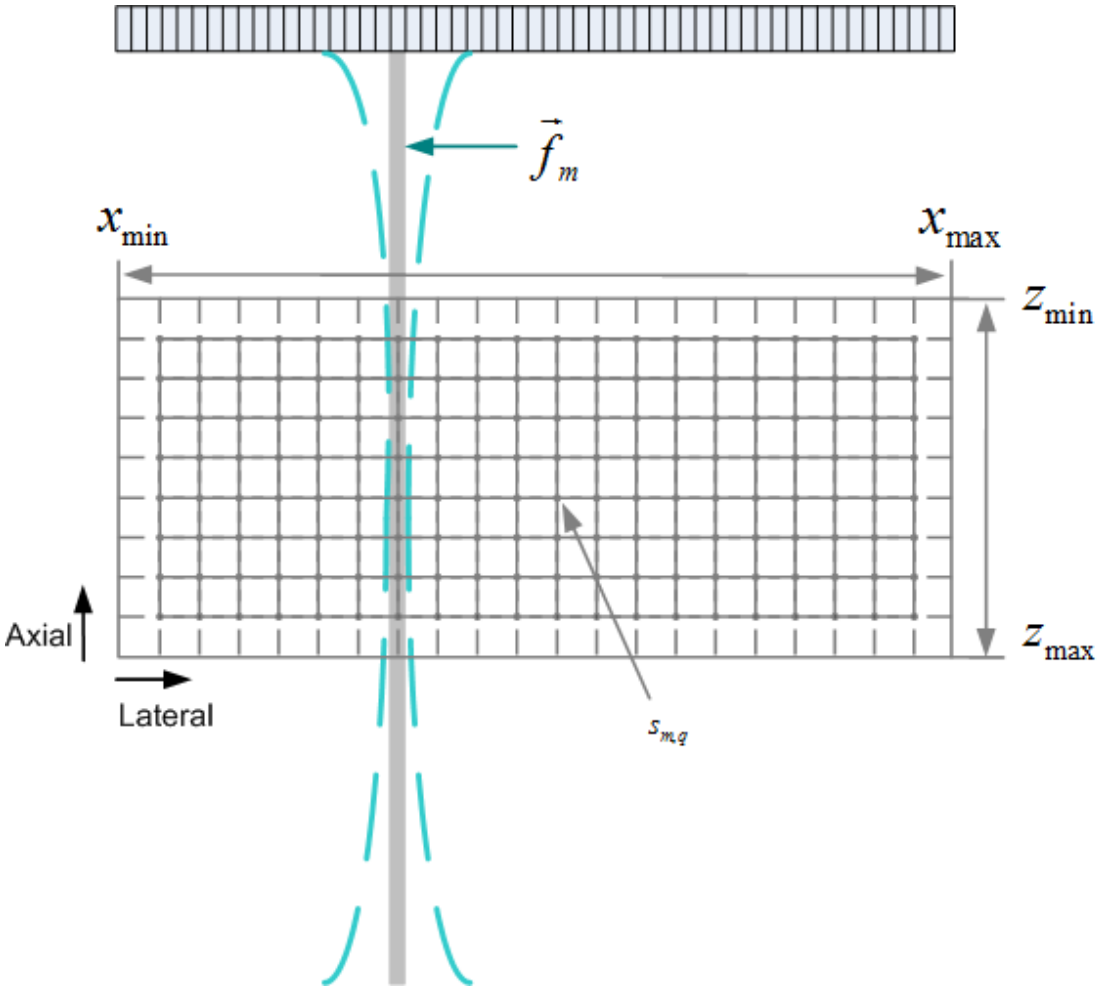

Figure 2.1: A 1D linear array system model where the scattering is assumed to result from scatters with random amplitudes on the Cartesian grid.

$\boldsymbol{\varsigma}_m$ as a vector of size $N_i \times 1$ containing amplitudes of scatterers along scan line m ($N_i >> N$). Let $\boldsymbol{S}$ be a vector containing all lines of scatterers in the imaging field ($M_i >> M$) as

$$\boldsymbol{S} = \begin{bmatrix} \cdots & \boldsymbol{\varsigma}_1^T & \boldsymbol{\varsigma}_2^T & \cdots & \boldsymbol{\varsigma}_M^T & \cdots \end{bmatrix}^T, \tag{2.1}$$

where, ^{T} denotes matrix/vector transpose. The discretized version of the received echo for scan line m in the range interval $[z_{min}, z_{max}]$ can be represented in vector form as $\boldsymbol{f}_m$ of size $N \times 1$ and all the M scan lines can be grouped in $\boldsymbol{F}$ as follows:

$$\boldsymbol{F} = \begin{bmatrix} \boldsymbol{f}_1^T & \boldsymbol{f}_2^T & \cdots & \boldsymbol{f}_M^T \end{bmatrix}^T. \tag{2.2}$$

The impulse response of the system at a grid point is the echo from a single unit-strength scatterer positioned at that point. For illustration purposes, we assume the point scatterer is at the center of the specified grid. Then the generated pulse-echo impulse response at grid point q along line i is denoted as vector $\boldsymbol{g}_{i,q}$ of size $N \times 1$ which contains the discretized samples in time-domain. The pulse-echo impulse responses at the grid points along line i can be grouped as

$$\boldsymbol{G}_i = \begin{bmatrix} \cdots & \boldsymbol{g}_{i,1} & \boldsymbol{g}_{i,2} & \cdots & \boldsymbol{g}_{i,N} & \cdots \end{bmatrix}. \tag{2.3}$$

Assume $\boldsymbol{G}_0$ is the matrix containing the pulse-echo impulse responses from grid points along the line through the focus and $\{\boldsymbol{G}_{\pm i}\}_{i=1}^{\infty}$ are the matrices containing pulse-echo impulse responses from the grid points along the lines on right/left sides of focus. Typically, $\boldsymbol{G}_i = \boldsymbol{G}_{-i}$ due to the symmetry of the linear array aperture or apodization. Based on the above notations and definitions, the received echo signal from one scan line is obtained by superposition,which can be represented in matrix form:

$$\boldsymbol{f}_m = \underbrace{\begin{bmatrix} \cdots & \boldsymbol{G}_{-i} & \cdots & \boldsymbol{G}_{-1} & \boldsymbol{G}_0 & \boldsymbol{G}_1 & \cdots & \boldsymbol{G}_i & \cdots \end{bmatrix}}_{\boldsymbol{\Psi}} \boldsymbol{S}, \tag{2.4}$$

where, $\boldsymbol{\Psi}$ is the spatio-temporal impulse response of the system and each G_i represents the response in a given lateral direction. Therefore, for a single A-line, the sampled beamformer output $\boldsymbol{f}_m$ is related to the scatter distribution $\boldsymbol{S}$ by a discretized propagation operator (matrix) $\boldsymbol{\Psi}$.

2.3 1D PIO Filter

The one-dimensional pseudoinverse filter proposed in [35] is derived from a system model for a single A-line acquisition using a 1D linear array. We will give a brief explanation of the filter design process, but defined on a Cartesian grid for the convenience of deriving the proposed two-dimensional pseudoinverse filter in the next section.

If AWGN noise is considered in the system, the system equation for a single A-line is

$$\boldsymbol{f}_m = \boldsymbol{\Psi}\boldsymbol{S} + \boldsymbol{n}, \tag{2.5}$$

where, $\boldsymbol{n}$ contains the AWGN noise term. Thus a minimum-norm least-square estimate of the scatter distribution $\boldsymbol{S}$ can be obtained as

$$\hat{\boldsymbol{s}} = \underbrace{\boldsymbol{\Psi}^H(\boldsymbol{\Psi}\boldsymbol{\Psi}^H)^\dagger}_{\boldsymbol{PIO}_{1D}}\boldsymbol{S}, \tag{2.6}$$

where, the superscripts ^{H}, † represent matrix Hermitian, and generalized inverse operators, respectively and the $\boldsymbol{PIO}_{1D}$ is defined as the one-dimensional pseudoinverse operator.

A further reduction of computational complexity can be achieved by using the range-shift invariance (RSI) assumption [30, 35]. Strictly speaking, the energy and the shape of the impulse responses in the matrices $\boldsymbol{G}_i$ are gradually changing along the axial direction. However, this change is moderate in the vicinity of the focus where we can establish computationally that the impulse responses can be approximated by the time-shifted versions of each other. With this assumption, the matrix $\boldsymbol{G}_i$ can be represented as Toeplitz. In addition, the array beam pattern justifies truncation of the impulse responses from grid points far away from the focus. This implies: $\boldsymbol{g}_{i,q} \to 0$, $q > N_f$,N_f is some finite value. Using the shifted version of $\boldsymbol{g}_{i,c}$, the pulse-echo impulse response at the focus, the RSI approximation version of $\boldsymbol{G}_i$ is a banded Toeplitz matrix of size $N \times N$:

$$\boldsymbol{G}_i = \mathcal{T}(0, \cdots, g_{i,c}(0), g_{i,c}(1), \cdots, g_{i,c}(N_f), \cdots, 0), \tag{2.7}$$

where N_f is the number of nonzero samples of the impulse response along the ith direction and $\mathcal{T}$ stands for the operator of forming a Toeplitz matrix using a specified

sequence. The Toeplitz structure allows diagonalization using DFT matrices:

$$\boldsymbol{G}_i = \boldsymbol{F}_N \boldsymbol{H}_i \boldsymbol{F}_N^{-1}, \tag{2.8}$$

where, $\boldsymbol{H}_i$ is a diagonal matrix and $\boldsymbol{F}_N$ is a DFT matrix of size N:

$$\boldsymbol{F}_N = \begin{pmatrix} 1 & 1 & \cdots & 1 \\ 1 & W_N^{1\cdot 1} & \cdots & W_N^{1\cdot(N-1)} \\ \vdots & & \ddots & \vdots \\ 1 & W_N^{(N-1)\cdot 1} & \cdots & W_N^{(N-1)\cdot(N-1)} \end{pmatrix}, \tag{2.9}$$

where $W_N = e^{-j\frac{2\pi}{N}}$. With this diagonalization, the $\boldsymbol{PIO}_{1D}$ becomes

$$\boldsymbol{PIO}_{1D} = \begin{pmatrix} \boldsymbol{PIOF}_1 & \boldsymbol{PIOF}_2 & \cdots & \boldsymbol{PIOF}_N \end{pmatrix}^T, \tag{2.10}$$

where, $\boldsymbol{PIOF}_i = \boldsymbol{F}_N \boldsymbol{Z}_i \boldsymbol{F}_N^{-1}$ is the i^{th} filter for obtaining the scatterer distribution along i^{th} lateral direction from received echo $\boldsymbol{f}_m$ and $\boldsymbol{Z}_i$ is a diagonal matrix with diagonal terms defined by

$$\{\boldsymbol{Z}_i\}_{k,k} = \frac{\boldsymbol{H}_{i\{k,k\}}}{\sum_{i=1}^{N} \left|\boldsymbol{H}_{i\{k,k\}}\right|^2}. \tag{2.11}$$

The above expression defines the $\boldsymbol{PIO}_{1D}$ filter bank in frequency domain. Thus, the estimate of the scatterer distribution is obtained by N filters:

$$\hat{\boldsymbol{s}} = \begin{pmatrix} \boldsymbol{PIOF}_1\boldsymbol{f}_m & \boldsymbol{PIOF}_2\boldsymbol{f}_m & \cdots & \boldsymbol{PIOF}_N\boldsymbol{f}_m \end{pmatrix}^T. \tag{2.12}$$

The RSI assumption followed by DFT operations allows complexity reduction from $N \times N$ filters to N filters and leads to the derivation of an illustrating expression of the $\boldsymbol{PIO}_{1D}$ filter as shown in Equation 2.11.

This filter bank implementation allows parallel processing of echo data from multiple directions in a single beamforming operation. In principle, the filter bank could be designed to decouple echoes from different directions given the echoes from different directions are uncorrelated. Therefore, more efficiency in decoupling requires the operation in conjunction with multi-modal coded excitation, i.e. several distinct codes are transmitted simultaneously with single receive beamforming of echoes from the ROI [30].

2.4 Structure Properties

The derivation of the two-dimensional pseudoinverse filter starts from the system model obtained in Section 2.2. The spatio-temporal impulse response equation for a single A-line is defined in Equation 2.4. We can group the received signals from M scan lines as follows

$$\boldsymbol{F} = \underbrace{\begin{pmatrix} \ddots & & & & \\ & \boldsymbol{\Psi} & & & \\ & & \boldsymbol{\Psi} & & \\ & & & \boldsymbol{\Psi} & \\ & & & & \ddots \end{pmatrix}}_{\bar{\boldsymbol{G}}_T} \boldsymbol{S}. \tag{2.13}$$

Equation 2.13 provides a basis for an inverse solution to determine the scatterer strength $\boldsymbol{S}$ from the measurement $\boldsymbol{F}$. However, this is not computationally feasible due to the extremely large sizes of the vectors involved. Furthermore, due to the finite aperture and finite bandwidth of the system, it will not be possible to recover the scatter strength exactly. Therefore, we would like to develop an algorithm for solving Equation 2.13 using a *regularized inverse* obtained through computationally efficient operations. The following properties of the operator $\bar{\boldsymbol{G}}_T$ provide a basis for such an algorithm:

A. The matrix $\bar{\boldsymbol{G}}_T$ is block Toeplitz.

B. The RSI approximation implies that the matrices $\boldsymbol{G}_i$ themselves being Toeplitz [30].

C. The array beam pattern in the axial and lateral directions justify truncation of the impulse responses from grid points far away from the focus. This implies $\bar{\boldsymbol{G}}_T$: $\boldsymbol{G}_i \to 0$, $|i| > M_f$; $\boldsymbol{g}_{i,q} \to 0$, $q > N_f$, where M_f and N_f are some finite values.

As pointed in Equation 2.7, $\boldsymbol{G}_i$ is a banded Toeplitz matrix of size $N \times N$. Therefore, $\bar{\boldsymbol{G}}_T$ is a block banded Toeplitz matrix with banded blocks, i.e. $\bar{\boldsymbol{G}}_T$ can be described as a Toeplitz-block block Toeplitz matrix. With the knowledge of the spatio-temporal impulse response $\boldsymbol{\Psi}$ and the output $\boldsymbol{F}$, retrieving the input $\boldsymbol{S}$ is an inverse problem. In principle, this solution can be obtained using matrix inversion assuming M_f and N_f are sufficiently large to minimize the truncation errors. However, inverting the

matrix $\bar{\boldsymbol{G}}_T$ is still a challenging computational problem due to its large dimensions ($MN \times MN$). While some savings in the storage requirements and number of operations can be realized by exploiting the Toeplitz structure of the matrix, the requirements remain prohibitively large, even on powerful computers utilized in modern scanners. To illustrate this point, we describe the storage and computational requirements for a well-known inversion algorithm. Specifically, Akaike [36] derived an efficient inversion algorithm for general block Toeplitz matrices. His algorithm is a generalization of the Toeplitz matrix inversion algorithm developed by Trench [37] and refined by Zohar [38]. The order of magnitude of the number of operations is $\mathcal{O}(N^3M^2)$ for Akaike's algorithm. The storage requirement for the block Toeplitz matrix $\bar{\boldsymbol{G}}_T$ is reduced to $\mathcal{O}(N^2M)$ compared to the original general matrix. However, the memory needed in this case exceeds 100 GB for typical values of M and N in high frequency ultrasound. Therefore, direct inversion of block Toeplitz matrices is not feasible for the ultrasonic imaging problems of interest.

2.5 Circulant-Block Block Circulant Matrix Approximation

2.5.1 Asymptotically Equivalent Circulant Matrices

The computational challenges of inverting the matrix $\bar{\boldsymbol{G}}_T$ described above can be circumvented by using the fact that a banded Toeplitz matrix is asymptotically equivalent to its associated circulant matrix given both matrices are bounded in the strong norm [39]. Asymptotic equivalence of the two matrices means they approximate each other as the matrix dimension becomes large. For a banded Toeplitz matrix, its associated circulant matrix can be simply formed by filling in the upper right and lower left corners with the appropriate entries, e.g. for $\boldsymbol{G}_i$, the asymptotically equivalent circulant matrix is:

$$\boldsymbol{C}_i = \mathcal{C}(0, \cdots, g_{i,c}(0), g_{i,c}(1), \cdots, g_{i,c}(N_f), \cdots, 0), \tag{2.14}$$

where, $\mathcal{C}$ stands for the operator of forming a circulant matrix using a specified sequence. With $\boldsymbol{C}_i$ as the associated circulant matrix for $\boldsymbol{G}_i$, the eigenvalues of $\boldsymbol{G}_i$ and the eigenvalues of $\boldsymbol{C}_i$ are asymptotically equally distributed [39]. In addition, as long

as the strong norm of the inverse of $\boldsymbol{G}_i$ and the strong norm of the inverse of $\boldsymbol{C}_i$ are bounded, the inverse of $\boldsymbol{C}_i$ is asymptotically equivalent to the inverse of $\boldsymbol{G}_i$ [39].

Note that an $N \times N$ circulant matrix can be diagonalized using a size-N DFT matrix and the diagonal values are the DFT coefficients, which are samples of the discrete-time Fourier transform (DTFT) of the underlying sequence. Therefore, the asymptotic equivalence between Toeplitz matrices and circulant matrices can be understood in terms of the equivalence between linear and circular convolutions with zero-padding applied appropriately to avoid time-domain aliasing.

2.5.2 Asymptotically equivalent CBBC Matrices

Similar to the Toeplitz matrices, the Toeplitz-Block Block Toeplitz (TBBT) matrices can be approximated by their associated Circulant-Block Block Circulant (CBBC) matrices [40,41]. This approximation has the obvious advantages of improving the computational efficiency and reducing the storage cost of inverting the TBBT matrix. In addition, it transforms a usually ill-posed inverse problem to a well-posed FFT problem. Bose [40] extended the **Szegö** theorem for the TBBT matrices. Specifically, the sequence of eigenvalues of Hermitian block Toeplitz with Toeplitz-block matrices are asymptotically equally distributed as the sequence of eigenvalues of their associated CBBC matrices. Using similar arguments to those given in Section 2.5.1, the asymptotic equivalence between TBBT matrices and CBBC matrices can be understood in light of the relationship between the two-dimensional circular convolution and 2D linear convolution.

The 2D convolution TBBT matrix, $\bar{\boldsymbol{G}}_T$, can be replaced by its associated CBBC matrix with $M \times M$ blocks and the truncated version of the original convolution equation Equation 2.13 can be expressed as:

$$\boldsymbol{F} = \underbrace{\mathcal{C}(0, \cdots, \boldsymbol{C}_{-M_f}, \cdots, \boldsymbol{C}_{-1}, \boldsymbol{C}_0, \boldsymbol{C}_1, \cdots, \boldsymbol{C}_{M_f}, \cdots, 0)}_{\bar{\boldsymbol{G}}_C} \boldsymbol{S}_M, \tag{2.15}$$

where, each element in $\bar{\boldsymbol{G}}_C$ is a circulant matrix, and $\boldsymbol{S}_M$ of size $M \times 1$ is defined as the truncated version of $\boldsymbol{S}$:

$$\boldsymbol{S} = \begin{bmatrix} \boldsymbol{s}_1^T & \boldsymbol{s}_2^T & \cdots & \boldsymbol{s}_M^T \end{bmatrix}^T. \tag{2.16}$$

2.6 Inversion of the CBBC Matrix and Derivation

Equation 2.15 is the CBBC matrix equivalent of the convolutional system model to be inverted. It provides the basis for the regularized inversion algorithm described by the following steps [42]:

2.6.1 Diagonalize the Circulant Blocks

The circulant blocks $\boldsymbol{C}_i$'s in $\bar{\boldsymbol{G}}_C$ can be diagonalized using the direct sum of DFT matrices. The direct sum of the DFT matrices is defined as

$$\boldsymbol{Q} = \oplus_{m=1}^{M} \boldsymbol{F}_N = \begin{pmatrix} \boldsymbol{F}_N & & & \\ & \boldsymbol{F}_N & & \\ & & \ddots & \\ & & & \boldsymbol{F}_N \end{pmatrix}. \tag{2.17}$$

The circulant blocks $\boldsymbol{G}_i$'s can be diagonalized by multiplying $\boldsymbol{Q}$ and $\boldsymbol{Q}^{-1}$ from left and right sides of $\bar{\boldsymbol{G}}_C$:

$$\bar{\boldsymbol{H}} = \boldsymbol{Q}\bar{\boldsymbol{G}}_C\boldsymbol{Q}^{-1}, \tag{2.18}$$

where $\bar{\boldsymbol{H}}$ retains the block circulant structure as $\bar{\boldsymbol{G}}_C$, but every block $\boldsymbol{H}_i$ is a diagonal matrix obtained by

$$\boldsymbol{H}_i = \boldsymbol{F}_N\boldsymbol{C}_i\boldsymbol{F}_N^{-1}. \tag{2.19}$$

That is,

$$\bar{\boldsymbol{H}} = \mathcal{C}(\boldsymbol{0}, \cdots, \boldsymbol{H}_{-M_f}, \cdots, \boldsymbol{H}_{-1}, \boldsymbol{H}_0, \boldsymbol{H}_1, \cdots, \boldsymbol{H}_{M_f}, \cdots, \boldsymbol{0}), \tag{2.20}$$

and

$$\begin{aligned} \boldsymbol{H}_i &= \begin{pmatrix} h_{i,0} & & & \\ & h_{i,1} & & \\ & & \ddots & \\ & & & h_{i,N-1} \end{pmatrix} \\ &= diag(h_{i,0}, h_{i,1}, \cdots, h_{i,N-1}), \end{aligned} \tag{2.21}$$

where $diag(\cdot)$ is defined as the operator of forming a diagonal matrix using the specified input series and $\{h_{i,n}\}_{n=0}^{N-1}$ is the DFT coefficients from the Fourier-Transform of

$\{g_{i,c}(l)\}_{l=0}^{N-1}$ forming the circulant matrix $\boldsymbol{G}_i$:

$$h_{i,n} = \sum_{l=0}^{N-1} g_{i,c}(l) W_N^{nl}. \tag{2.22}$$

2.6.2 Block-Diagonalize the Block Circulant Matrix

The circulant block matrix $\bar{\boldsymbol{H}}$ can be diagonalized using the direct product of a DFT matrix and an identity matrix:

$$\begin{aligned} \boldsymbol{P} &= \boldsymbol{F}_M \otimes \boldsymbol{I}_N \\ &= \begin{pmatrix} \boldsymbol{I}_N & \boldsymbol{I}_N & \cdots & \boldsymbol{I}_N \\ \boldsymbol{I}_N & W_M^{1\cdot 1}\boldsymbol{I}_N & \cdots & W_M^{1\cdot(M-1)}\boldsymbol{I}_N \\ \vdots & & \ddots & \vdots \\ \boldsymbol{I}_N & W_M^{(M-1)\cdot 1}\boldsymbol{I}_N & \cdots & W_M^{(M-1)\cdot(M-1)}\boldsymbol{I}_N \end{pmatrix}, \end{aligned} \tag{2.23}$$

where $\boldsymbol{F}_M$ is a DFT matrix of size M and $\boldsymbol{I}_N$ is an identity matrix of size N. The block diagonal matrix $\bar{\boldsymbol{D}}$ can be obtained by

$$\bar{\boldsymbol{D}} = \boldsymbol{P}\bar{\boldsymbol{H}}\boldsymbol{P}^{-1}, \tag{2.24}$$

which is simply a diagonal matrix:

$$\bar{\boldsymbol{D}} = diag(\boldsymbol{D}_0, \boldsymbol{D}_1, \cdots, \boldsymbol{D}_{M-1}), \tag{2.25}$$

and

$$\boldsymbol{D}_k = \sum_{i=0}^{M-1} W_M^{ik} \boldsymbol{H}_i. \tag{2.26}$$

Note that $\boldsymbol{H}_i$ is already a diagonal matrix, so $\boldsymbol{D}_k$ is a diagonal matrix as well,

$$\boldsymbol{D}_k = diag(d_{k,0}, d_{k,1}, \cdots, d_{k,N-1}), \tag{2.27}$$

where,

$$d_{k,n} = \sum_{i=0}^{M-1} h_{i,n} W_M^{ik}. \tag{2.28}$$

Substituting Equation 2.22 into Equation 2.28, we have

$$d_{k,n} = \sum_{i=0}^{M-1} \sum_{l=0}^{N-1} g_{i,c}(l) W_N^{nl} W_M^{ik}. \tag{2.29}$$

Equation 2.29 shows that the diagonal terms are the 2D DFT of the sequence $g_{i,c}(l)$ or the k-space representation of our system model. In this formulation, diagonalizing the block matrices $\boldsymbol{G}_k$ is a Fourier transform in the axial direction (time) and block-diagonalizing $\bar{\boldsymbol{G}}_C$ is a Fourier transform in lateral direction. Equation 2.29 can be written in matrix form,

$$\bar{\boldsymbol{D}} = \boldsymbol{P}\boldsymbol{Q}\bar{\boldsymbol{G}}_C\boldsymbol{Q}^{-1}\boldsymbol{P}^{-1}. \tag{2.30}$$

Alternatively, the matrix $\bar{\boldsymbol{G}}_C$ can be written in terms of the diagonal matrix $\bar{\boldsymbol{D}}$ and DFT (and inverse DFT) operations

$$\bar{\boldsymbol{G}}_C = \boldsymbol{Q}^{-1}\boldsymbol{P}^{-1}\bar{\boldsymbol{D}}\boldsymbol{P}\boldsymbol{Q}. \tag{2.31}$$

2.6.3 k-Space Inverse Filtering

Substituting Equation 2.31 in Equation 2.15, we obtain

$$\boldsymbol{F} = \boldsymbol{Q}^{-1}\boldsymbol{P}^{-1}\bar{\boldsymbol{D}}\boldsymbol{P}\boldsymbol{Q}\boldsymbol{S}_M, \tag{2.32}$$

which, upon multiplying by $\boldsymbol{P}\boldsymbol{Q}$ from the left, yields the k-space representation of Equation 2.15,

$$\underbrace{\boldsymbol{P}\boldsymbol{Q}\boldsymbol{F}}_{\boldsymbol{F}_K} = \bar{\boldsymbol{D}}\,\underbrace{\boldsymbol{P}\boldsymbol{Q}\boldsymbol{S}_M}_{\boldsymbol{S}_K}. \tag{2.33}$$

The vectors $\boldsymbol{F}_K$ and $\boldsymbol{S}_K$ are simply the 2D DFTs of $\boldsymbol{F}$ and $\boldsymbol{S}_M$, respectively. From Equation 2.33, the inversion of Equation 2.15 in k-space is simplified as the inversion of the diagonal matrix $\bar{\boldsymbol{D}}$:

$$\hat{\boldsymbol{S}}_K = \bar{\boldsymbol{D}}^{\dagger}\boldsymbol{F}_K. \tag{2.34}$$

where, $\hat{\boldsymbol{S}}_K$ is the estimate of $\boldsymbol{S}_K$ and the $(\cdot)^{\dagger}$ indicates the *regularized* inverse or *pseudoinverse*. The design of this 2D pseudoinverse operator (2D PIO) is discussed in Section 2.7 below.

2.6.4 Inverse 2D FFT

Finally, we obtain $\hat{\boldsymbol{S}}_M$ using an inverse 2D DFT:

$$\hat{\boldsymbol{S}}_M = \boldsymbol{P}^{-1}\boldsymbol{Q}^{-1}\hat{\boldsymbol{S}}_K. \tag{2.35}$$

2.7 2D PIO Design

In principle, the inverse filtering problem can be achieved by inverting the diagonal matrix $\bar{\boldsymbol{D}}$ in Equation 2.33. However, this will result in very high gains at frequencies where the magnitude response of the system is very low. In practice, the inverse filter amplifies noise components rendering the restoration problem useless. Therefore, a regularized inverse solution is usually sought; one that attempts to incorporate the signal-to-noise (SNR) in the inversion problem. A simple solution is given by

$$d_{k,n}^{\dagger} = \frac{d_{k,n}^{*}}{|d_{k,n}|^2 + \beta}, \tag{2.36}$$

where β is a regularization parameter and $(\cdot)^*$ denotes complex conjugation. One can see that, for $\beta << |d_{k,n}|^2$, $d_{k,n}^{\dagger} \approx d_{k,n}^{-1}$; inverse filtering. On the other extreme, when $\beta >> |d_{k,n}|^2$, $d_{k,n}^{\dagger} \propto d_{k,n}^{*}$; matched filtering. The value of β could be determined based on SNR considerations. Other considerations include controlling the behavior of the resulting filter in the space domain, e.g. to minimize ringing. One can also consider frequency-dependent regularization (i.e. $\beta = \beta_{k,n}$), but this is usually coupled with specific knowledge of frequency dependence of the SNR.

In this project, the simple regularization scheme suggested by Equation 2.36 was found to be adequate for our purposes. This is justified based on the observation of the degradation pattern in k-space for different levels of spatial sampling as can be seen in Figure 2.2. The figure shows the 2D frequency response of a generic linear array pattern (no steering) using the same aperture and temporal bandwidth, but with element-to-element spacing, d_e, between 0.5λ and 4λ as shown. One can see that the bandwidth in the axial (temporal) direction is largely unaffected by the lateral sampling up to $d_e = 3\lambda$. For this range of element-to-element spacing, one can also see that the effect of increasing d_e introduces aliased lateral frequency components. Larger values of d_e produce significant ripple in the lateral frequency response in the passband of the system, which reduce both the lateral and the axial bandwidth of the imaging system. Our interest, however, is in the restoration of the imaging contrast for imaging systems employing arrays with d_e in the range of $1 - 3\lambda$. In this range, the coarser sampling effects are most pronounced in the lateral frequency direction. One would expect that the single-parameter regularization approach described by Equation 2.36 to affect the

array response mainly in the lateral frequency direction. This can be seen in Figure 2.3, which shows the frequency response of the regularized system for $d_e = 2\lambda$ and $\beta = 0.01$, 0.1, 1, and 10. One can see that the smallest value of β produces relatively high gains at frequencies outside the main passband of the system. This is likely to amplify noise components in the received signal, which can result in poor performance. One can also see that the highest value of β produces a 2D PIO that behaves like a matched filter. The matched filter is known to maximize the SNR (resulting in improved contrast), but possibly at the expense of reduced spatial resolution. The intermediate values of β are more likely to achieve a more appropriate tradeoff between spatial and contrast resolutions.

2.8 The 2D PIO Filter in Spatial-Temporal Form

As seen in the previous steps, the two FFT-order DFT operations dominate the computational cost since the filtering step is simply multiplications in k-space. If the 2D PIO filter is implemented in the spatial domain provided the filter has finite region of support, we expect the computational efficiency of the 2D filter can be further improved by eliminating the DFT operations, allowing real-time implementation especially with modern hardware platforms optimized for digital filtering. Therefore, we would like reformulate the filter in spatial-temporal domain, which is simply the 2-dimensional inverse DFT of the filter coefficients in k-space $d^{\dagger}_{k,n}$:

$$h_{m,l} = \frac{1}{NM} \sum_{k=0}^{M-1} \sum_{n=0}^{N-1} W_M^{-mk} W_N^{-nl} d^{\dagger}_{k,n}. \tag{2.37}$$

The impulse response main lobe of the filter in spatial domain is plotted in Figure 2.4 with a dynamic range of 60 dB. It is obvious that the majority of the information is within the 0.4 mm $\times$ 1.2 mm box which defines the finite region of support (ROS) of this filter. Therefore, a small kernel can be extracted for this filter for reducing the computational complexity at the same time expecting more or less same performance. Note that the filter also has two side lobes with maximum level of -44 dB which are not shown in Figure 2.4.

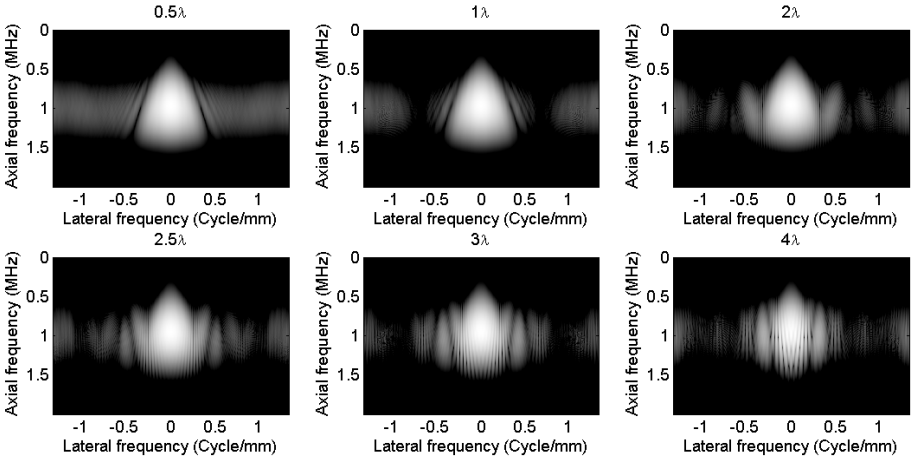

Figure 2.2: Frequency responses in k-space for generic apertures with different values of d_e: 0.5λ-4λ, f-number = 2 and fractional bandwidth of 60%. Patterns are displayed using a 50-dB dynamic range with lateral direction along the horizontal axis and axial direction along the vertical axis.

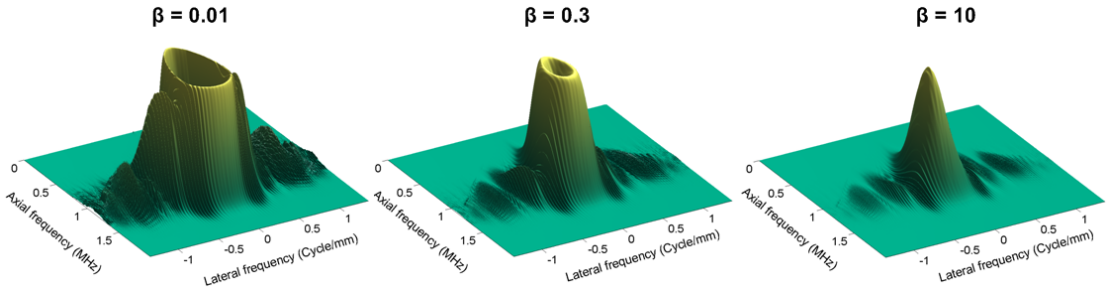

Figure 2.3: The frequency response of a 2D PIO filter in k-space for a generic linear array with $d_e = 2\lambda$ using $\beta = 0.01$, 0.3 and 10.

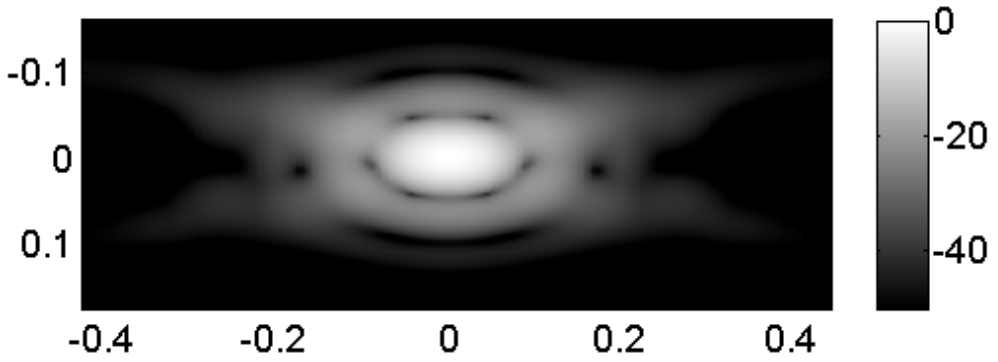

Figure 2.4: The kernel of a 2D PIO filter in spatial domain for a 25 MHz linear array with $d_e = 2\lambda$ using $\beta = 0.3$. The axial direction is along the vertical axis and the lateral direction is along the horizontal axis, both in mm scale.

2.9 The Implemented Filtering Algorithm with GUI

The 2D PIO filtering algorithm has been implemented on Matlab platform with Field II simulation package [43] required. A Matlab graphical user interface (GUI) is also constructed for this algorithm as shown in Figure 2.5. For the purpose of convenience, the regularization parameter β can be specified as digit input or by dragging the slider bar. The demo of the algorithm can be downloaded from http://www.tc.umn.edu/∼wanx0028/.

2.10 Summary

We proposed this post-beamforming filtering algorithm derived from a multiple-scan linear array imaging system model. The single-line model is extended to include data from multiple A-lines (up to a frame) by axial and lateral shifting of the 2D impulse response of the single-line beamforming operation. This discretized propagation model results in a system matrix with attractive properties for computationally-efficient inversion. Specifically, the matrix is block Toeplitz with the matrix elements themselves being Toeplitz due to the range-shift invariance assumption [30]. A direct inversion of the TBBT matrix is possible with Akaike's algorithms [36]. For a matrix with $M \times M$ blocks each with $N \times N$ elements, the Akaike algorithm requires $\mathcal{O}(N^2M)$ memory storage and $\mathcal{O}(N^3M^2)$ operations. The values of N and M are determined by the extent of the ROI, the sampling frequency, and the line density of the imaging system. These result in excessive memory requirement (typically above 100 GB) and number of operations for inversion. A well-known fact is that a banded Toeplitz matrix is asymptotically equivalent to its associated circulant matrix given both matrices are bounded in the strong norm [39]. Similarly, the Toeplitz-block block banded Toeplitz matrices can be approximated by their associated CBBC matrices [40, 41], which not only improves the computational efficiency and reduces the storage cost, but also transforms a usually ill-posed inverse problem to a well-posed FFT problem. Therefore, we are able to use the CBBC matrix to approximate the original propagation matrix, in addition, we extend an efficient inversion algorithm for block circulant matrices [42] specifically for elements being circulant blocks. Correspondingly, the original inversion operation in

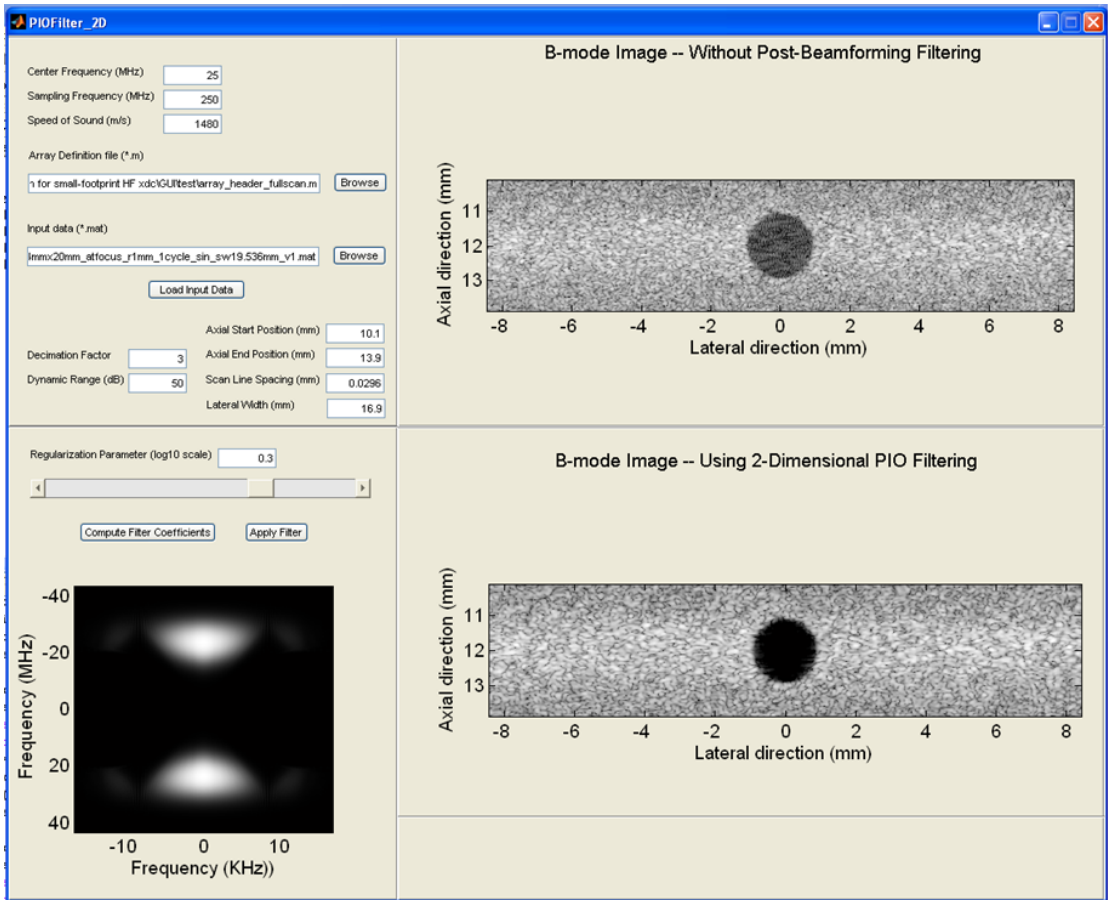

Figure 2.5: The GUI of the 2D PIO filtering algorithm.

spatio-temporal domain is transformed into multiplication operation in two-dimensional frequency domain, preceded and followed by FFT-order DFT operations. Furthermore, regularization is used to avoid the noise amplification due to the inversion of small eigenvalues (or Fourier coefficients). The performance of this filtering algorithm will be analyzed in details in the following sections.

Chapter 3

Enhanced Image Resolution of DMUA

3.1 Introduction

Several image-guided HIFU systems have been introduced for minimally invasive treatment of cancer and other tissue abnormalities [44]. Currently diagnostic ultrasound [45] and MRI [46] are the most commonly used image guidance modalities. Diagnostic ultrasound offers several advantages, including portability, ease of integration, low cost and real-time operation. MRI's major advantages are its high soft-tissue contrast and high spatial resolution, which often result in excellent target visibility and visualization of treated tissue. MRI is also capable of imaging temperature change, which allows for monitoring the progress (and control) of thermal therapy treatments with HIFU [47]. It should be mentioned that diagnostic ultrasound has also been shown to offer a noninvasive means of imaging temperature change in tissues undergoing thermal treatments [48,49], but it currently suffers from limitations when imaging high temperature changes [50]. Other imaging modalities have also been suggested for thermometry, e.g. X-ray CT [51] and electrical impedance tomography [52].

Numerous research groups in the area of image-guided HIFU are considering phased arrays for their respective applications [53–59]. Piezocomposite technology is especially appealing for therapeutic phased arrays due to low cross coupling and relatively high efficiency [60]. In addition, piezocomposite transducers have larger bandwidth than

their piezoceramic counterparts, which allows for the use of therapeutic arrays in pulse-echo mode [29]. These studies highlight the feasibility of real-time dual-mode operation in the therapeutic application of HIFU, where the pulse-echo capability of the DMUA is used to achieve one or more of the following:

- B-mode imaging of the treatment region before and after lesion formation, where changes in echogenicity could be used as an indicator of lesion formation [29, 61–63].
- Monitoring of and real-time compensation for the target motion using speckle tracking methods [64].
- Monitoring of temperature related tissue parameters by application of acoustic radiation force method [50, 65].
- Image-based refocusing of the DMUA for optimal power deposition at the target while avoiding collateral damage to critical structures in the path of the HIFU beam, e.g. the rib cage when targeting liver tumors [66, 67].

Improving the imaging capabilities of DMUAs to levels comparable with diagnostic guidance systems will allow a unique paradigm in image-guided surgery. The inherent registration between the therapeutic and imaging coordinate systems will allow the physician to define the target point(s) where the power deposition is to be maximized directly on B-mode images produced by the DMUA. In addition, critical points where power deposition is to be minimized can be defined on the same image. An optimal solution can be obtained by employing the pseudoinverse multiple-focus synthesis method with additional constraints [68, 69]. This approach has been validated experimentally in a laboratory setting using a prototype 1-MHz 64-element DMUA [66, 67].

We have investigated a number of approaches for improving the image quality of a prototype DMUA that was originally optimized for therapeutic performance. One of them is using the 1-dimensional pseudoinverse filtering method with coded excitation for improving the axial resolution of the current DMUA prototype. Therapeutic arrays typically operate at relatively low frequencies compared with diagnostic imaging array, e.g. 1 - 1.5 MHz is commonly used in abdominal applications [46, 64]. Even with fractional bandwidths in the 30 - 40 % range, the resulting axial resolution is poor, in

the range of 2 - 3 mm. On the other hand, due to the relatively low f-number, the lateral resolution is typically 1 - 1.5 mm ($\approx 1\lambda$). This is the opposite situation to diagnostic arrays with planar or convex geometry and relatively high f-number values where the axial resolution is finer than the lateral resolution. In the case of DMUAs, the resulting point spread function (PSF) is elongated in the axial direction. We thus proposed the use of coded excitation with the 1-dimensional pseudoinverse filtering method to balance the axial and lateral resolution of our prototype DMUA while preserving the contrast resolution of the imaging system [70].

In addition to the bandwidth limitation mentioned above, DMUAs have some special geometric characteristics. The therapeutic efficacy of a DMUA at a target location within the treatment volume is measured by the focusing intensity gain [68]. For a given therapeutic array, the therapeutic operating field ($ThxOF$) of a DMUA is defined as the volume where the focusing intensity gain of the array exceeds a threshold where HIFU beams can produce therapeutic effects [29]. DMUAs have some characteristic geometric features that are dictated by the need for high intensity focusing gain in the $ThxOF$ and electrical-to-acoustic power conversion efficiency. These characteristics are: 1) non-planar concave apertures, 2) large directive elements (width $> \lambda$), and 3) low f-number (≈ 1 or lower). Therefore, conventional delay-and-sum beamforming with such arrays results in nonuniform $IxFOV$ in a region centered around the geometric focus. This nonuniform $IxFOV$ is closely related to the intensity focusing gain profile, which defines the DMUA's $ThxOF$. Special considerations of these geometric characteristics of DMUAs combined with the post-beamforming filtering approach leads to significant improvements in the contrast resolution.

The above work has been focused on the use of pre- and post-beamforming algorithms to improve the imaging performance of a DMUA given its geometry and operating bandwidth [29, 66, 71]. Until recently, these factors were dictated by therapeutic optimization and manufacturing limitations. Advances in piezocomposite transducer technology allow for a choice of materials to meet a variety of power/bandwidth constraints. In addition, fine array lattice definition is now possible with improved manufacturing techniques. These advances open the door for a paradigm shift in the design of DMUAs for optimization of their performance in both imaging and therapy modes. Due to the complexity and high cost of the DMUA geometries in practical applications, the

design optimization must be carried out using appropriate simulation tools. We have previously used CW simulations for the optimization of DMUA for therapeutic performance [72]. However, pulsed wave (PW) simulations are necessary for evaluation of imaging performance in speckle-generating phantoms. Field II simulation program [73] is widely used in the ultrasound imaging community with a number of diagnostic array geometries supported. We have used a modified version of the program to allow for the simulation of concave large-aperture DMUAs. In this project, we present experimental and PW simulation results from a 1 MHz, 64-element prototype DMUA that illustrate its imaging capabilities. These results also serve to validate the new PW simulation model of the DMUA, which is used to investigate the imaging performance of a modified design. In particular, we use the PW simulation model to investigate the effect of fractional bandwidth and aperture sampling on the imaging performance of the DMUA. A modified DMUA design with different aperture sampling in imaging and therapy modes is presented. This design is based on fine sampling of a concave aperture with the same dimensions as our current 1 MHz prototype. A uniform sampling grid employing 128×8 elements is used to cover the available concave aperture. Using interconnection circuits for element grouping in imaging and therapy modes, the DMUA can be configured as a 64×1 array in therapy mode and a 128×1 array in imaging mode on the same aperture. The imaging array has finer sampling to reduce grating lobes and higher f-number in the elevation direction to extend the *IxFOV*. Simulation results from the modified DMUA design are also provided to illustrate the improvements in imaging performance. This additional work on the design of DMUA prototype is also placed in the appendix of this dissertation.

3.2 DMUA Prototype

We have designed a 64-element, 1-MHz, linear concave array (on a spherical shell with 100 mm radius) for HIFU applications. The array has a fairly low f-number of 0.8 in order to maximize the array focusing gain in the intended *ThxOF* as described in [29]. In order to minimize the channel count and maintain high driving efficiency, we have sampled the aperture using 1.5×50 mm^2 elements with center-to-center spacing of 2 mm as shown in Figure 3.1. Clearly, this $1.33\bar{3}\lambda$ spacing in the lateral direction results

in grating lobes. However, computer simulations were used to establish that these grating lobes were kept at least -25 dB below the focus for every focal point within the *ThxOF*. For this particular prototype, the *ThxOF* was specified as a circular disk 3-cm in diameter and centered at the geometric center. Simulation results of the focusing intensity gain profile for this prototype have shown that the *ThxOF* extends from 80 - 120 mm axially and ±20 mm laterally [29]. The focusing intensity gain within this region was in the range of 700 - 1150 with the maximum intensity gain achieved at the geometric focus. With ≈ 5 W/cm^2 available at its surface, the prototype is capable of producing focal intensities from 3500 - 5750 W/cm^2 within its *ThxOF*.

The array was fabricated using HI-1 piezocomposite technology (Imasonic, Besançon, France) [60] and was shown to produce up to 250 W with efficiency ≈ 60 %. In therapeutic mode, the DMUA was shown to have a 37% bandwidth around the center frequency of 1.1 MHz [29]. In pulse-echo mode without matching, the DMUA has two predominant resonance frequencies, at 1.1 and 2.1 MHz. These characteristics are consistent with an earlier prototype that was described in [74].

3.3 Coded Excitation

It is well known that in conventional pulse-echo ultrasound imaging, there is a trade-off between resolution and penetration depth under the limit of peak acoustic power. Narrower pulses will have wider bandwidth and better resolution, but suffer lower SNR leading to less penetration. Using coded waveforms as excitation enables elongated pulses for higher SNR.

Coded excitation was first explored in Radar systems [75] and later applied to ultrasound imaging since 1970's [34]. Many challenges appeared in the early investigation of using coded excitation for ultrasound imaging such as, limited available transducer bandwidth, dynamic receive focusing distortion, and frequency-dependent attenuation. All of these factors results in poor compression and high sidelobe levels, consequently impeding the research on coded excitation.

Recently, more attention has been brought to this topic due to several reasons:

1. Advancement in transducer manufacturing technology has allowed large transducer

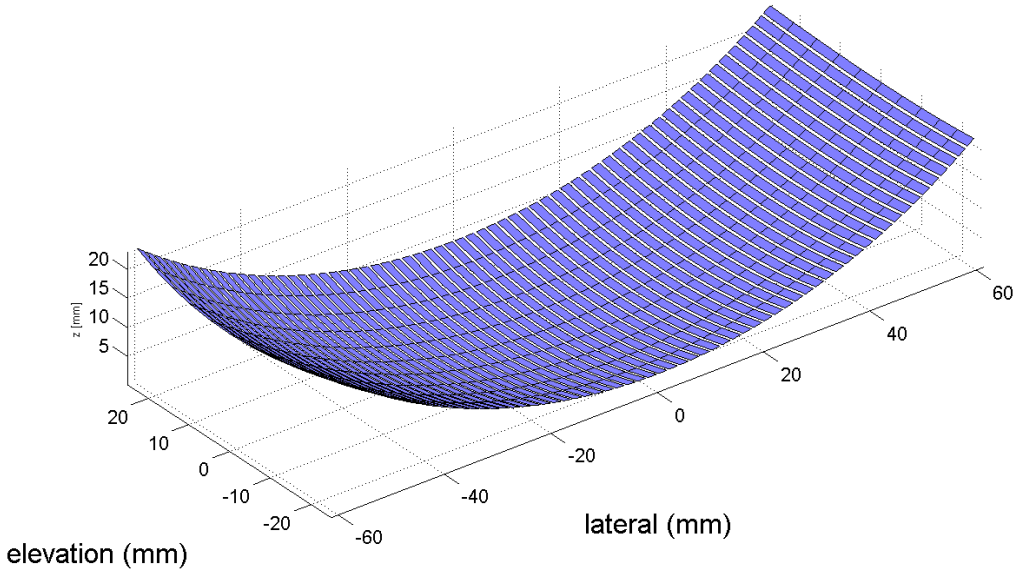

Figure 3.1: Dual-mode ultrasound array geometry. The array elements are shown segmented in the elevation direction. This segmentation is for simulation purposes only.

bandwidth to become available in commercial ultrasound scanners: for example, Ultrasonix L-14-5/38 transducer has about 100% bandwidth around center frequency 9 MHz.

2. Multilevel and long duration waveform generation has been enabled in some ultrasound imaging systems. For example, coded waveforms were introduced to General Electric diagnostic ultrasound scanners in 1990's.

3. Insistent work and effort have been conducted by pioneer researchers on various critical issues in this topic. For example, Chiao and Hao showed clinical images using Golay codes to highlight the practical usage of coded waveforms [31]; Misaridis and Jensen compared different classes of coded waveform and considered a linear chirp as a robust compression waveform for frequency-dependent attenuation [34].

3.3.1 Coded Waveforms

In this evolving field, approaches using different codes have been proposed: PN sequences [30, 76], Golay codes [31], chirps [34]. A nice summary of coded waveforms was introduced back in 1971, and the coded waveforms are categorized into 4 groups according to the ambiguity function [75]:

1. Constant-carrier pulse. A constant-carrier pulse is the simplest form of the waveform we can use. The short duration constant-carrier pulse is the excitation used in the conventional pulse-echo ultrasound imaging. The reasons why it is a good choice for ultrasound imaging are simple implementation or low complexity, good range resolution due to its large bandwidth, low sidelobe level with proper envelope and robustness to the frequency-dependent attenuation due to its short duration. The well known disadvantages are poor SNR resulted from low time-bandwidth (TB) product and high correlation in the imaging field.

2. Pulse compression signals with thumbtack ambiguity function. These waveforms have time-bandwidth product larger than unity, thus may producing higher SNR than constant-carrier pulse. Sets of Orthogonal codes are used to reduce the correlation in the field [30]. The major problem with this type of waveforms is the high sidelobe level after compression: average $\propto 1/TB$, although it is one

of those types of waveforms which are able to achieve sharpest mainlobe peak. A special case in this family is complementary codes which are able to suppress sidelobe level by adding two or more transmitted sequences with equal-magnitude, opposite-sign sidelobes [31].

3. Pulse compression signal with sheared ridge ambiguity function – linear chirp. Linear chip is a special type of pulse compression signal because it has a large time-bandwidth product as other pulse compression signals while maintaining low sidelobe level as the constant-carrier pulse. It is also robust to the frequency-dependent attenuation because the frequency shift mismatch can be translated to time shift, thus guaranteeing the compression quality.

4. Pulse trains. This type of waveforms is the least investigated because of the range ambiguity for ultrasound imaging. However, it is worth mentioning due to its capability of suppressing sidelobe level, at the same time, achieving sharp mainlobe peaks.

Some researchers did not select the exciting waveforms according to the above classification. Their approach is obtaining spatio-temporal codes capable of correcting the distortion in heterogeneous, lossy medium by iteratively calibrating/training the system [77]. This way of choosing coded waveform cast light on optimum waveform design for specific applications/scenarios.

3.3.2 Receive Filter

A Matched filter appears often as the receiving/compressing filter because it achieves the highest SNR at the peak of the compressed pulses [31]. The highest possible SNR is proportional to the time-bandwidth product of the transmitted waveforms. However, matched filters do not take system noise or clutter distribution into account and this type of filter can not balance performance parameters for optimum solutions of specific applications.

On the contrary, the pseudoinverse filter has the capability of combining compression, decoupling, noise/clutter reduction and performance adjustment at the same time. This will be further illustrated and explained in the following sections.

3.4 1D Post-Beamforming PIO Filter Design for Coded Excitation

For example, we transmit a linear chirp signal $c(t)$ covering the frequency band of 0.5-1.5MHz as illustrated in Figure 3.2(a). The frequency response of the matched filter is $C^*(f)$, the complex conjugate of the Fourier transform of $c(t)$. The frequency response of the pseudo-inverse filter, $P(f)$, is defined as

$$P(f) = \frac{C^*(f)}{S_s(f) + \beta S_n(f)}, \tag{3.1}$$

where, $S_s(f) = |C(f)|^2$ is the spectral density of the signal, $S_n(f)$ is the spectral density of the noise and β is a regularization parameter for the noise term. For illustration purpose, additive white Gaussian noise (AWGN) model is assumed. As shown in Figure 3.2(b)-Figure 3.2(d), the frequency response of the pseudo-inverse filter changes with the value of β. Specifically, when we set the regularization parameter $\beta = 0$, the filter behaves as an inverse filter, $1/C(f)$, with widest bandwidth and highest noise floor. It is obvious that the pulse width in the time domain is inversely proportional to the bandwidth. Therefore, theoretically, the inverse filter obtains the highest axial resolution but with the lowest SNR. On the other extreme, when the regularization parameter β is large enough so that $\beta S_n(f)$ dominates the denominator, the filter behaves as a matched filter as shown in Figure 3.2(d). This solution maximizes the SNR, but may reduce the axial resolution (due to the reduced overall bandwidth of the system-matched filter cascade). The use of the Pseudoinverse filter allows us to shape the spectrum of the compressed received signal by regularized inversion of the system frequency response at frequencies where the SNR is sufficiently high. The appropriate value of β can be determined from the SNR of the system as a function of the frequency. The objective is to achieve the highest axial resolution level (as close as possible to the lateral resolution) at an acceptable level of SNR.

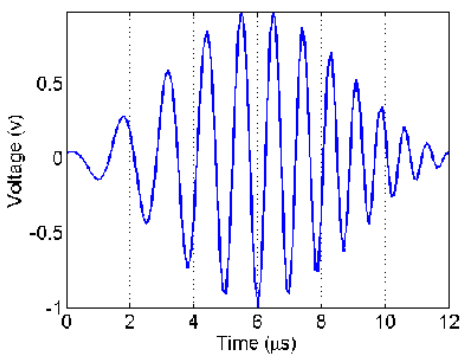

(a) Chirp signal

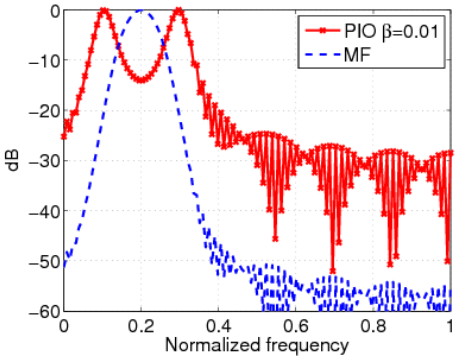

(b) Filter with β=0.01

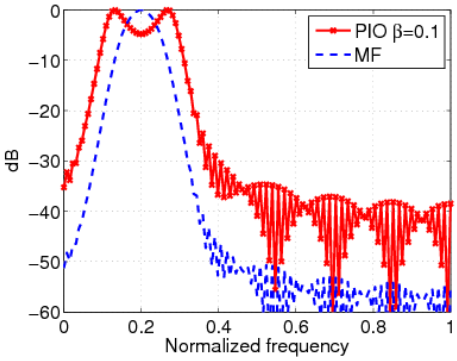

(c) Filter with β=0.1

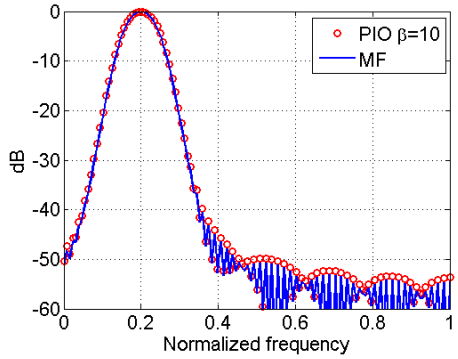

(d) Filter with β=10

Figure 3.2: Illustration of the pseudo-inverse compression filter frequency response designed for a Gaussian chirp transmit waveform. The effect of the regularization parameter, β, on the frequency response of the PIO is also shown.

3.5 Simulation and Experiment Setup

3.5.1 Simulation Models

Both continuous wave (CW) and pulsed wave (PW) simulation models were developed for the DMUA. The CW simulation model was used for beam synthesis and field computation as described in [68]. The CW simulation model was used in determining the DMUA design parameters based on the following considerations:

- The aperture size, degree of geometric focusing, and operating therapeutic frequency are determined by target depth, available acoustical window and the required focusing gain to achieve a desired therapeutic endpoint at the target [29].
- The aperture sampling (element size and spacing) is determined by the size of the *ThxOF* and the maximum acceptable grating lobe levels to avoid therapeutic heating outside the target volume. The element size (directivity) must be chosen such that the drop in intensity gain at the focus is within a specified level (e.g. 1 - 2 dB) throughout the *ThxOF*. Element size may also be determined by the type of amplifier used in driving the element and electrical-to-acoustic power conversion efficiency.

The availability of $\approx 40\%$ fractional bandwidth for our DMUA prototype encouraged us to develop a PW simulation model for analyzing its imaging performance. The PW model was based on the Field II simulation package [43, 73], which is widely used in the ultrasound imaging community and provided us with valuable tools for simulating speckle-generating targets. Due to the concave nature of our DMUA, we had to modify the program to support the concave array structure shown in Figure 3.1. Note that the slicing for each element in the elevation direction is only for simulation purposes. This is due to the fact that Field II simulates curved elements by discretizing their surfaces using linear, mathematical elements. We have experimentally sampled the actual impulse response and the excitation for use in the Field II simulations.

3.5.2 Experiment Data Collection

Array elements were connected to a transmitter and a receiver through a 4×64 matrix switch (Tektronix VX4380). For conventional pulse-echo experiments, a pulser/receiver

(GE Panametrics 5800) was connected to the transmit and receive terminals on the matrix switch with the receiver connected to a 20 Msample/s 23-bit digitizer (Agilent HP E1437A). Coded excitation experiments were performed by connecting an arbitrary waveform generator (Agilent AG33250A) and a power amplifier (ENI A150) to the transmit terminal on the matrix switch.

3.5.3 Imaging Targets

A variety of imaging targets are used to illustrate the imaging performance of the DMUA:

Wire Target Array: was used to illustrate the spatial resolution of the DMUA as well as illustrating the extent of the *IxFOV*. It was also used to demonstrate the beamforming accuracy throughout the imaging field. We used 230 μm thermocouple wires tightened on a Plexiglas frame that could be attached on the DMUA holder so that the wires are placed from -50 mm to 50 mm along lateral direction and 40 mm to 150 mm along axial direction (as shown in Figure 3.3). The center of the wire target array was positioned at the geometric focus of the DMUA. The spacing between each pair of wires is 10 mm.

CIRS Model 55 3D Contrast Phantom [78]: was used to illustrate the enhanced contrast resulting from accounting for element directivity and gain compensation in a challenging 3D egg-shaped contrast target used for evaluating diagnostic scanners. It was also used to assess the loss in contrast resulting from the use of pseudoinverse post-beamforming filtering with coded excitation.

3.5.4 Synthetic Aperture Imaging

We use synthetic aperture imaging technique [14] to obtain images with 2-way (transmit-and-receive) dynamic focusing. This provides the highest quality image possible with the current prototype using conventional delay-and-sum beamforming. In this mode, the RF data from an image pixel at $P(x_p, z_p)$ in a medium with uniform speed of sound,

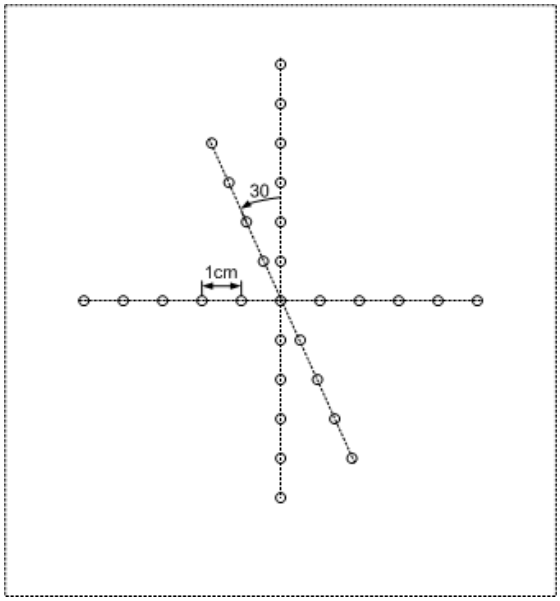

Figure 3.3: Geometry of the wire target array phantom. The center wire was positioned at the geometric focus of the DMUA.

c, is computed by:

$$I(x_p, z_p) = \sum_{i=1}^{64} \sum_{j=1}^{64} A_i \cdot B_j \cdot s_{i,j} \left(\frac{R_{ip} + R_{jp}}{c} \right), \tag{3.2}$$

where A_i and B_i are, respectively, the transmit and receive apodization weights, R_{ip} and R_{jp} are, respectively, the distances from the transmitting and receiving elements to the image pixel P, and $s_{i,j}(t)$ is the echo received by element j when transmitting with element i. Other imaging scenarios can be easily performed by specializing the image formation (3.2).

The waveforms, $s_{i,j}(t)$, are either collected experimentally using the system described in Section 3.5.2 or generated using the modified Field II with the DMUA geometry described in Section 3.2. In both cases, a sampling frequency of 10 MHz was used. We note here that the use of the matrix switch did not allow for collecting echo data at element i when that same element was used as a transmitter. This was accounted for in the beamforming program with both experimental and simulation data. It had minimal effect on the quality of the reconstructed images.

3.6 Assessment of Imaging Performance

3.6.1 Spatial Resolution

For wire target images, the 6-dB width and length of the envelope were used to measure the lateral and axial resolution, respectively. For quality assurance and scatterer phantoms we used the speckle correlation cell size as described in [79]. Uniform speckle regions from the test object area were identified to compute the average speckle correlation cell size in the axial and lateral directions as follows:

$$S_{cx} = \int_{-X}^{X} \frac{C_I(x,0)}{C_I(0,0)} dx \qquad S_{cz} = \int_{-Z}^{Z} \frac{C_I(0,z)}{C_I(0,0)} dz, \tag{3.3}$$

where S_{cx} and S_{cz} are, respectively, the lateral and axial cell size values and $C_I(x,z)$ is the 2D intensity autocovariance function. The integration limits X and Z are chosen to be large enough to allow the magnitude of the autocovariance to drop to negligible levels. The integrals are evaluated numerically in Cartesian coordinates using the trapezoidal rule to obtain the speckle cell size in the axial and lateral directions.

3.6.2 Contrast

The contrast ratio (CR) is defined as following

$$CR = 10 \log_{10} \left[\frac{\bar{I}_2}{\bar{I}_1} \right], \tag{3.4}$$

where $\bar{I}_2$ and $\bar{I}_1$ are the average intensities in the region of interest (e.g. cyst) and a reference region, respectively.

3.7 Results

3.7.1 Verification of Simulation Model Using Wire Target Array

SA image data from the wire target array shown in Figure 3.3 was collected experimentally using the setup described in Section 3.2. The same array geometry was simulated using Field II to obtain the equivalent SA waveforms. Figure 3.4(a) shows the 50-dB grayscale image of simulation data and Figure 3.4(b) shows the image of experimental data formed by (3.2). Both images show the wire targets correctly registered with maximum intensity at the DMUA geometric center and reduced intensity from targets away from the center in all directions. The extent of the axial PSFs is similar in both images throughout the imaging field. The lateral PSF in the experimentally acquired image data shows higher sidelobes due to heterogeneous element gains that were not corrected for. In addition, one can see the cumulative grating lobe patterns due to the multiple wire targets. These grating lobe patterns, together with the reduction in target intensity away from the geometric center, demonstrate the reduced imaging dynamic range outside the *IxFOV*. The results of this experiment demonstrate that the DMUA has a *IxFOV* which extends by $\approx \pm$ 20 mm from the geometric center in the lateral direction. In the axial direction, the *IxFOV* appears to extend by more than $\pm$ 30 mm from the geometric center. They also provide a partial validation of the simulation model, which will be used in the analysis and design of new DMUA geometries.

3.7.2 Special Considerations

The results shown in Figure 3.4(a) and Figure 3.4(b) are based on (3.2) without accounting for element directivity or array gain. We have shown experimentally [71] that

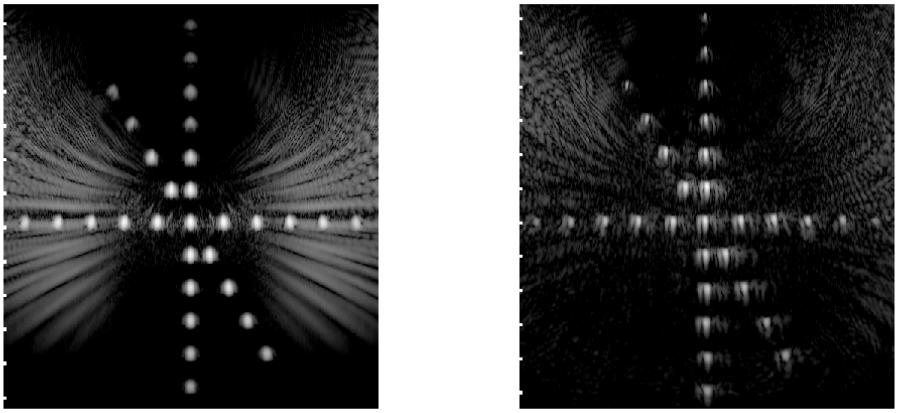

(a) Simulated data.

(b) Experimental data.

Figure 3.4: Grayscale images (50 dB) of the wire target array phantom using SA pulse-echo data.

accounting for these effects improves the contrast resolution by extending the imaging dynamic range by reducing the grating lobes (element directivity) and improving the uniformity of the target intensity within the *IxFOV* (array gain compensation). These special considerations are illustrated based on simulated SA waveforms to avoid repetition.

Element Directivity

DMUA elements are 1-λ wide, which may be too directive, especially for near-field pixels. The element directivity weighting function is given as follows [66]:

$$D(\theta) = \frac{\sin[kd\sin(\theta)/2]}{kd\sin(\theta)/2}, \tag{3.5}$$

where, $k = 2\pi/\lambda$, d is the element width and θ is the angle between the vector from the element to the focusing pixel P and the vector from the element to the geometric focus. The 6 dB width of this function is $\pm 25^\circ$. At 100 mm range, the width of the directivity pattern is ± 46.6 mm. After considering transmit and receive element directivities $D(\theta_i)$ and $D(\theta_j)$, respectively, the beam-forming equation (3.2) becomes:

$$I(x_p, z_p) = \sum_{i=1}^{64}\sum_{j=1}^{64} A_i \cdot B_j \cdot s_{i,j}\left(\frac{R_{ip} + R_{jp}}{c}\right) \cdot D(\theta_i) \cdot D(\theta_j). \tag{3.6}$$

Using (3.6) in beamforming the simulated SA waveforms for the wire target array produces the 50-dB image shown in Figure 3.5. One can see clearly the reduction in cumulative grating lobes compared to the SA imaging without accounting for element directivity. More importantly, accounting for element directivity in beamforming improves the signal to noise ratio of the beamformed data by suppressing signal components from directions where the element directivity is very low. This effectively reduces the noise contribution to element data before beamforming. This process can be understood as a pre-beamforming spatial matched filtering operation.

Gain Compensation

The concave nature of the DMUA is dictated by therapeutic design considerations. The aperture size and radius of curvature together with the element size and spacing define

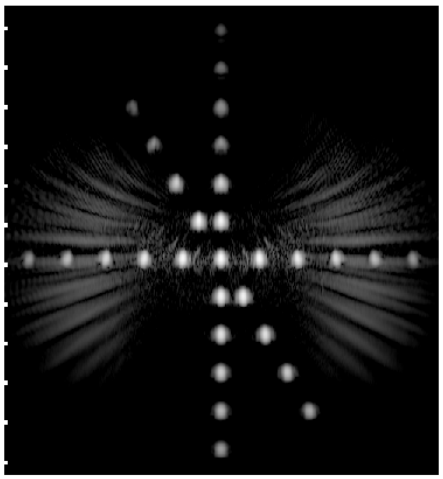

Figure 3.5: Grayscale image (50 dB) of the wire target array shown in Figure 3.3 using (3.6) with simulated SA pulse-echo data.

the DMUA's $ThxOF$. The $ThxOF$ defines a region around the geometric focus where the focusing gain of the array provides therapeutic levels suitable for HIFU application. Outside the $ThxOF$, the focusing gain is significantly lower [66]. Incidentally, the intensity focusing gain is the same as the two-way array gain in synthetic aperture imaging mode described above. This means that the $IxFOV$ is associated with the $ThxOF$. The $IxFOV$ can be extended by performing gain compensation after beamforming.

The field strength at a given pixel should be compensated as follows

$$I_g(x_p, z_p) = I(x_p, z_p)/G(x_p, z_p), \tag{3.7}$$

where, $G(x_p, z_p)$ is the square root of the intensity gain.

The need for gain compensation can be appreciated by examining the images resulting from the wire target array. The intensity levels of the wire targets drop gradually away from the geometric center, both axially and laterally. This is due to the DMUA's high focusing gain near the geometric center, which could be predicted by CW simulations. In this study, however, we simulated a uniform phantom (-33.4 mm to 33.4 mm in lateral direction and 70.2 mm to 178.8 mm in the axial direction) to illustrate the effect of gain compensation. As shown in Figure 3.6(a), the image appears brighter around the geometric center and darker in the prefocal/postfocal regions and on the sides. Applying gain compensation by using (3.7), the image shown in Figure 3.6(b) appears much more uniform. This result can be quantified by computing the contrast ratio between intensity levels from selected regions just outside $IxFOV$ and the geometric center. With reference to (3.4), $\bar{I}_2$ is the average intensity in a region inside of a square region centered at the the geometric center and $\bar{I}_1$ the average intensity in the same size region centered as specified in Table 3.1 (center position coordinates in mm). One can see that image uniformity is improved within and outside the $IxFOV$. This is important for properly imaging extended contrast targets as shown in Figure 3.6. We have also collected SA pulse-echo data with the CIRS Model 55 3D quality assurance phantom used as an imaging object. The phantom was positioned so that the top portion of the large egg-shaped contrast object was in the DMUA's $IxFOV$. The data collection was performed with both the DMUA and the phantom submerged in water with 60 mm spacing between the front surface of the phantom and the apex of the array. SA

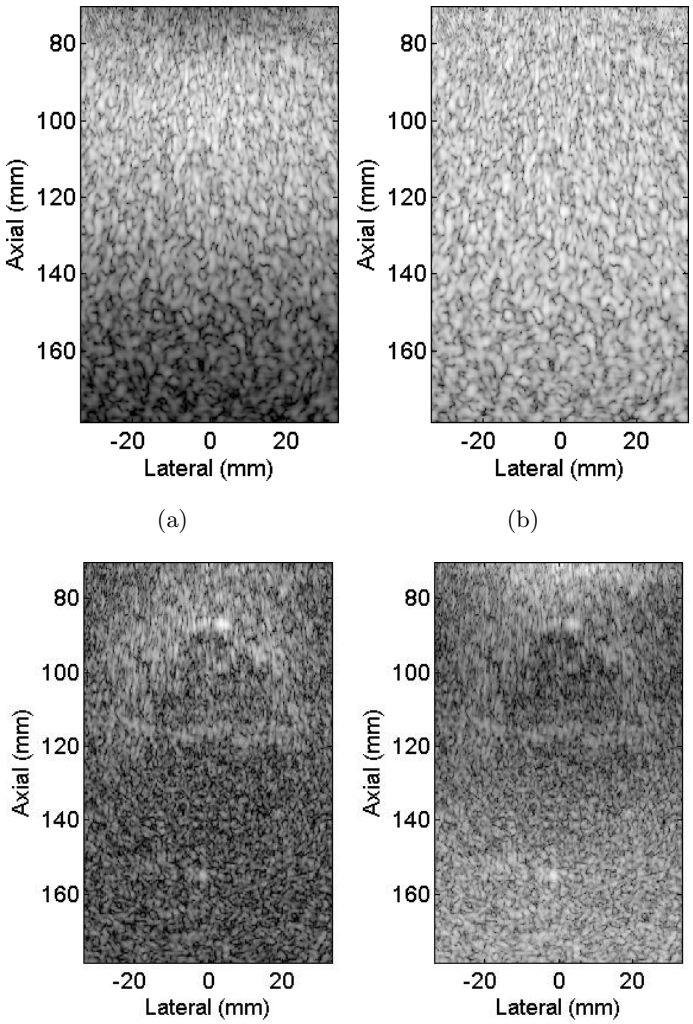

Figure 3.6: Grayscale images (50 dB) of a simulated uniform scatterer phantom and the CIRS Model 55 3D quality assurance phantom using experimentally collected SA pulse-echo data.

	Pre-focal (0,52.2)	**Post-focal** (0,152.2)	**Left** (-32.2,100)	**Right** (32.2,100)
Without Gain Compensation	20.3 dB	18.5 dB	2.45 dB	2.74 dB
With Gain Compensation	4.5 dB	3.6 dB	0.28 dB	0.22 dB

Table 3.1: CR Values for Selected Regions.

beamforming was performed on the collected data and the resulting grayscale images (50-dB) are shown in Figure 3.6 without and with gain compensation. To quantify the effect of gain compensation, we computed the CR value for an elliptic region (with major and minor axes of 80 mm and 30 mm in the axial and lateral directions). The ellipse was centered at [32 0 152] mm outside of the egg-shaped contrast object with reference to a region with the same size and shape inside of the object. A negative contrast of -1.4 dB was measured without gain compensation. The corresponding value after gain compensation was 7.6 dB.

3.7.3 Coded Excitation Results Using 1D Pseudoinverse Filter

SA pulse-echo data was collected using a linear chirp transmit pulse covering frequency band of 0.5 – 1.5 MHz with the CIRS Model 55 quality assurance phantom used as an imaging target. The phantom was in the same position described above for the conventional pulse-echo data collection. We used a matched filter and a pseudoinverse filter with a β of 0.1 to compress the received echo after beamforming. A colored noise model was used in (3.1) to account for reverberation noise below 1 MHz. A value of $\beta = 0.1$ was chosen to maximize the bandwidth without amplifying the broadband high frequency noise components. The frequency response of the pseudoinverse filter is very well behaved as can be seen in Figure 3.7. Matched and pseudoinverse filters were (separately) applied to beamformed RF data before envelope detection and log compression. Resulting grayscale images (50 dB) are shown in Figure 3.8. One can see that the speckle from the pseudoinverse filter appears shorter along axial direction compared to that from matched filter. We used speckle correlation cell size [79] to quantify the resolution as shown in Table 3.7.3. One can see that using pseudoinverse filter improved the axial resolution by 30% compared to the result from the matched filter. Significantly, because the achieved axial resolution is closer to the lateral resolution, the image obtained using the pseudoinverse filter appears more uniform. The contrast ratio for the contrast target was 7.6 dB for pulse-echo, 7.8 dB for matched filter and 6.6 dB for pseudoinverse filter. This shows that significant improvement in axial resolution was achieved at the cost of 1.2 dB loss in contrast for this object.

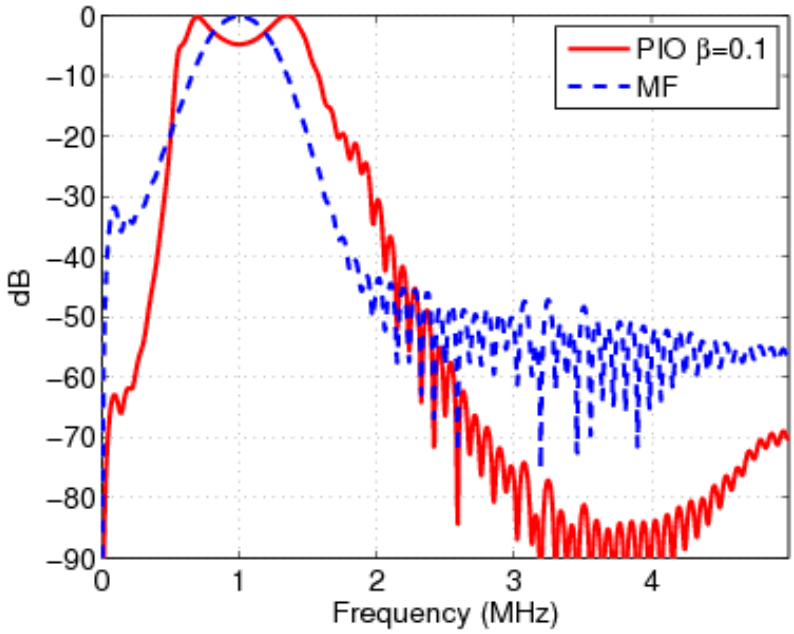

Figure 3.7: Frequency response of designed pseudoinverse filter.

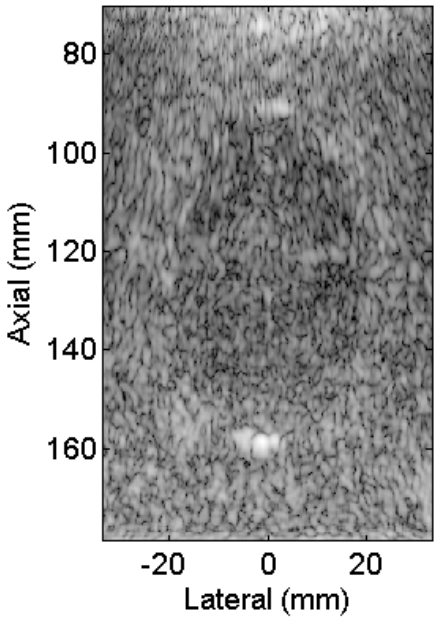

(a) matched filter

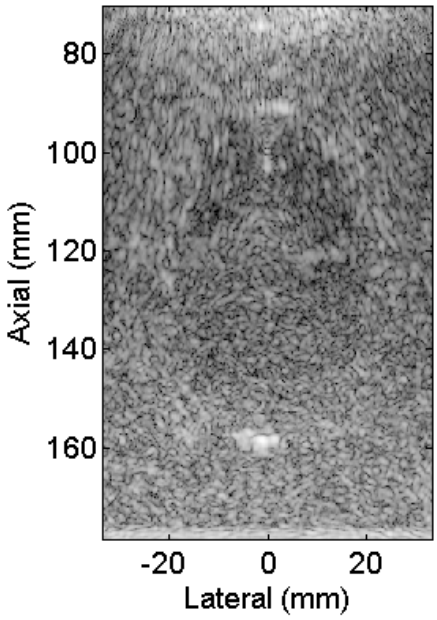

(b) pseudoinverse filter

Figure 3.8: Grayscale images (50 dB) of the CIRS Model 55 quality assurance phantom using experimentally collected SA pulse-echo data. A chirp transmit pulse was used together with matched filter, (a), and a PIO filter, (b).

	calculated	**pulse-echo**	**MF**	**PIO**
Axial	2.8 mm	2.77 mm	2.5 mm	1.65 mm
Lateral	1.1 mm	1.06 mm	1.28 mm	1.06 mm

Table 3.2: Egg phantom speckle correlation cell size.

3.8 Conclusion

The use of dual mode ultrasound phased arrays in image-guided surgery is becoming a reality. We presented experimental and simulation results for characterization of the imaging capabilities of a 1 MHz prototype DMUA. The regularized post-beamforming pseudoinverse filtering together with coded excitation has been shown to improve the axial resolution of a DMUA prototype by 30% without significant loss in contrast ratio. Gain compensation and accounting for element directivity have been shown to extend the DMUA FOV. A Field II-based simulation model of the concave DMUA has been developed as a tool to assess the imaging performance of DMUA prototypes. This will help in the design of future DMUA prototypes. Wire target array images obtained by beamforming experimental and simulation data show that the array simulations capture the array geometry and bandwidth characteristics. Listed in Section A, these images show that the PSF, the Ix-FOV, and the grating lobe structure are well predicted by the simulation model. The simulation model was then used to evaluate the effect of varying DMUA design parameters (FBW and aperture sampling) on the PSF and the contrast ratio of cyst targets positioned at various locations within the IxFOV. Finally, based on this simulation study in Section A, we have proposed a modified DMUA design that results in significant enhancement in the imaging performance in terms of spatial and contrast resolution as well as expanded IxFOV. Using simple element interconnection schemes in imaging and therapy modes, the modified DMUA can achieve this enhancement while simultaneously maintaining the therapeutic aperture sampling of the existing DMUA design that has been optimized for therapy. This implies that the improvements in imaging performance of the DMUA will not significantly compromise its predicted therapeutic performance.

Chapter 4

Contrast Enhancement for High Frequency Ultrasound Imaging

4.1 Introduction

High-frequency ultrasound has been used for noninvasive visualization of living tissues at or near microscopic levels in many clinical or biological applications, such as dermatology [80, 81], ophthalmology [2, 82, 83], intravascular intracardiac imaging [84–88], nonvascular endoluminal imaging [89], cartilage imaging [90,91], and small-animal studies [92,93]. Researchers have recently achieved some success in extending the resolution to microscopic levels [2, 24, 28] using high-frequency systems with single-element transducers. At least one high frequency ultrasound imaging system of this kind has been commercialized for small-animal research applications.

Various array transducers for HFUS imaging applications have been proposed recently [20–24, 26–28]. These efforts are motivated by the success of array transducers in clinical applications in the frequency range of 2 - 16 MHz. A number of transducer materials and fabrication methodologies have been developed in recent years [23, 27, 28, 94]. The benefits of these advances in materials and fabrication techniques have not been fully realized for high frequency arrays above 20 MHz. One of the primary challenges for current transducer technologies is the element size requirements in this frequency range. Smaller size elements in the 30 - 60 μm range may be difficult to realize using existing techniques. Even if the fabrication problems are solved, additional problems

due to increased cross coupling, increased element impedance, and increased variability in element sensitivity may arise. Therefore, based on the existing knowledge of transducer materials and fabrication methodologies, it is expected that high frequency arrays in the range of 25 - 35 MHz will be realized with 1.5 - 3 λ pitch (rather than the desirable range of 1 - 1.2 λ for linear array imaging). Conventional beamforming with these coarsely sampled arrays results in increased grating lobe levels leading to reduced dynamic range and loss of contrast.

We will use the 2-dimensional post-beamforming pseudoinverse filtering algorithm for restoring the lost contrast due to the coarse sampling in lateral aperture. A HFUS linear array pulse-echo imaging models is constructed based on Field II [43] which is a widely-used simulation program in the ultrasound imaging community. We will first test the The imaging performance using simulated phantoms: such as a unit point scatterer or a speckle-generating phantom with a cyst. 25 MHz Arrays (60% fractional bandwidth) with finely-sampled aperture ($\lambda/2$ element spacing) and coarsely-sampled aperture (2λ element spacing) were respectively simulated to be the references for comparison. The simulation result from the coarsely-sampled array is then filtered by the 2D PIO filter with proper regularization. Finally, the comparison between the filtered result and the above references will show how much improvement is by using our algorithm for high-frequency coarsely-sampled ultrasound arrayscompared to that of the finely-sampled equivalent. The quantified spatial resolutions and contrast are measured for validation. In addition, different aspects related to this algorithm are discussed such as computational complexity, trade-off between resolutions and SNR during regularization, the limitation with reduced lateral sampliing.

An important characteristics of this filtering algorithm is that our regularization approach leads to well-behaved PSFs with properties that change gradually with increasing values of the regularization parameter, β. In particular, the axial and lateral dimensions of the PSF increase approximately as a sigmoid function with respect to $\log \beta$. Furthermore, the contrast ratio measurements from cyst targets also increases approximately as a sigmoid function with respect to $\log \beta$. This feature provides user-friendly convenience of choosing a value of β for achieving the desired levels of imaging performance (contrast and resolutions), which can be easily implemented as a knob on ultrasound scanners.

Further verification of the performance of this filter has been conducted on imaging quality-assurance phantoms, porcine eye *in vitro* and human carotid artery *in vivo* using Ultrasonix RP system [95] with linear array probes. We will show similar performance of this algorithm in various applications in terms of not only the contrast restoration but also the smooth regularization process. These experiments act as test cases for this algorithm in more realistic situations.

4.2 Simulation Results

4.2.1 25 MHz Small-Footprint HFUS Array Prototype

The objective is to image the heart-valve equivalent (HVE) *in vitro* and ultimately *in vivo* using HFUS. The array prototype described here serves as a reference for future prototypes utilizing coded-aperture and/or coded excitation. For the purposes of this paper, we have simulated a linear array prototype with the following parameters:

- center frequency: $f_0 = 25$ MHz;
- fractional bandwidth: FBW = 60%;
- active aperture size: 6 mm;
- lateral focal distance: 12 mm;
- elevation height: 2.5 mm;
- elevation focal distance: 15 mm
- lateral pitch: 0.5 $\lambda(\approx 30\ \mu\text{m})$, 2 $\lambda(\approx 118\ \mu\text{m})$

The operating frequency was determined based on single-element imaging results of HVE samples [96]. The remaining parameters of the prototype were chosen based on recent publications on the design and manufacture of HFUS arrays [20–24,26–28] and potential HFUS imaging applications [2], such as intravascular and intracardiac imaging [84–88], skin imaging [80, 81], ocular imaging [82, 83], nonvascular endoluminal imaging [89], cartilage imaging [90, 91], and small-animal study: developmental biology [92], tumor

biology [93]. The wavelength is 59.2 μm given the specified speed of sound. The finely-sampled array is assumed to have $d_e = 0.5\lambda$, which utilizes elements with width of $\approx 30\mu$m. This is currently very challenging and expensive even for the transducer manufacture technology in the research stage. The coarsely-sampled array is assumed to have $d_e = 2\lambda$, which utilizes elements with width of $\approx 120\mu$m. This can be easily achieved using modern transducer technology.

The simulation results of this prototype with two lateral pitches consist of two parts. In the first part, the PSF was used to characterize the spatial resolutions and side lobe levels, especially lateral side lobe level of the systems, consequently showing the comparison of the intrinsic properties of the imaging systems for different lateral pitches. This will give us a quantitative illustration of the degradation of fundamental characteristics of an imaging system due to coarse sampling of the lateral aperture. Next the 2D PIO filtering approach is applied to the result obtained from the coarsely-sampled array. The results will show that the filtering algorithm affects the fundamental properties of imaging system: spatial resolutions and lateral side lobe level. In the second part, a speckle-generating cyst phantom is used to visually illustrate the contrast measurements of the imaging systems for different lateral pitches. This measurement is quantified by computing the contrast ratio. Similarly, the proposed algorithm is applied to the cyst phantom result obtained from the coarsely-sampled array, and a regularization process is illustrated with contrast ratio and speckle correlation cell (SCCS) size measurements for different regularization parameters.

Point spread function

In this section, the point spread function (PSF) is used to characterize the spatial resolutions and grating lobe levels of the specified imaging systems with finely-sampled aperture, coarsely-sampled aperture and the results filtered by 2D PIO filter with regularization for the coarsely-sampled aperture case.

Figure 4.1 shows the 60-dB grayscale images of the PSFs for 0.5 λ lateral pitch (a), 2 λ lateral pitch (b), respectively. The images are defined in a 2.5 $\times$ 19.5 mm^2 region with the unit scatterer at the focus [0 0 12] mm. The lateral dimensions of the images are specified long enough to include the 1^{st}-order grating lobe due to the coarse sampling as shown in Figure 4.1(b). Figure 4.1(a) illustrates the ideal image quality

with Nyquist sampling: the lateral sidelobe level is far below -60 dB as plotted with solid line in Figure 4.2(b) and the spatial resolutions are decided by the imaging system as listed in table. However, when the lateral element-to-element spacing increases, the grating lobes move closer to the image center along the lateral direction with increased magnitude. With 2 λ lateral element-to-element spacing, the grating lobes appear at about $x = \pm 6$ mm as shown in Figure 4.1(b) and the contour plot shows the shape and the magnitude of the grating lobes in this case. Correspondingly, the sidelobe level of the lateral PSF increases to about -55 dB as shown with dotted line in Figure 4.2(b) and the 43 dB increment is contributed by the grating lobe artifacts.

As illustrated in Section 2.7, the two-dimensional PIO filter can be regularized to balance the trade-off between spatial resolutions and SNR. In this case, the main noise term brought by this problem is the lateral grating lobe artifacts, in addition, the axial sidelobe levels of the PSFs are far below -80 dB within the range of our regularization; therefore, we only compare the lateral sidelobe levels of the PSFs and the -6 dB width of the PSFs' peaks to show the adjustment in SNR and resolutions. For instance, Figure 4.3 shows the lateral PSFs of the results filtered by the 2D PIO filter with regularization parameter β =0.001, 0.1 and 1. From Figure 4.3, it is easy to observe that the lateral sidelobe level decreases with increased β values while the lateral resolution becomes worse. Naturally, the axial resolution is also influenced by the regularization, but less dramatically than the lateral one as illustrated in Figure 4.4 and plotted in Figure 4.5. This has been explained by the k-space representation of the 2D PIO filter in Section 2.7. Correspondingly, Figure 4.11 illustrates the trend of the measured mainlobe to grating lobe ratio (MGR) with sweeping β. Figure 4.6 shows the PSF for β =0.1 as an example where the grating lobes are suppressed to give a better image quality.

Cyst phantom

We used a simulated, 2D uniform phantom with a spherical cyst in the middle to illustrate the contrast measurement of the imaging systems. Specifically, the contrast

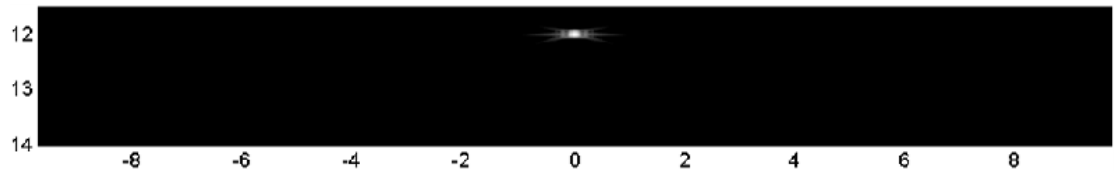

(a) lateral pitch: 0.5 λ

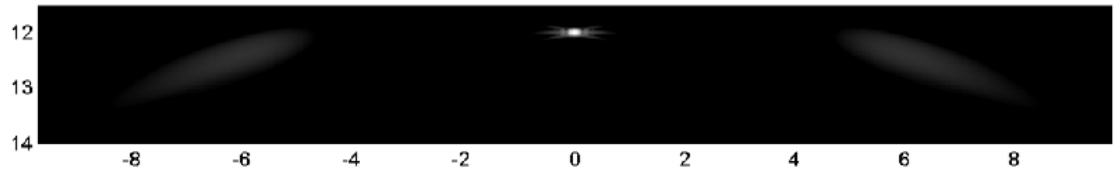

(b) lateral pitch: 2 λ

Figure 4.1: Grayscale images (60 dB) of the PSFs, the vertical coordinate is axial direction, the horizontal coordinate is lateral direction and both are in mm.

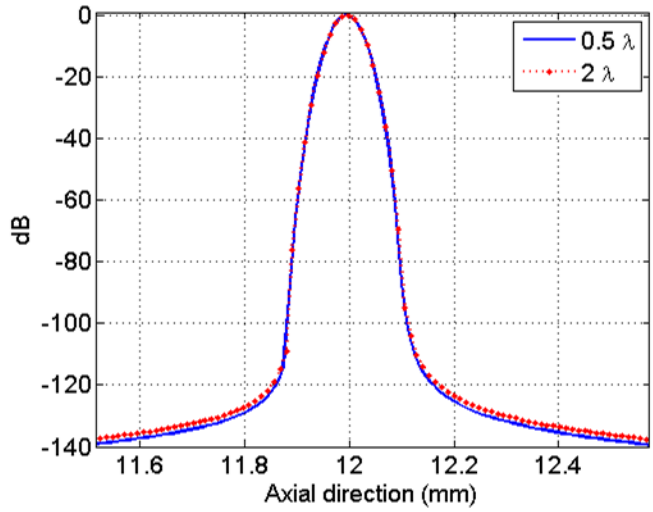

(a) Axial PSFs

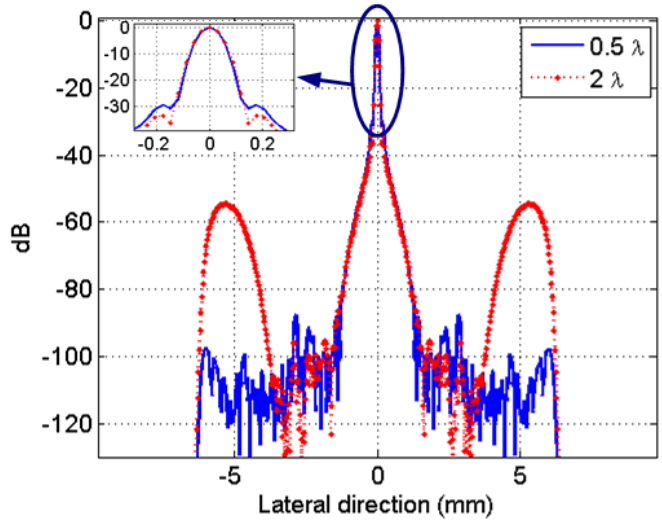

(b) Lateral PSFs

Figure 4.2: Comparison of Axial and Lateral PSFs for 0.5λ pitch and 2λ pitch.

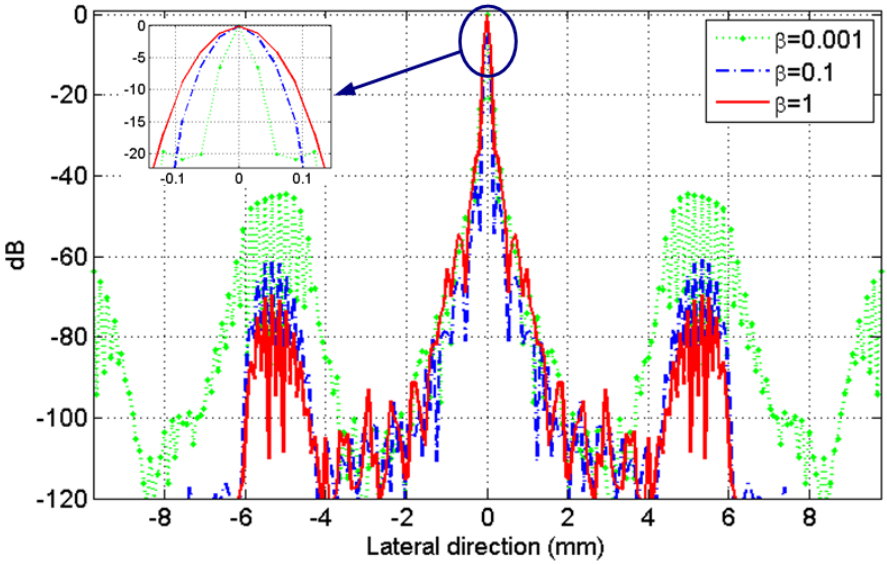

Figure 4.3: Lateral PSFs, filtered by 2D PIO filter with regularization parameter $\beta =$ 0.001, 0.1 and 1.

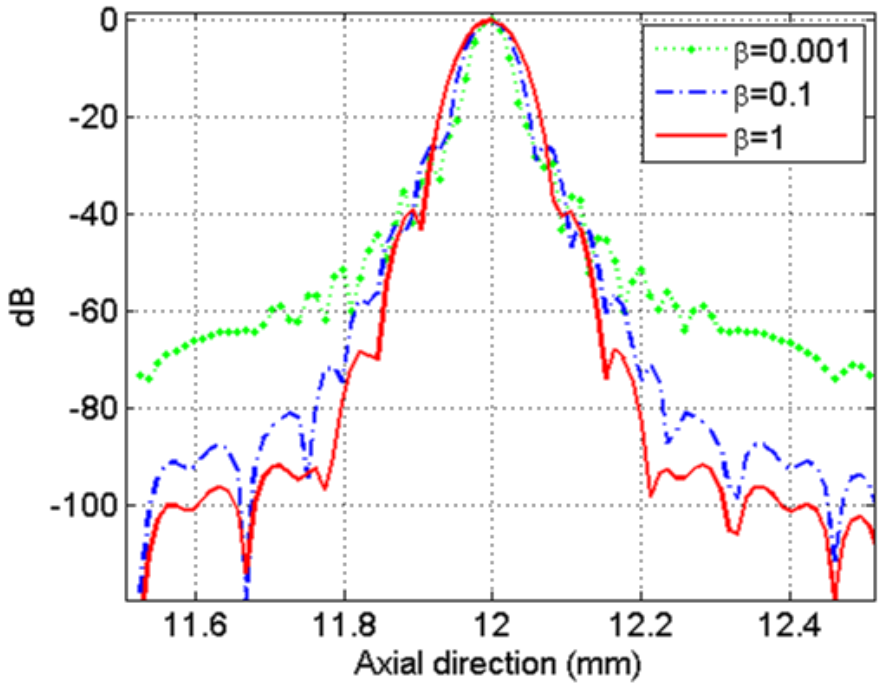

Figure 4.4: Axial PSFs, filtered by 2D PIO filter with regularization parameter $\beta =$ 0.001, 0.1 and 1.

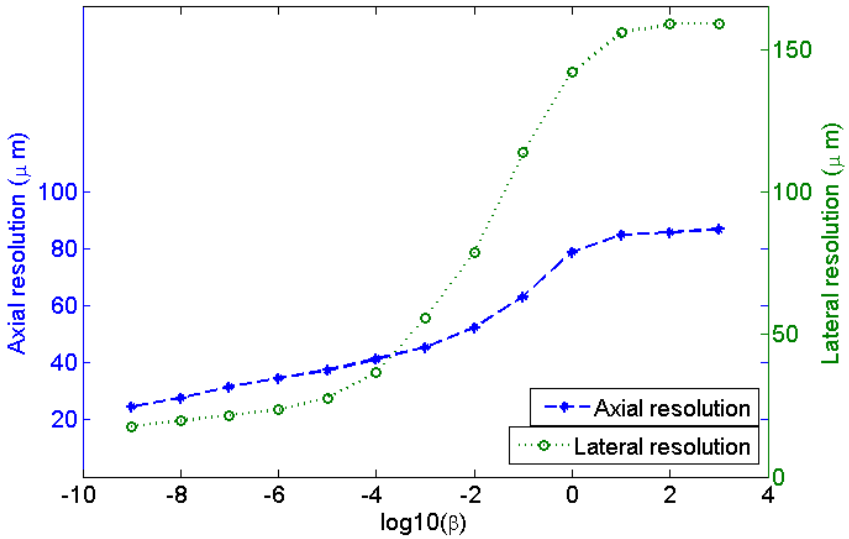

Figure 4.5: Spatial resolutions of results filtered by 2D PIO filter with sweeping regularization parameter β.

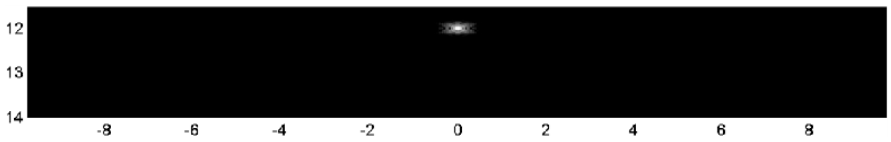

Figure 4.6: 60 dB gray scale representation of the PSF filtered by 2D PIO filter with β=0.1.

ratio computed from the cyst phantom gives a measurement of the loss of SNR due to the grating lobe artifact. On the other hand, we will use the same quantified measurement to illustrate the improvement by using the 2D PIO filter, or even recover most of contrast loss due to the artifact. The 4 x 20 mm^2 phantom is centered at the focus [0 0 12] mm with a cyst of radius 1 mm. The phantom is set to be long enough in lateral direction to include the artifacts of the 1^{st}-order grating lobe due to coarse sampling.

Figure 4.7 shows the 50 dB grayscale images of the 3.8 x 8.4 mm^2 region in the cyst phantom from the imaging systems with Nyquist-sampled aperture: 0.5λ (a) and coarsely-sampled aperture: 2λ (b). We computed the contrast ratio (CR) Equation 3.4 for a circular region of radius 0.9 mm outside/inside of the cyst. The region outside of the cyst is centered at [3.4 0 12] mm and the region inside is centered at the focus [0 0 12] mm. The contrast ratio of Figure 4.7(a) and Figure 4.7(b) are respectively 28.8 dB and 20.4 dB as listed in Table 4.2.1. Consequently, a 6.4 dB loss of contrast is due to the coarse sampling artifact.

We then obtained results from the regularized 2D PIO filter as illustrated in Figure 4.8. The 50 dB grayscale images are generated with β values of 0.01, 0.1, 0.3, 1 and 10, and the corresponding CRs are 22.7 dB, 26.9 dB, 28.8 dB, 30 dB and 29.2 dB as shown in Table 4.2.1. By comparing the images in Figure 4.8, we see that the contrast is improved with increased β values as shown from Figure 4.8(a) to Figure 4.8(d). This is due to increased MGR with respect to increased β as shown in Figure 4.11. At the same time, the spatial resolutions of the images, especially the lateral resolution, are increasing in Figure 4.8 (a)-(d), which matches the trend of changes in spatial resolutions from the study of PSFs in Figure 4.5. The change in contrast and lateral resolution can be better interpreted in Figure 4.9 where the noise level inside of the cyst increased with smaller β values while the edge of the cyst along the lateral direction is becoming sharper at the same time, corresponding to better lateral resolution. At the same time, the spatial resolution along the axial direction remains the same with different β values as shown by the cyst edges along the axial direction in Figure 4.10. Furthermore, when the lateral resolution becomes bad enough to blur the contrast edge, the contrast decreases even with better lateral sidelobe level reduction as shown in Figure 4.8(e). Therefore, a good compromise for the regularization process will produce the best image quality. A β value of 0.3 (Figure 4.8(c)) is chosen to recover all the 6.4 dB loss in the contrast

due to the coarse sampling artifact as in Figure 4.7(a) and Figure 4.7(b). In the mean time, the spatial resolutions are kept about the same as the original system as plotted in Figure 4.5. If the contrast is preferred, a larger β value (*e.g.* 1) can be used to achieve contrast ratio of 30 dB; likewise, if the spatial resolutions are favored, a smaller β value (*e.g.* 0.01) can be used to have about 50 μm axial resolution and 80 μm lateral resolution. These decisions are depended on the specific application requirements or practical considerations.

Finally, we draw the connection of MGR with the contrast ratio measured from the cyst phantom. As plotted in Figure 4.11, the contrast ratio (the dotted line with circle) approximately increases with MGR (the dashed line with cross) in a logarithm scale of the regularization parameter β. As stated above, this is because the lateral side lobe level of the PSF is due to the grating lobe of coarse sampling, contributing main source of noise. The contrast ratio reaches the maximum as the lateral side lobe level reduced and at the same time, the lateral resolution becomes larger to reduce the contrast. The most important message from this relationship is that we are able to predict the contrast from MGR instead of obtaining it from the speckle-generating phantom which requires intensive computational resources.

Verification of the 2D PIO Filter in Spatial-Temporal Form

We have shown the improved imaging performance by using the 2D PIO filter in k-space for a coarsely-sampled HFUS array; correspondingly, the finely-sampled one was simulated to be the reference for comparison [97]. In this section, the simulation results are presented to show similarly improved imaging performance by using the 2D PIO filter in spatial-temporal form. For the purpose of comparison, we studied the same 25 MHz HFUS linear array prototype proposed in [97], constructed using the Matlab-based simulation tool: Field II [43]. All the parameters are also set to be the same as in [97]: the speed of sound was set to be 1480 m/s; a Gaussian impulse response model was assumed for the array elements and an impulse-like signal was used as excitation;

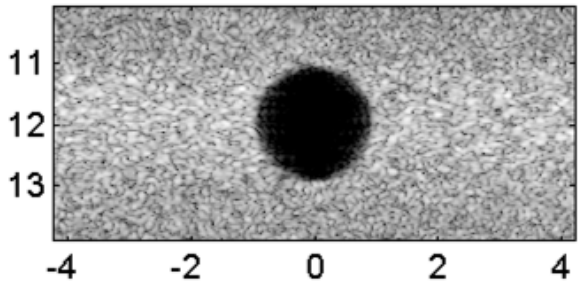

(a) lateral pitch: 0.5 λ

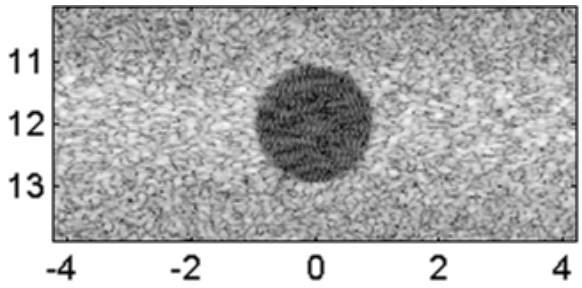

(b) lateral pitch: 2 λ

Figure 4.7: Grayscale images (50 dB) obtained from the cyst phantom, the vertical coordinate is axial direction, the horizontal coordinate is lateral direction and both are in mm; (a) conventional beamforming using a Nyquist sampled array; (b) conventional beamforming using a coarsely sampled array (2λ).

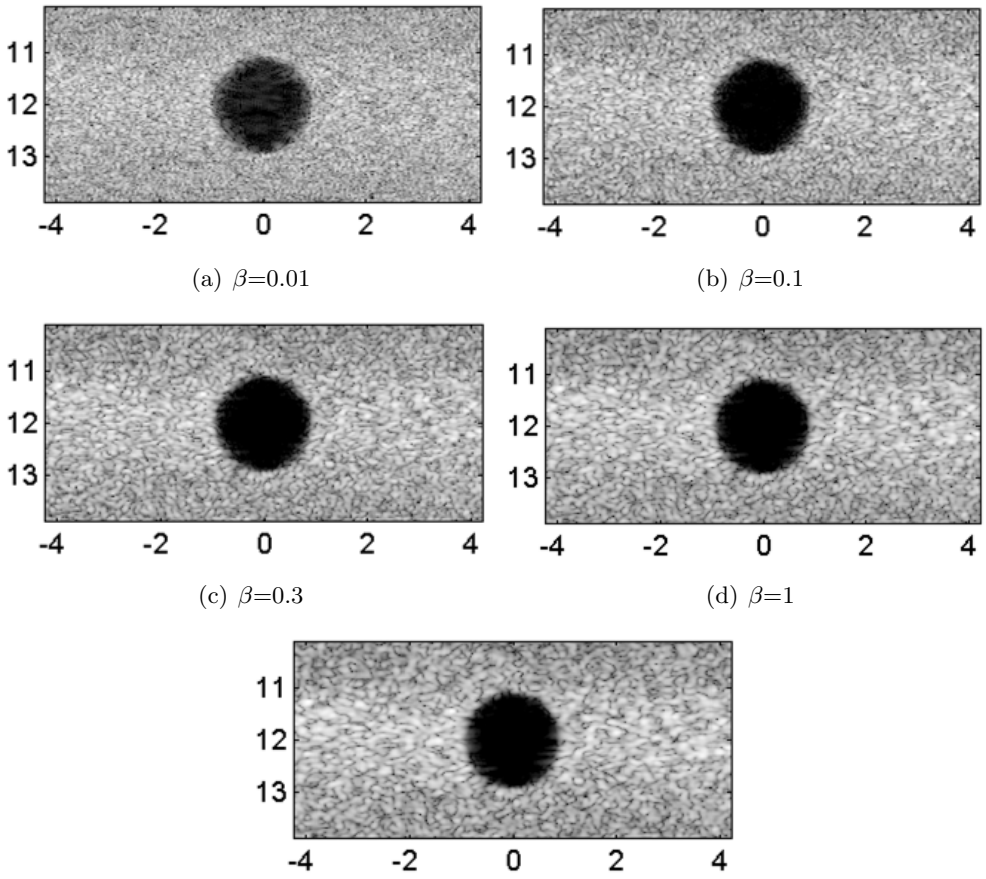

(a) β=0.01

(b) β=0.1

(c) β=0.3

(d) β=1

(e) β=10

Figure 4.8: Grayscale images (50 dB) obtained from the cyst phantom, filtered by the regularized 2D PIO filter, the vertical coordinate is axial direction, the horizontal coordinate is lateral direction and both are in mm. (a) $\beta = 0.01$, (b) $\beta = 0.1$, (c) β= 0.3, (d) $\beta = 1$, and (e) $\beta = 10$.

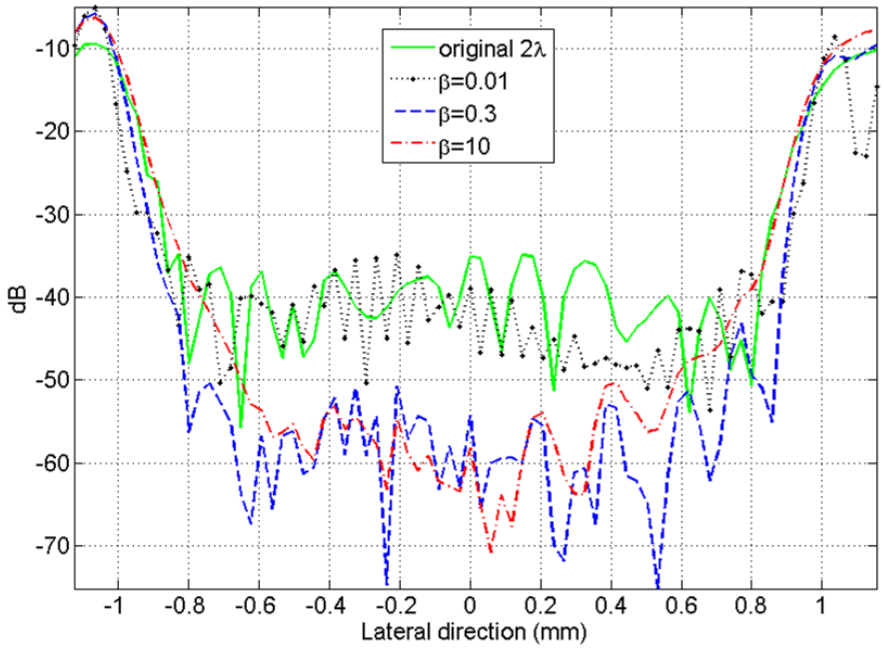

Figure 4.9: Lateral line plots through cyst center at z = 12 mm for different values of β. The loss of lateral resolution can be clearly seen for $\beta = 10$ while the loss of contrast is clear for $\beta = 0.01$.

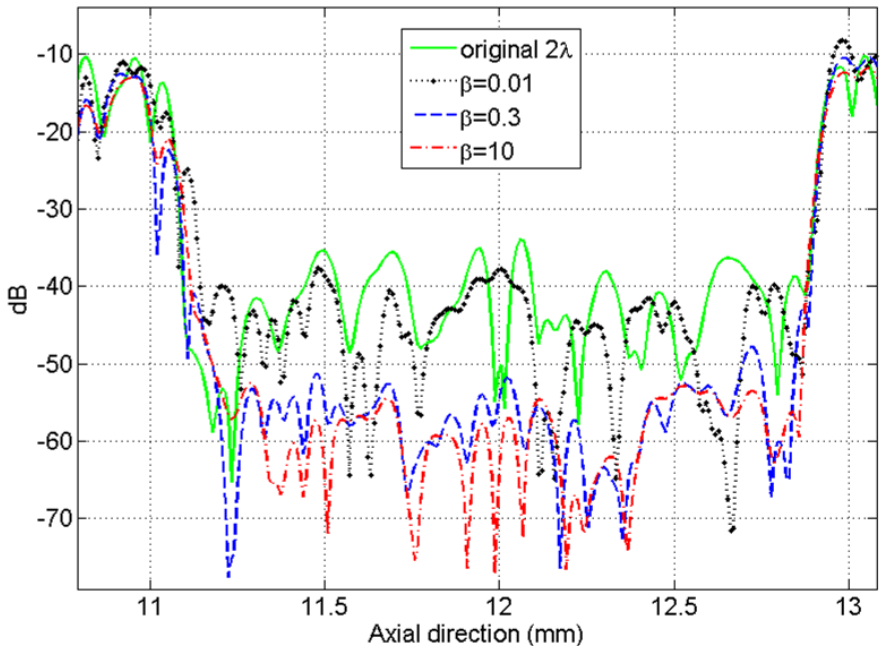

Figure 4.10: Axial line plots through cyst center at x = 0 mm for different values of β. One can observe a minimal loss in resolution for $\beta = 10$ in the axial direction while the loss of contrast is clear for $\beta = 0.01$.

0.5λ	**2λ**	**2D PIO filter, β**					
		0.001	**0.01**	**0.1**	**0.3**	**1**	**10**
28.8	20.4	18.1	22.7	26.9	28.8	30	29.2

Table 4.1: Contrast ratio of the images from the cyst phantom.

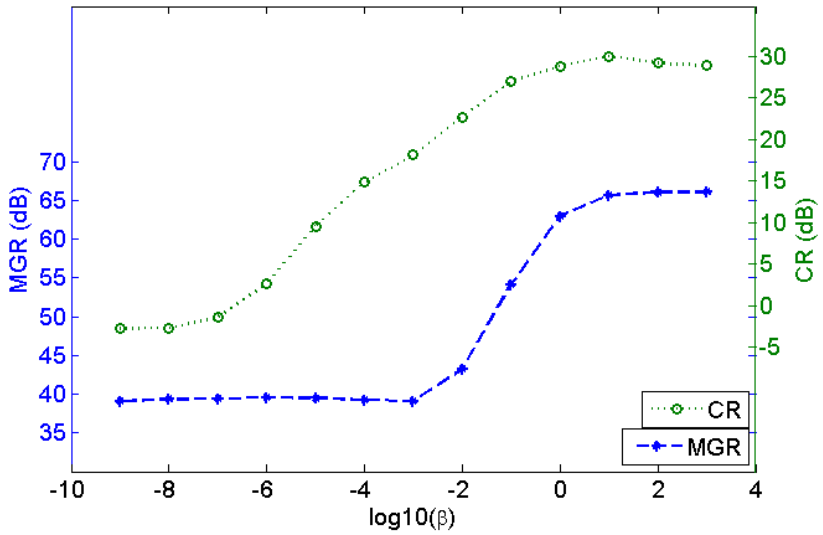

Figure 4.11: Contrast ratio vs. the regularization parameter β in logarithm scale (the dotted line with circle). MGR vs. the regularization parameter β in logarithm scale (the dashed line with cross).

conventional delay-and-sum beamforming was used before applying this algorithm; the array prototype is specified with the following parameters: center frequency: $f_0 = 25$ MHz; fractional bandwidth: 60%; active aperture size: 6 mm; lateral focal distance: 12 mm; elevation height: 2.5 mm; elevation focal distance: 15 mm; lateral pitch: 0.5 λ ($\approx$ 30 μm), 2 λ ($\approx$ 118 μm).

Two 25 MHz linear arrays were simulated, respectively with $\lambda/2$ and with 2λ element spacing. An example of the 2D kernel with size of 266.4 μm $\times$ 651.2 μm is obtained from the ROS of the 2D PIO filter with β=0.3. The size of the 2D kernel is only 0.03% of the size of the filter in k-space. The algorithm was verified in imaging the same 2D uniform speckle-generating phantom (average 25 scatterers per resolution cell) with a 1-mm radius spherical cyst at the center of a region with axial and lateral extent of 4 and 20 mm, respectively. The 50 dB grayscale images of the 3.8 $\times$ 8.4 mm^2 ROI are shown in Figure 4.12: (a) using the finely sampled array, (b) using the coarsely sampled array, (c) applying the post-beamforming 2D PIO filter (with β=0.3) in k-space to the RF data obtained using the coarsely sampled array, and (d) applying the 2D kernel of the filter in spatial-temporal domain. The contrast ratio (CR) was measured as 28.8, 20.4, 28.8 and 28.2 dB for the images in Figure 4.12 (a), (b), (c) and (d), respectively. The contrast ratio obtained from the results using the filter kernel in spatia-temproral domain is only 2% less than the results filtered in k-space. In addition, the spatial resolutions were 61.2, 62.2, 71 and 71 μm in axial direction and 111.8 120, 128 and 131 μm in lateral direction, respectively. The simulation results verify that the 2D spatial filter with finite ROS can achieve the same level of restoration in CR while maintaining the same level of spatial resolution achieved by the full k-space filtering approach. The size of the 2D kernel is only 0.03% of the size of original filter, which significantly reduces the computational load, allowing for real-time implementation especially with modern hardware platforms optimized for digital filtering.

4.2.2 35 MHz Small-Footprint HFUS Array Prototype

In 2006, the Ultrasonic Transducer Resource Center at University of Southern California [25] developed a 35 MHz linear array using 2-2 composite for medical imaging

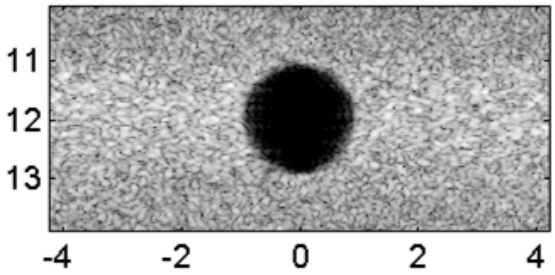

(a) Lateral pitch: 0.5 λ [97]

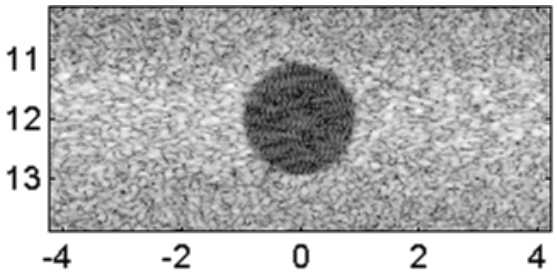

(b) Lateral pitch: 2 λ [97]

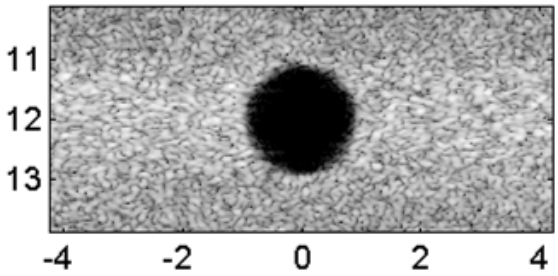

(c) Filtered in k-space

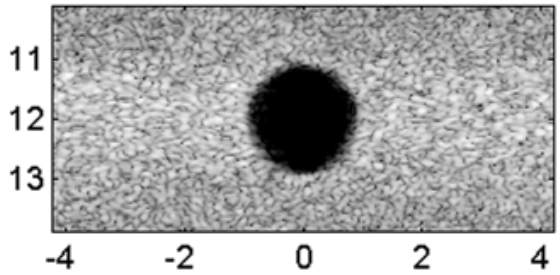

(d) Filtered in spatial domain

Figure 4.12: Grayscale images (50 dB) obtained from the cyst phantom, the vertical coordinate is axial direction, the horizontal coordinate is lateral direction and both are in mm. (a) Conventional beamforming using a Nyquist sampled array; (b) conventional beamforming using a coarsely sampled array (2λ); (c) full k-space with $\beta = 0.3$; and (d) 2-D kernel with $\beta = 0.3$.

applications. We simulate an HFUS prototype extracted from this linear array to further illustrate the proposed algorithm for higher frequency. The only modification we made for the array specifications is the dimension in elevation direction. We modified it so that we can have smooth imaging performance for $f_{\#} = 2$, consequently we would be able to compare the imaging performance obtained from the proposed algorithm at different frequencies. The specifications of the designed prototype are listed as follows:

- center frequency: $f_0 = 35$ MHz;
- fractional bandwidth: FBW = 55%;
- active aperture size: 3.2 mm;
- lateral focal distance: 6.4 mm;
- elevation height: 1.5 mm;
- elevation focal distance : 7.5 mm
- lateral pitch: 0.5 λ ($\approx$ 21 μm), 1.2 λ($\approx$ 51 μm), 2 λ ($\approx$ 85 μm);

where the elevation height and elevation focus are different with the design described in [25]. The 1.2 λ lateral pitch is the actual array lateral element-to-element spacing specified in [25]. We also simulated the 0.5 λ case as a golden reference and the 2λ case for applying the proposed algorithm just as in the case of the 25 MHz prototype. Given that the PSF characteristics are quite similar here as for the 25 MHz prototype, we will not repeat the details of this part; instead, we only illustrate the key elements: MGR in Figure 4.14 and spatial resolutions in Figure 4.15.

We also simulated a 4 x 12 mm^2 speckle-generating cyst phantom centered at the focus [0 0 6.4] mm with a cyst of radius 1 mm to illustrate the contrast measurement. Again, the lateral extension of the cyst phantom is chosen to include the 1^{st}-order grating lobe due to coarse sampling. Figure 4.13 shows the 50 dB grayscale images of the 3.8 x 12 mm^2 region in the cyst phantom from the imaging systems with lateral pitch of : 0.5λ (a), 1.2λ (b), 2λ (c) and finally the filtered results from the 2λ lateral-sampled aperture using 2D PIO filtering algorithm with regularization parameter $\beta = 0.3$ (d). The 0.5λ image provides the image quality we would like to obtain with contrast ratio of 30.4 dB

as listed in Table 4.2. The 1.2λ case shows reasonable image quality with contrast ratio of 25.8 dB; however, it is important to note that this result is based on simulation which does not include the potential cross-talk degradation due to fabrication limitation for small element dimension, such as 51 μm in this case. Naturally, the 2λ case provides worse imaging quality with contrast ratio of 17.1 dB which is not allowable for medical imaging applications.

Then we applied the propose algorithm to the 2λ result with regularization parameter, β, swept from 0.001 to 10 as shown in Table 4.2. Coincidentally, the result with $\beta = 0.3$ provides the contrast we would like to achieve: 30.4 dB from the 0.5λ case. Therefore, we are able to recover the contrast loss due to coarse sampling by using the 2D PIO filtering algorithm, consequently, 2λ lateral pitch can be used in this case to obtain similar image quality as in the 0.5λ case. In this way, 85 μm element width can be used for 35 MHz arrays instead of pushing to 51 μm or 21 μm.

In addition to recovering the contrast loss, the connection of MGR with the contrast ratio measured from the cyst phantom can be similarly draw. As plotted in Figure 4.14, the contrast ratio (the dotted line with circle) approximately increases with MGR (the dashed line with cross) in a logarithm scale of regularization parameter β. We would like to use this drawing to emphasize the relationship of predicting the contrast with MGR obtained from Figure 4.11.

4.3 Quality-Assurance Phantom Results

Further experiments using quality-assurance phantoms were conducted to verify the performance of the 2D PIO filter in a more realistic environment. The Ultrasonix RP system [95] with L14-5/38 linear array probe was used. The imaging target was the General Purpose Multi-Tissue Ultrasound Phantom (CIRS Model 040) [98]. We used 2-cycle 10 MHz excitation for the purpose of emphasizing the information in the higher-frequency band and the speed of sound was set to be 1540 m/s.

The imaging system was focused at the cystic target and the high contrast target at a depth of 4 cm with a diameter of 4 mm. The attenuation coefficient for the surrounding

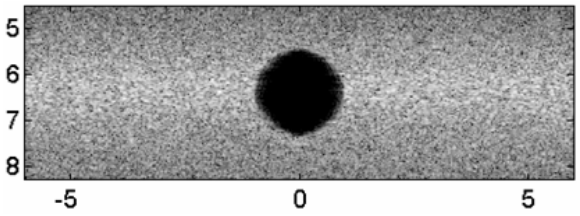

(a) lateral pitch: 0.5 λ

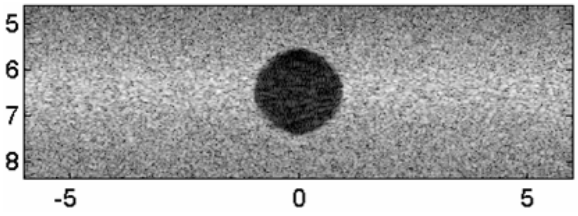

(b) lateral pitch: 1.2 λ

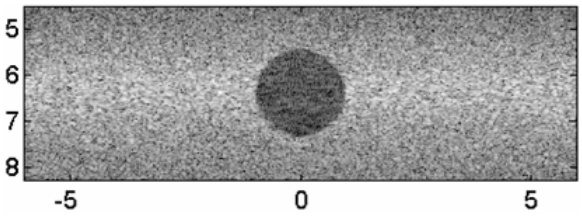

(c) lateral pitch: 2 λ

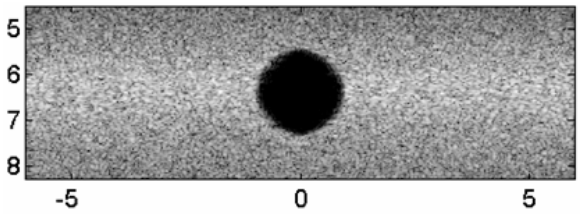

(d) β=0.3, lateral pitch: 2 λ

Figure 4.13: Grayscale images (50 dB) obtained from the cyst phantom, the vertical coordinate is axial direction, the horizontal coordinate is lateral direction and both are in mm. (a) Conventional beamforming using a Nyquist sampled array; (b) conventional beamforming using a coarsely sampled array (1.2λ); (c) conventional beamforming using a coarsely sampled array (2λ); (d) full k-space with $\beta = 0.3$.

0.5λ	**1.2λ**	**2λ**	**2D PIO filter, β**					
			0.001	**0.01**	**0.1**	**0.3**	**1**	**10**
30.4	25.8	17.1	17.2	22	28.3	30.4	32	32.6

Table 4.2: Contrast ratio of the images from the cyst phantom.

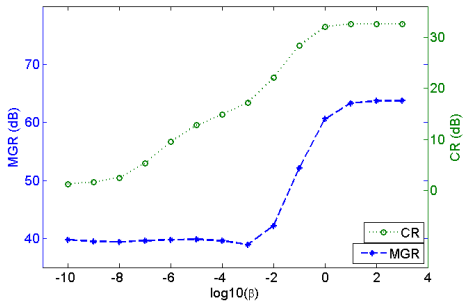

Figure 4.14: Contrast ratio vs. the regularization parameter β in logarithm scale (the dotted line with circle). MGR vs. the regularization parameter β in logarithm scale (the dashed line with cross).

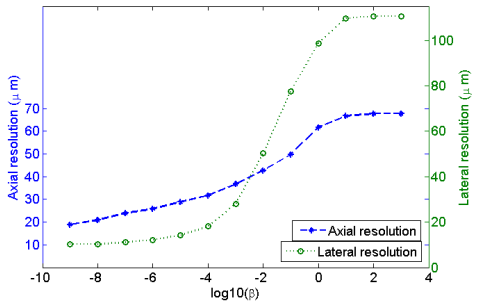

Figure 4.15: Spatial resolutions of results filtered by 2D PIO filter with sweeping regularization parameter β.

material is 0.5 dB/cm/MHz and the attenuation coefficient inside of the cyst is less than 0.07 dB/cm/MHz. The 50 dB grayscale images are shown in Figure 4.16: run 1, 10 $\times$ 30 mm^2 ROI, (a) applying a post-beamforming band-pass filter (BPF), (b) applying the post-beamforming 2D PIO filter with β=1; run 2, 13.5 $\times$ 20 mm^2 ROI, (c) applying the BPF, (d) applying the 2D PIO filter with β=1. The contrast ratio was measured as 12.4 and 20.8 dB for the images in Figure 4.7 (a) and (b), respectively. In addition, the speckle correlation cell sizes [79] were measured as 219.9 and 224.2 μm in axial direction and 634.8 and 813.1 μm in lateral direction, respectively. The 8.4 dB contrast improvement in this experiment verifies that the 2D PIO filter can also achieve good performance for contrast restoration in experimental environment. Furthermore, the experimental results also verify the well-behaved regularization process which has been proved by simulation results in [97]. As shown in Figure 4.18, the CR values have a well-behaved changing pattern with respect to $log10\beta$: an approximate sigmoid. This suggests that the user will be able to directly determine the level of regularization necessary to achieve the desired levels of performance. This can be implemented in much the same way as the TGC is implemented on current scanners. Similar experiments for cystic target at a depth of 2 cm with a diameter of 2 mm has also been done and the images are shown in Figure 4.17 with CR measurements of 14.9 and 22.6 dB for Figure 4.17 (a) and (b) respectively.

4.4 *In Vitro* and *In Vivo* Results

4.4.1 Porcine Eye *In Vitro*

Ophthalmology is an important application for high frequency ultrasound imaging. For example in ER, direct visualization of intraocular structures is difficult or impossible when the eye lids are swollen shut after injury. Lens opacification and hyphema can also block the posterior view of the chamber. The ability of ultrasound to evaluate the eye and the adjacent structures in a rapid and noninvasive manner is of tremendous value in busy ER [99]. An interesting region in the ocular anatomy is the optic nerve head region underneath the lens area as shown in Figure 4.19(a). The optic nerve attaches

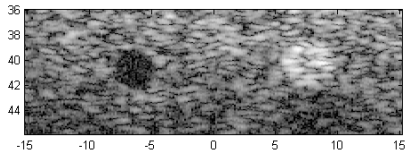

(a) Run 1, BPF

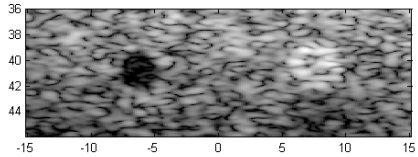

(b) Run 1, 2D PIO filter

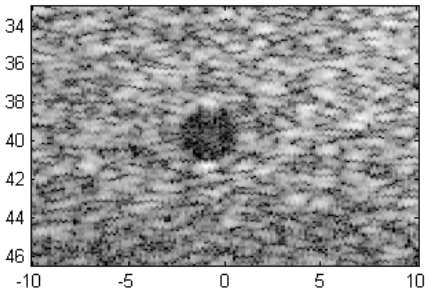

(c) Run 2, BPF

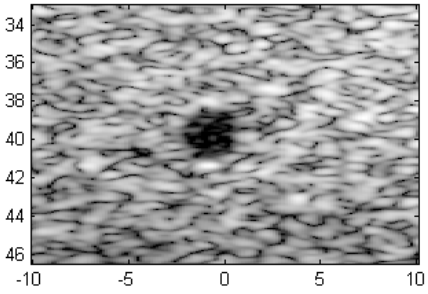

(d) Run 2, 2D PIO filter

Figure 4.16: Grayscale images (50 dB) obtained from the cystic target and high contrast target at depth of 4 cm in CIRS Model 040 quality assurance phantom, the vertical coordinate is axial direction, the horizontal coordinate is lateral direction and both are in mm.

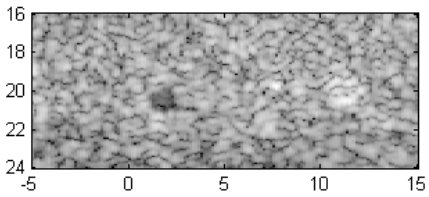

(a) Filtered by BPF

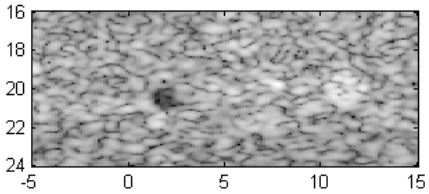

(b) Filtered by 2D PIO filter, β=1

Figure 4.17: Grayscale images (50 dB) obtained from the cystic target and high contrast target at depth of 2 cm in CIRS Model 040 quality assurance phantom, the vertical coordinate is axial direction, the horizontal coordinate is lateral direction and both are in mm.

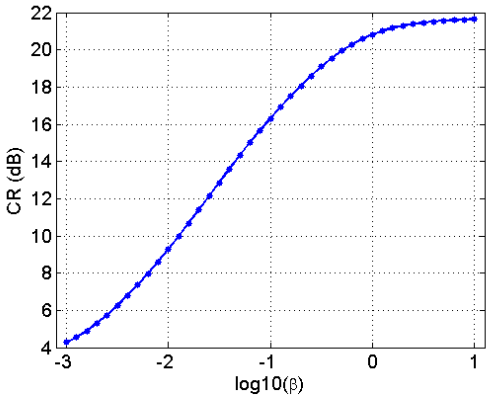

Figure 4.18: CR vs regularization parameter β in logarithm scale.

to the globe posteriorly and is wrapped in a sheath that contains fluid. The optic nerve sheath is contiguous with the dura mater and has a trabeculated arachnoid space through which cerebrospinal fluid slowly percolates. This area is generally echolucent with ultrasound. The relationship between the optic nerve sheath diameter (ONSD) and intracranial pressure (ICP) has been well established [99]. Evaluation of the optic nerve sheath diameter (ONSD) can detect elevated intracranial pressure (EICP). The evaluation of the optic nerve sheath diameter using ultrasound imaging is a simple non-invasive procedure, which is a useful tool in the assessment of elevated intracranial pressure in Pathology. Therefore we are interested in enhancing the contrast of the optic nerve sheath region using the 2D PIO filtering algorithm. In this section, we present experimental results on imaging porcine eye tissue *in vitro* as an illustration of enhancing the contrast of the optic nerve sheath region.

Figure 4.19(b) and Figure 4.19(c) show the results filtered by the 2D PIO filter with different values of regularization parameter: β. With $\beta = 1$ as shown in Figure 4.19(c), the filtering algorithm obtains a good contrast ratio value of 18.5 dB for the optic nerve sheath region, and the contrast improvement compared to the result without applying the filter (15.3 dB) is 3.2 dB. More importantly, with a relatively smaller value of β, for example 0.01, the contrast ratio measurement is less: 17.3 dB but with fine resolution as shown in Figure 4.19(b). In this case, we see a very good definition of the contour of the optic nerve sheath region, and a clear definition of the contour of the sheath region is essential for making correct measurement of the ONSD, leading to a good detection of the EICP.

4.4.2 Carotid Artery *In Vivo*

In this section, we present experimental results from imaging human carotid artery *in vivo*. The carotid arteries are located on each side of the neck and carry blood from the heart to the brain. Ultrasound imaging on carotid arteries can be used for detecting the blockage or narrowing of the carotid arteries (conditions that substantially increase the risk of stroke), locating a hematoma, detecting dissection of the carotid artery or verifying the position of a metal stent placed to maintain carotid blood flow.

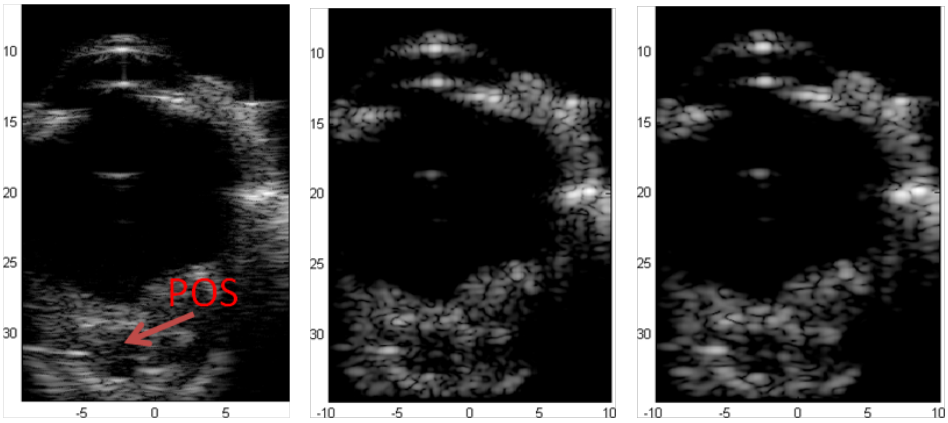

(a) Original (b) β=0.01 (c) β=1

Figure 4.19: Grayscale images (60 dB) of the *in vitro* porcine eye, the vertical coordinate is axial direction, the horizontal coordinate is lateral direction and both are in mm.

We used the Ultrasonix RP system [95] with L14-5/38 linear array probe. A simulated model for forward propagation was constructed based on the L14-5/38 linear array probe profile with the speed of sound set to be 1540 m/s as in soft tissue. The 2D filter coefficients were computed from the model using the 2D PIO filtering algorithm. An illustration of the 2D pseudoinverse filter representation is shown in Figure 4.20 with the regularization parameter set to be 1.

As shown in Figure 4.21, the center of the right carotid artery is at the depth of about 15 mm and its diameter is 6.5 mm. The probe was tilled slightly to reduce specular reflections from the artery walls. This may result in more clutter such as grating-lobe artifact from the tissue within the artery. The 50 dB grayscale images of the carotid artery before and after applying the 2D PIO filtering algorithm are shown in Figure 4.21 and Figure 4.22, respectively, both with a size of 27.4 mm $\times$ 38 mm. By comparing the PIO-filtered image with the unfiltered image, one can see a discernible difference in echogenicity from within the carotid. In addition, the speckle in tissue regions is generally well-behaved in the filtered image compared with the unfiltered one.

The contrast ratio (CR) was measured as 15.2 dB and 19 dB for the images in Figure 4.21 and Figure 4.22, respectively. In addition, the speckle correlation cell sizes [79] were measured as 286.6 μm and 284 μm in axial direction and 494.5 μm and 782.3 μm in lateral direction, respectively. Finally, the CR measurements from the *in vivo* results have a smooth changing pattern with respect to $\log_{10}\beta$. Specifically, it has an approximate sigmoidal behavior as shown in Figure 4.23, demonstrating a well-behaved regularization process which is one of the key reasons of the guaranteed robustness. This suggests that the user will be able to directly determine the level of regularization for achieving the desired levels of performance. This can be implemented in much the same way as the TGC is implemented on current scanners. All of these *in vivo* results are consistent with our previously reported results from computer simulations [100] as well as imaging of quality assurance phantoms [101], again verifying the imaging performance of the 2D PIO filtering algorithm such as contrast restoration.

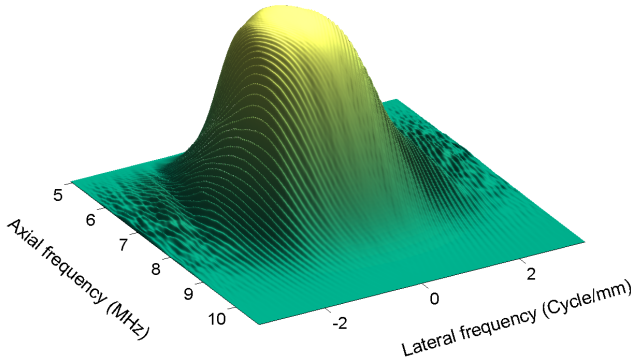

Figure 4.20: The frequency response of the 2D PIO filter in k-space, applied to the carotid artery data with the regularization parameter β=1.

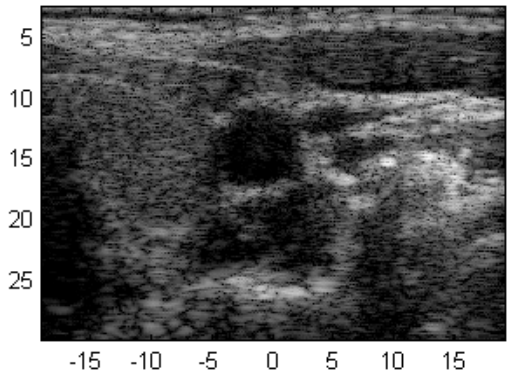

Figure 4.21: The grayscale image (50 dB) of the right carotid artery, the vertical coordinate is axial direction, the horizontal coordinate is lateral direction and both are in mm.

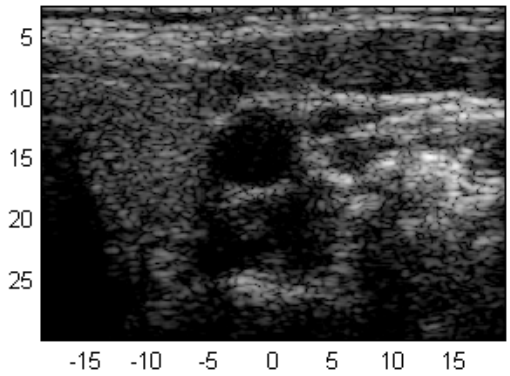

Figure 4.22: The grayscale image (50 dB) of the right carotid artery, filtered by the 2D PIO filter, the vertical coordinate is axial direction, the horizontal coordinate is lateral direction and both are in mm.

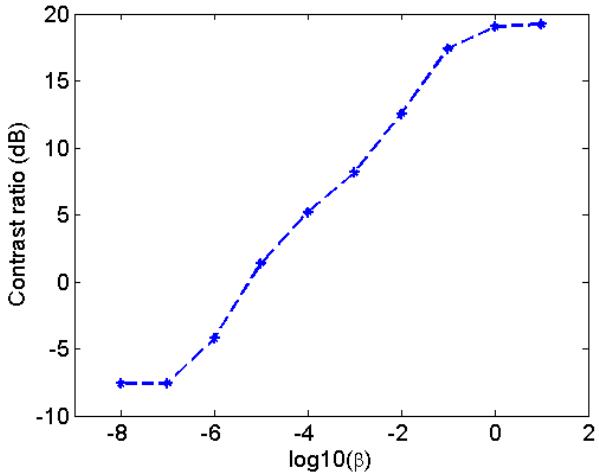

Figure 4.23: Contrast ratio of results filtered by 2D PIO filter with sweeping regularization parameter β.

4.5 Conclusion

We presented using the 2-D postbeamforming filtering algorithm for restoration of contrast resolution in high frequency pulse-echo ultrasonic imaging systems employing coarsely sampled apertures. This was demonstrated for 2 high-frequency ultrasound arrays operating at 25 and 35 M Hz with fractional bandwidths of 60% and 55%, respectively. The latter array has been described in the recent literature [24] and represents an example of the latest technology in HFUS. The simulation results clearly show that, for a given array sampling geometry, one can design a 2-D PIO with a specific regularization parameter value to restore the contrast ratio to levels achieved by Nyquist-sampled arrays without sacrificing spatial resolution. Measures of spatial and contrast resolution were shown to vary smoothly (approximately as a sigmoid) with the logarithm of the regularization parameter. This validates the the robustness and predictability of this pesudoinverse filtering algorithm. Experiment results on quality-assurance phantom and tissue *in vitro* or *in vivo* also verified the performance of this algorithm on both the contrast enhancement and smooth parameter-controlled regularization. Therefore, the 2-D postbeamforming PIO approach offers the promise of realizing the benefits of high-resolution ultrasonic imaging using coarsely sampled apertures.

Chapter 5

Conclusion and Future Work

5.1 Conclusion

We proposed the use of post-beamforming pseudoinverse filtering algorithms for restoring contrast resolution in pulse-echo medical ultrasound imaging. The regularized 1D post-beamforming pseudoinverse filtering together with coded excitation has been shown to improve the axial resolution of a DMUA prototype by 30% without significant loss in contrast ratio. Gain compensation and accounting for element directivity have been shown to extend the DMUA FOV. A Field II-based simulation model of the concave DMUA has been developed as a tool to assess the imaging performance of DMUA prototypes. This will help in the design of future DMUA prototypes. Wire target array images obtained by beamforming experimental and simulation data show that the array simulations capture the array geometry and bandwidth characteristics. Listed in Section A, these images show that the PSF, the Ix-FOV, and the grating lobe structure are well predicted by the simulation model. The simulation model was then used to evaluate the effect of varying DMUA design parameters (FBW and aperture sampling) on the PSF and the contrast ratio of cyst targets positioned at various locations within the IxFOV. Finally, based on this simulation study in Section A, we have proposed a modified DMUA design that results in significant enhancement in the imaging performance in terms of spatial and contrast resolution as well as expanded IxFOV. Using simple element interconnection schemes in imaging and therapy modes, the modified DMUA can achieve this enhancement while simultaneously maintaining the therapeutic

aperture sampling of the existing DMUA design that has been optimized for therapy. This implies that the improvements in imaging performance of the DMUA will not significantly compromise its predicted therapeutic performance.

Based on the formulation of the 1D pseudoinverse filter, I have derived the 2D post-beamforming filtering algorithm for restoration of lost information due to various artifacts, such as beamforming artifacts due to coarse sampling. The algorithm is based on a discretized receive signal model of the imaging FOV on a Cartesian grid in linear-array imaging. A simple and efficient multiplication operation is derived using the k-space methods in the 2D spatio-temporal frequencies domain, preceded and followed by fast DFT operations. The formulation of the operator was shown to allow a computationally efficient implementation of the filter in k-space using 2-D fast Fourier transform or in the spatial domain using a 2-D impulse response with small ROS. From the k-space representation, we see that this filter is a regularized pseudoinverse operation of the system impulse response. The impulse response of the array imaging system includes information of the transmitted waveform, system aperture and beamforming. With the knowledge of these information, we are able to reconstruct the imaging target to certain degree by this regularized pseudoinverse operation. Measures of spatial and contrast resolution were shown to vary smoothly (approximately as a sigmoid) with the logarithm of the regularization parameter.

The simulation results demonstrate that 2D post-beamforming filtering can be effectively used in recovering the loss in contrast due to beamforming artifacts with minimum loss in spatial resolution. In particular as shown in Section 4, grating-lobe artifacts can be removed by applying a properly designed 2D PIO to the beamformed data acquired using arrays with coarse sampling (element spacing in the range of $1.2 - 2.5\lambda$). In principle, loss in contrast due to even coarser sampling can be restored, but the spatial frequency loss due to increased element directivity becomes excessive for element spacing $> 3\lambda$. The regularization approach described in this paper may not be sufficient for recovering some or all of the nulls that appear in the passband defined by the aperture (see Figure 2.2). It is important to point out, however, the significance of the contrast recovery achieved for element spacing in the range of 2λ demonstrated in this paper. As suggested by the 35-MHz prototype example, the same aperture could be sampled at 2λ (≈ 85 μm) and still achieves the same CR levels as the Nyquist sampling case

(≈ 21 μm) and exceeds the performance of conventional beamforming with the existing prototype sampled at 1.2λ (≈ 51 μm). Given the current state of transducer technology, easing the requirements on array sampling may allow higher fidelity imaging by reducing element cross coupling and/or preserving transducer bandwidth. It is obvious that for various other applications, the upper limit of the reconstruction capability of this filter needs to be respected and specifically studied.

Although this is a 2-dimensional filtering algorithm, the implementation of the filter in k-space is three 1D operations: one 1D multiplication and two 1D DFT operations. Furthermore, we used CUDA programming for GPU parallel computing for the implementation of this filter and the processing time of a typical image is about 0.1 second. This is already very close to real-time implementation, especially for a 2D filter. We believe with more powerful GPUs, the processing time can be quickly further reduced for real-time implementations.

This filtering algorithm can be applied to various applications where artifacts in the 2D space needs to be eliminated or suppressed and special filters are needed to be designed for special characteristics of the systems. In this dissertation, we applied the filter into two applications: high-frequency ultrasound imaging and image guidance for DMUA system. We have shown that this filter can recover either lost contrast or resolution in different scenarios, or achieve a good combination of the two. This capability of this filter is achieved by the regularization of the filter, changing the filter response accordingly such as the bandwidth or outside-of-main-band noise level. From this point, we see that an adaptive modulation of the filter response may be a more powerful extension of the filter, such as multi-parameter regularization.

5.2 Future Work

5.2.1 Multi-parameter regularization

Our preliminary data suggest that the single-parameter regularization approach effectively controls the lateral behavior of the resulting PSF to compensate for the effects of the grating lobes. It would be quite useful, however, to develop a multi-parameter regularization approach that allows separate (ideally independent) control of the axial and lateral resolutions. While we do not expect these two performance parameters can

be controlled completely independently, it is interesting to investigate the feasibility of using, for example, two parameters to control the axial and lateral response of the 2D PIO separately.

5.2.2 Application to phased-array imaging

The imaging system model shown in this paper applies to linear array imaging, which is useful given the wide use of this imaging mode in ultrasound. However, extending this approach to phased array imaging may be of significant value in high frequency ultrasound, e.g. forward-looking catheter arrays in intravascular applications. In addition to the obvious formulation of the problem in the $r \sin \theta$ coordinate system, one has to account for the spatially-varying nature of the array PSF with the steering angle. This approach is currently being investigated.

5.2.3 Combined with Coded Waveform Design

Coded excitation combined with this 2D pseudoinverse filter can easily lead to a setup for fast frame rate imaging. The 2D pseudoinverse filter can act as a de-coupling filter for the coded waveforms, and consequently we can achieve one frame of data in one transmit. Also, we could beamform the aperture for a wide beam with multiple codes, and one frame of data can be accomplished with a few transmissions. In this way, the frame rate can be increased dramatically and this can be used for various applications, such as 3D real-time ultrasound echo-cardiology.

5.2.4 Quantitative Multi-Dimensional Vascular imaging

Vascular imaging is gaining increased attention not only as a means of detection of cardiovascular diseases, but also for the evaluation of response to new antiatherosclerotic therapies [102]. Recently, there has been increased interest in imaging flow in conjunction with computational fluid dynamic (CFD) modeling the evaluation of large artery hemodynamics [103–105]. In this context, modeling fluid-solid interfaces has been defined as a challenging area in vascular mechanics [105]. Imaging methods capable of capturing both perivascular (and wall) tissue motion and deformations, together with fluid flow may be the key component in addressing this challenge. 2-dimensional speckle

tracking with high frame rate M2D may be a good approach for this challenge [106]. We have shown in Section B that this approach obtains 2D displacements fields and strain/sheer strain fields for simultaneous tracking of tissue motion in the vicinity of arteries and blood flow inside. Furthermore, vascular structure is always accompanied by various imaging artifacts such as reverberation from the vessel wall, and these artifacts are prominent considering the low signal to noise ratio of the blood signal inside the vessel. Therefore, eliminating or suppressing the artifacts from the tissue/wall to the inside of the vessel for a better reconstruction of the vascular structure is an important pre-condition for any tracking algorithm.

References

[1] Y. Wan and Emad S. Ebbini. Imaging with concave large-aperture therapeutic ultrasound arrays using conventional synthetic-aperture beamforming. *IEEE Trans. Ultrason., Ferroelect., Freq. Contr.*, 55(8):1075–1718, August 2008.

[2] F. S. Foster, C. J. Pavlin, K. A. Harasiewicz, D. A. Christopher, and D. H. Turnbull. Advances in ultrasound biomicroscopy. *Ultrasound in Med. & Biol.*, 26(1):1–27, January 2000.

[3] John J. Wild and John M. Reid. Application of echo-ranging techniques to the determination of structure of biological tissues. *Science*, 115:226–230, 1952.

[4] J.M. Reid and J.J. Wild. Ultrasonic ranging for cancer diagnosis. *Electronics*, 25(5):136–138, May 1952.

[5] J.J. Wild and J.M. Reid. Application of echo-ranging technique to the determination of the structure of biological tissues. *Cancer Res*, 14(2):277–283, February 1954.

[6] National Cancer Institute.

[7] J. Ophir, I. Cespedes, H. Pnekanti, M. Yazdi, and X. Li. Elastography: a quantitative imaging methods for measuring the elasticity of biological tissue. *Ultrasonic Imaging*, 13(1):111 – 134, 1991.

[8] D.H. Simpson, Chien Ting Chin, and P.N. Burns. pulse inversion doppler: a new method for detecting nonlinear echoes from microbubble contrast agent. *IEEE Trans. Ultrason., Ferroelect., Freq. Contr.*, 46:372–382, July 1999.

[9] Dalong Liu and Emad S. Ebbini. Real-Time 2-D Temperature Imaging Using Ultrasound. *IEEE TRANSACTIONS ON BIOMEDICAL ENGINEERING*, 57(1):12–16, JAN 2010.

[10] K. Kato and T. Izumi. A new ultrasonic flowmeter that can detect flow direction. *Jpn. Med. Ultrasonics*, 5(5):28–30, May 1966.

[11] F.D. McLeod. A directional doppler flowmeter. In *7th Int Conf. Med. Biol. Eng.*, page 213, 1967.

[12] A. Macovski. Ultrasonic imaging using arrays. *Proc IEEE*, 67:194–195, 1979.

[13] P. D. Corl, G. S. Kino, C. S. DeSilets, P. M. Grant, and A. F. Metherell. A digital synthetic focus acoustic imaging system. *Acoustic Imaging*, 8:39–53, 1980.

[14] K. Thomenius. Evolution of ultrasound beamformers. In *IEEE Ultrason. Symp.*, pages 1615–1622, 1996.

[15] J. R. Lindner. Microbubbles in medical imaging: current applications and future directions. *Nature Reviews Drug Discovery*, 3:527–533, 2004.

[16] Aixplorer ultrasound system.

[17] P. Phukpattaranont and E. S. Ebbini. Post-beamforming second-order volterra filter for pulse-echo ultrasonic imaging. *IEEE Trans. Ultrason., Ferroelect., Freq. Contr.*, 50:987–1001, 2003.

[18] Jeremy Bercoff, Mickael Tanter, and Mathias Fink. Supersonic shear imaging: A new technique for soft tissue elasticity mapping. *IEEE Trans. Ultrason., Ferroelect., Freq. Contr.*, 51:396–409, 2004.

[19] M. E. Anderson and G. E. Trahey. A seminar on k-space applied to medical ultrasound, 2000.

[20] A. Nguyen-Dinh, L. Ratsimandresy, P. Mauchamp, R. Dufait, A. Flesch, and M. Lethiecq. High frequency piezo-composite transducer array designed for ultrasound scanning applications. In *IEEE Ultrason. Symp.*, pages 943–947, 1996.

[21] T.A. Ritter, K. K. Shung, J. Cannata, and T. R. Shrout. High frequency ultrasound arrays for medical imaging. In *IEEE Ultrason. Symp.*, pages 1261–1264, 2000.

[22] R. Liu, K. A. Harasiewicz, and F. S. Foster. Interdigital pair bonding for high frequency (20-50 MHz) ultrasonic composite transducers. *IEEE Trans. Ultrason., Ferroelect., Freq. Contr.*, 48(1):299–306, January 2001.

[23] E. Lacaze, S. Michau, and P. Mauchamp. 20 MHz ultrasound array for medical imaging: from design to image evaluation. In *IEEE Ultrason. Symp.*, pages 1139–1142, 2001.

[24] T. Ritter, T. R. Shrout, R. Tutwiler, and K. K. Shung. A 30 MHz piezo-composite ultrasound array for medical imaging applications. *IEEE Trans. Ultrason., Ferroelect., Freq. Contr.*, 49(2):217–230, February 2002.

[25] J. M. Cannata, J. A. Williams, Q. Zhou, T. A. Ritter, and K. K. Shung. Development of a 35-MHz piezo-composite ultrasound array for medical imaging. *IEEE Trans. Ultrason., Ferroelect., Freq. Contr.*, 53(1):224–236, January 2006.

[26] W. Hackenberger, S. Kwon, and P. Rehrig. 2-2 PZT-polymer composites for high frequency (>20 MHz) ultrasound transducers. In *IEEE Ultrason. Symp.*, pages 1221–1224, 2002.

[27] S. Michau, P.Mauchamp, and R. Dufait. Piezocomposite 30 MHz linear array for medical imaging: design challenges and performances evaluation of a 128 elements array. In *IEEE Ultrason. Symp.*, pages 898–901, 2004.

[28] D. T. Yeh, O. Oralkan, A. S. Ergun, X. Zhuang, I. O. Wygant, and B. T. Khuri-Yakub. High-frequency CMUT arrays for high-resolution medical imaging. In *Proc. SPIE Med. Imag.*, volume 5750, pages 87–98, April 2005.

[29] E. S. Ebbini, H. Yao, and A. Shrestha. Dual-mode ultrasound phased arrays for image-guided surgery. *Ultrasonic Imaging*, 28:201–220, 2006.

[30] J. Shen and E. S. Ebbini. Filter-based coded-excitation system for high-speed ultrasonic imaging. *IEEE Trans. Med. Imag.*, 17(6):923–934, 1998.

[31] R. Y. Chiao and X. Hao. Coded excitation for diagnostic ultrasound: A system developer's perspective. *IEEE Trans. Ultrason., Ferroelect., Freq. Contr.*, 52(2):160–170, February 2005.

[32] B. Haider, P. A. Lewin, and K. E. Thomenius. Pulse elongation and deconvolution filtering for medical ultrasonic imaging. *IEEE Trans. Ultrason., Ferroelect., Freq. Contr.*, 45(1):98–113, January 1998.

[33] M. Vogt and H. Ermert. In vivo ultrasound biomicroscopy of skin: Spectral system characteristics and inverse filtering optimization. *IEEE Trans. Ultrason., Ferroelect., Freq. Contr.*, 54(8):1551–1559, August 2007.

[34] T. Misaridis and J. A. Jensen. Use of modulated excitation signals in medical ultrasound. part I: basic concepts and expected benefits. *IEEE Trans. Ultrason., Ferroelect., Freq. Contr.*, 52(2):177–191, February 2005.

[35] J. Shen and E. S. Ebbini. A new coded-excitation ultrasound imaging system – part I: basic principles. *IEEE Trans. Ultrason., Ferroelect., Freq. Contr.*, 43(1):131–140, 1996.

[36] H. Akaike. Block Toeplitz matrix inversion. *SIAM J. Appl. Math.*, 24(2):234–241, March 1973.

[37] W. F. Trench. An algorithm for the inversion of finite Toeplitz matrices. *J. Soc. Indust. Appl. Math.*, 12(3):515–522, September 1964.

[38] S. Zohar. Toeplitz matrix inversion: the algorithm of W. F. Trench. *J. Assoc. Comput. Mach.*, 16:592–601, October 1969.

[39] R. M. Gray. *Toeplitz and circulant matrices: A review.* Now Publishers, Norwell, Massachusetts, 2000.

[40] N. K. Bose and K. J. Boo. Asymptotic eigenvalue distribution of block-Toeplitz matrices. *IEEE Trans. Inform. Theory*, 44(2):858–861, March 1998.

[41] P. A. Voois. A theorem on the asymptotic eigenvalue distribution of Toeplitz-block-Toeplitz matrices. *IEEE Trans. Signal Processing*, 44(7):1837–1841, July 1996.

[42] T. DE Mazancourt and D. Gerlic. The inverse of a block-circulant matrix. *IEEE Trans. Antennas Propagat.*, AP-31:808–810, September 1983.

[43] J. A. Jensen. Field II program.

[44] N.T. Sanghvi, K. Hynynen, and F.L. Lizzi. New developments in therapeutic ultrasound. *IEEE Eng. Med. Biol. Mag.*, pages 83 – 92, November 1996.

[45] N. T. Sanghvi, F. J. Fry, R. Bihrle, et al. Noninvasive surgery of prostate tissue by high-intensity focused ultrasound. *IEEE Trans. Ultrason., Ferroelect., Freq. Contr.*, 43(6):1099–1110, 1996.

[46] C. M. Tempany, E. A. Stewart, N. McDannold, B. J. Quade, F. A. Jolesz, and K. Hynynen. MR imaging-guided focused ultrasound surgery of uterine leiomyomas: a feasibility study. *Radiology*, 226:897 – 905, November 2003.

[47] J. Poorter, C. Wagter, Y. Deene, C. Thomsen, F. Stahlberg, and E. Achten. Noninvasive MRI thermometry with the proton resonance frequency (PRF) method: In vivo results in human muscle. *Magn. Reson. Med.*, 33:74 – 81, 1995.

[48] R. Seip and E. Ebbini. Non-invasive estimation of tissue temperature response to heating fields using diagnostic ultrasound. *IEEE Trans. Biomed. Eng.*, 42:828–839, Aug 1995.

[49] R. Moreno, C. Damianou, and N. Sanghvi. Tissue temperature estimation in-vivo with pulse-echo ultrasound. In *IEEE Ultrason. Symp.*, pages 1225–1229, 1995.

[50] C. Simon, P. VanBaren, and E. S. Ebbini. Combined imaging and therapy with piezocomposite phased arrays. In *IEEE Ultrason. Symp.*, volume 2, pages 1555–1558, October 1998.

[51] B. Fallone, P. Moran, and E. Podgorsak. Noninvasive thermometry with a clinical X-ray scanner. *Med. Phys.*, 9:715–721, 1982.

[52] P. Meaney, K. Paulsen, A. Hartov, and R. Crane. Initial in vivo experience with EIT as a thermal estimator during hyperthermia,. *Ultrasound Med. Biol.*, 12:573–591, 1996.

[53] J.Y. Chapelon, D. Cathignol, C. Cain, E. Ebbini, J.U. Kluiwstra, O. Sapozhikov, G. Fleury, R. Berriet, L. Cupin, , and J.L. Guy. New piezoelectric transducers for therapeutic ultrasound. *Ultrasound Med. Biol.*, pages 153 – 159, 2000.

[54] M. Pernot, R. Berriet, J.-F. Aubry, O. Le Baron, M. Tanter, G. Fleury, L. Chupin, L. Gallet, and M. Fink. High power density prototype for high precision transcranial therapy. In *Proc. of the 3rd Int. Symp. on Therapeutic Ultrasound*, volume 1, pages 405 – 410, 2003.

[55] K. Hynynen and J. Sun. Trans-skull ultrasound therapy: The feasibility of using image-derived skull thickness information to correct the phase distortion. *IEEE Trans. Ultrason., Ferroelect., Freq. Contr.*, 46(5):752–755, May 1999.

[56] K. Ishida, J. Kubota, T. Mitake, R.F. Carlson, R. Seip, N.T. Sanghvi, K. Sadaki T. Azuma, K. Kawabata, and S. Umemura. Development and animal experiment of variable focusing HIFU syatem for prostate cancer treatment. In *Proc. of the 3rd Int. Symp. on Therapeutic Ultrasound*, volume 1, pages 382 – 387, 2003.

[57] R. Seip, W. Chen, J. Tavakkoli, L.A. Frizzell, and N.T. Sanghvi. High-intensity focused ultrasound (HIFU) phased arrays: Recent developments in transrectal transducers and driving electronics. In *Proc. of the 3rd Int. Symp. on Therapeutic Ultrasound*, volume 1, pages 423 – 428, 2003.

[58] L. Curiel, F. Chavrier, R. Souchon, A. Birer, and J. Y. Chapelon. 1.5-D high intensity focused ultrasound array for non-invasive prostate cancer surgery. *IEEE Trans. Ultrason., Ferroelect., Freq. Contr.*, 49(2):231–242, February 2002.

[59] R.W. Martin, S. Vaezy, and E.Y. Chi. Investigation of HIFU produced emulsion for acoustic hemostasis. In *Proc. of the 3rd Int. Symp. on Therapeutic Ultrasound*, volume 1, pages 351 – 356, 2003.

[60] G. Fleury, R. Berriet, O. Le Baron, and B. Huguenin. New piezocomposite transducers for therapeutic ultrasound. In *Proc. of the 2nd Int. Symp. on Therapeutic Ultrasound*, volume 1, pages 428 – 436, 2002.

[61] E. S. Ebbini, J. C. Bischof and J. E. Coad. Lesion formation and visualization using dual-mode ultrasound phased arrays. In *IEEE Ultrason. Symp.*, volume 2, pages 1351–1354, October 2001.

[62] I. Makin, T.D. Mast, P. Barthe, and M. Slayton. B-scan imaging and thermal lesion monitoring using miniaturized dual-functionality ultrasound arrays. In *IEEE Ultrason. Symp.*, volume 3, pages 1788–1791, August 2004.

[63] B. Guillaume, R. Berriet, C. Lafon, G. Fleury, D. Cathignol, and J.-Y. Chapelon. Dual mode transducer for ultrasound monitored thermal therapy. In *Proc. of the 5th Int. Symp. on Therapeutic Ultrasound*, volume 1, pages 390–394, 2005.

[64] F. Marquet, M. Pernot, J.F. Aubry, M. Tanter, G. Montaldo, and M. Fink. In vivo noninvasive motion tracking and correction in high intensity focused ultrasound. In *Proc. of the 28th Annual Int. Conference of the IEEE Eng. in Med. and Biol. Soc.*, volume 1, pages 688 – 691, 2006.

[65] A. Zaitsev, S. Raymond, J. Thierman, J. Juste, and K. Hynynen. Focused ultrasound thermal surgery, imaging, and elastometry using the same phased array: Feasibility study. In *IEEE Ultrason. Symp.*, volume 1, pages 2231–2234, August 2004.

[66] H. Yao and E. S. Ebbini. Dual-mode ultrasound phased arrays for imaging and therapy. In *IEEE Int. Symp. on Biomed. Imag.*, volume 1, pages 25–28, April 2004.

[67] H. Yao, R. Griffin and E. S. Ebbini. Noninvasive localized ultrasonic measurement of tissue properties. In *IEEE Ultrason. Symp.*, volume 1, pages 724–727, August 2004.

[68] E. Ebbini. *Deep Localized Hyperthermia with Ultrasound Phased Arrays Using the Pseudoinverse Pattern Synthesis Method.* PhD thesis, University of Illinois, 1990.

[69] Y.Y. Botros, E.S. Ebbini, and J.L. Volakis. Two-step hybrid virtual array-ray (var) technique for focusing through the rib cage. *IEEE Trans. Ultrason., Ferroelect., Freq. Contr.*, 45:989 – 1000, July 1998.

[70] Y. Wan and E. S. Ebbini. Enhanced resolution of dual-mode ultrasound arrays using coded excitation. In *IEEE Int. Symp. on Biomed. Imag.*, pages 1128–1131, April 2007.

[71] H. Yao and E. S. Ebbini. Imaging with large-aperture arrays with heterogeneous directive elements. In *IEEE Ultrason. Symp.*, volume 2, pages 1243–1246, October 2003.

[72] B. Otteson and E. S. Ebbini. On the design of dual-mode ultrasound arrays for imaging and therapy. In *Proc. of the 5th Int. Symp. on Therapeutic Ultrasound*, volume 1, pages 430–434, 2005.

[73] J.A. Jensen and N.B. Svendsen. Calculation of pressure fields from arbitrarily shaped, apodized, and excited ultrasound transducer. *IEEE Trans. Ultrason., Ferroelect., Freq. Contr.*, 39:262–267, March 1992.

[74] C. Simon, I. Elbakri, J. Shen, T. Hall and E. S. Ebbini. Combined ultrasound image guidance and therapy using a therapeutic phased array. *Medical Imaging*, 3341:89–98, May 1998.

[75] A. W. Rihaczek. Radar waveform selection - a simplified approach. *IEEE Trans. Aerosp. Electron. Syst.*, AES-7(6):1078–1086, November 1971.

[76] M. O'Donnell and Y. Wang. Coded excitation for synthetic aperture ultrasound imaging. *IEEE Trans. Ultrason., Ferroelect., Freq. Contr.*, 52(2):171–176, February 2005.

[77] G. Montaldo, J.-F. Aubry, M. Tanter, and M. Fink. Spatio-temporal coding in complex media for optimum beamforming: the iterative time-reversal approach. *IEEE Trans. Ultrason., Ferroelect., Freq. Contr.*, 52(2):220–230, February 2005.

[78] CIRS model 55 3D contrast phantom.

[79] R. F. Wagner, M. F. Insana, and S. W. Smith. Fundamental correlation lengths of coherent speckle in medical ultrasonic images. *IEEE Trans. Ultrason., Ferroelect., Freq. Contr.*, 35(1):34–44, January 1988.

[80] D. M. Thiboutot. Dermatological applications of high-frequency ultrasound. In *Proc. SPIE Med. Imag.*, volume 3664, pages 7–16, 1999.

[81] G. B. Jemec, M. Gniadecka, and J. Ulrich. Ultrasound in dermatology. part I. high frequency ultrasound. *Eur. J. Dermatol.*, 10(6):492–497, August 2000.

[82] D. Liu and E. S. Ebbini. Viscoelastic property measurement in thin tissue constructs using ultrasound. *IEEE Trans. Ultrason., Ferroelect., Freq. Contr.*, 55(2):368–383, February 2008.

[83] C. J. Pavlin, K. A. Harasiewicz, M. D. Sherar, and F. S. Foster. Clinical use of ultrasound biomicroscopy. *Ophthalmology*, 98(3):287–295, March 1991.

[84] D. T. Yeh, O. Oralkan, I. O. Wygant, M. O'Donnell, and B. T. Khuri-Yakub. 3D ultrasound imaging using a forward-looking CMUT ring array for intravascular/intracardiac applications. *IEEE Trans. Ultrason., Ferroelect., Freq. Contr.*, 53(6):1202–1210, June 2006.

[85] S. E. Nissen and P. Yock. Intravascular ultrasound: novel pathophysiological insights and current clinical applications. *Circulation*, 103(4):604–616, 2001.

[86] J. L. Evans, K. H. Ng, M. J. Vonesh, B. L. Kramer, S. N. Meyers, T. A. Mills, B. J. Kane, W. N. Aldrich, Y. T. Jang, and P. G. Yock. Arterial imaging with a new forward-viewing intravascular ultrasound catheter, I. initial studies. *Circulation*, 89:712–717, 1994.

[87] K. H. Ng, J. L. Evans, M. J. Vonesh, S. N. Meyers, T. A. Mills, B. J. Kane, W. N. Aldrich, Y. T. Jang, P. G. Yock, and M. D. Rold. Arterial imaging with a new forward-viewing intravascular ultrasound catheter, II. three-dimensional reconstruction and display of data. *Circulation*, 89:718–723, 1994.

[88] M. R. Neidert and R.T. Tranquillo. Tissue engineered valves with commissural alignment. *Tissue Eng.*, 12(4):891–903, April 2006.

[89] J. B. Liu and B. B. Goldberg. Endoluminal vascular and nonvascular sonography: past, present, and future. *AJR Am. J. Roentgenol.*, 165(4):765–774, October 1995.

[90] H. K. W. Kim, P. S. Babyn, K. A. Harasiewicz, K. P. H. Pritzker, and F. S. Foster. High resolution imaging of articular cartilage using ultrasound biomicroscopy. *J. Orthopaed Res.*, 13:963–970, 1995.

[91] A. Saied, E. Cherin, H. Gaucher, P. Laugier, P. Gillet, J. Floquet, P. Netter, and G. Berger. Assessment of articular carttilage and subchondral bone: subtle and progressive changes in experimental osteoarthritis using 50 MHz echography in vitro. *J. Bone Min. Res.*, 12:1378–1386, 1997.

[92] D. H. Turnbull, T. S. Bloomfield, F. S. Foster, and A. L. Joyner. Ultrasound backscatter microscope analysis of early mouse embryonic brain development. In *Proc. Nat. Acad. Sci*, volume 92, pages 2239–2243, 1995.

[93] D. H. Turnbull, J. A. Ramsay, G. S. Shivji, T. S. Bloomfield, L. From, D. N. Sauder, and F. S. Foster. Ultrasound biomicroscope analysis of mouse melanoma progression. *Ultrasound in Med. & Biol.*, 22:845–853, 1996.

[94] C. Daft, P. Wagner, B. Bymaster, S. Panda, K. Patel, and I. Ladabaum. cMUTs and electronics for 2D and 3D imaging: monolithic integration, in-handle chip sets and system implications. In *IEEE Ultrason. Symp.*, volume 1, pages 463–474, September 2005.

[95] Ultrasonix RP system.

[96] H. Lee. *High frequency ultrasound for characterizing the tissue engineered heart valve*. PhD thesis, University of Minnesota, 2005.

[97] Yayun Wan and E. S. Ebbini. A post-beamforming 2d pseudoinverse filter for coarsely sampled ultrasound arrays. In *IEEE Ultrason. Symp.*, pages 21–24, October 2007.

[98] CIRS Model 040.

[99] Beatrice Hoffmann. *Ultrasound Guide for Emergency Physicians – An Introduction*. Dover Publications, New York, second edition, 2008.

[100] Y. Wan and E. S. Ebbini. A post-beamforming 2d pseudoinverse filter for coarsely sampled ultrasound arrays. *IEEE Trans. Ultrason., Ferroelect., Freq. Contr.*, 56(9):1888–1902, September 2009.

[101] Y. Wan and E. S. Ebbini. 2d filter design for the reduction of beamforming artifacts in coarsely-sampled imaging apertures. In *IEEE Ultrason. Symp.*, pages 483–486, 2008.

[102] C.D. Ainsworth, C.C. Blake, A Tamayo, V. Beletsky, A. Fenster, and J.D. Spence. 3D ultrasound measurement of change in carotid plaque volume - A tool for rapid evaluation of new therapies. *Stroke*, 36(9):1904–1909, SEP 2005.

[103] D.A. Steinman and C.A. Taylor. Flow imaging and computing: Large artery hemodynamics. *ANNALS OF BIOMEDICAL ENGINEERING*, 33(12):1704–1709, DEC 2005.

[104] C.A. Figueroa, S. Baek, C.A. Taylor, and J.D. Humphrey. A computational framework for fluid-solid-growth modeling in cardiovascular simulations. *Computer Methods in Applied Mechanics and Engineering*, 198(45-46):3583 – 3602, 2009.

[105] C.A. Taylor and J.D. Humphrey. Open problems in computational vascular biomechanics: Hemodynamics and arterial wall mechanics. *Computer Methods in Applied Mechanics and Engineering*, 198(45-46):3514 – 3523, 2009.

[106] Y. Wan, D. Liu, and E. S. Ebbini. Imaging vascular mechanics using ultrasound: Phantom and in vivo results. In *IEEE Int. Symp. on Biomed. Imag.*, pages 980–983, 2010.

[107] J.R. Blake, S. Meagher, K.H. Fraser, W.J. Easson, and P.R. Hoskins. A method to estimate wall shear rate with a clinical ultrasound scanner. *Ultrasound in Medicine and Biology*, 34(5):760–774, MAY 2008.

[108] J.K. Tsou, J. Liu, A.I. Barakat, and M.F. Insana. Role of ultrasonic shear rate estimation errors in assessing inflammatory response and vascular risk. *Ultrasound in Medicine and Biology*, 34(6):963–972, JUN 2008.

[109] R. Karimi, T. Zhu, B.E. Bouma, and M.R.K. Mofrad. Estimation of Nonlinear Mechanical Properties of Vascular Tissues via Elastography. *Cardiovascular Engineering*, 8(4):191–202, DEC 2008.

[110] W.F. Weitzel, K. Kim, D.W. Park, J. Hamilton, M. O'Donnell, T.J. Cichonski, and J.M. Rubin. High-Resolution Ultrasound Elasticity Imaging to Evaluate Dialysis Fistula Stenosis. *Seminars In Dialysis*, 22(1):84–89, JAN-FEB 2009.

[111] B. Dunmire, K. W. Beach, K. Labs, M. Plett, and D. E. Strandness. Cross-beam vector doppler ultrasound for angle-independent velocity measurements. *Ultrasound in Med. & Biol.*, 26:1213–1235, October 2000.

[112] Jean K. Tsou, Jie Liu, and Michael F. Insana. Modeling and phantom studies of ultrasonic wall shear rate measurements using coded pulse excitation. *IEEE Trans. Ultrason., Ferroelect., Freq. Contr.*, 53(4):724–734, April 2006.

[113] Wei-Ning Lee, Christopher M. Ingrassia, Simon D. Fung-Kee-Fung, Kevin D. Costa, Jeffrey W. Holmes, and Elisa E. Konofagou. Theoretical quality assessment of myocardial elastography with *In Vivo* validation. *IEEE Trans. Ultrason., Ferroelect., Freq. Contr.*, 54(11):2233–2245, November 2007.

[114] Jianwen Luo, Kana Fujikura, Leslie S. Tyrie, III M. David Tilson, and Elisa E. Konofagou. Pulse wave imaging of normal and aneurysmal abdominal aortas *In Vivo*. *IEEE Trans. Med. Imag.*, 28(4):477–486, April 2009.

[115] K. Hirata, M. Kawakami, and M. F. O'Rourke. Pulse wave analysis and pulse wave velocity – a reviw of blood pressure interpretation 100 years after korotkov. *Circulation Journal*, 70:1231–1239, 2006.

[116] W. W. Nichols and M. F. O'Rourke. *McDonald's Blood Flow in Arteries*. Hodder Arnold, New York, 2005.

[117] J. I. Davies and A. D. Struthers. Pulse wave analysis and pulse wave velocity: A critical review of their strengths and weaknesses. *Journal of Hypertension*, 21:463–472, 2003.

Appendix A

DMUA Transducer Design: A Simulation Study

A.1 Introduction

Several dual-mode ultrasound array (DMUA) systems are being investigated for potential use in image-guided surgery. In therapeutic mode, DMUAs generate pulsed or continuous-wave (CW) high-intensity focused ultrasound (HIFU) beams capable of generating localized therapeutic effects within the focal volume. In imaging mode, pulse-echo data can be collected from the DMUA elements to obtain B-mode images or other forms of feedback on the state of the target tissue before, during, and after the application of the therapeutic HIFU beam. Therapeutic and technological constraints give rise to special characteristics of therapeutic arrays. Specifically, DMUAs have concave apertures with low f-number values and are typically coarsely sampled using directive elements. These characteristics necessitate pre- and post-beamforming signal processing of echo data to improve the spatial and contrast resolution and maximize the image uniformity within the imaging field of view (IxFOV). We have recently developed and experimentally validated beamforming algorithms for concave large-aperture DMUAs with directive elements. Experimental validation was performed using a 1 MHz, 64-element, concave spherical aperture with 100 mm radius of curvature. The aperture was sampled in the lateral direction using elongated elements 1 $\lambda \times 33.3\ \lambda$ with 1.33 λ center-to-center spacing (λ is the wavelength). This resulted in f-number values of 0.8

and 2 in the azimuth and elevation directions, respectively. In this section, we present a new DMUA design approach based on different sampling of the shared concave aperture to improve image quality while maintaining therapeutic performance. A pulse-wave (PW) simulation model using a modified version of the Field II program is used in this study. The model is used in generating pulse-echo data for synthetic-aperture (SA) beamforming for forming images of a variety of targets, e.g., wire arrays and speckle-generating cyst phantoms. The PW simulation model is used to investigate the effect of transducer bandwidth as well as finer sampling of the concave DMUA aperture on the image quality. The results show that modest increases in the sampling density and transducer bandwidth result in significant improvement in spatial and contrast resolutions in addition to extending the DMUA IxFOV.

In addition to the wire imaging target defined in Section 3.5.3, tissue mimicking cyst phantoms are also simulated to assess improvements in contrast resulting from the simulated increase in the bandwidth and/or in the spatial sampling of the DMUA. All the cysts used in this study are 12-mm in diameter with no scatterers within the cyst. The surrounding tissue is simulated assuming a scatterer density of > 12 scatterers per resolution cell, i.e. Rayleigh scattering. The size of the speckle-generating region surrounding the cyst(s) was sufficiently large to produce the clutter components from all significant sidelobes of the imaging beams. For example, for a 12-mm cyst centered at the geometric center of the DMUA, the extent of the speckle-generating phantom was 50 mm and 140 mm in the axial and lateral directions, respectively. Due to the high computational cost, the cysts simulated in this study are two-dimensional. This was deemed to be sufficient for the preliminary results presented in this paper for a 1D DMUA. Future 1.5D and 2D DMUAs will be tested using more realistic 3D cyst targets.

A.2 Transducer Bandwidth

Increasing the operating fractional bandwidth, FBW, of the DMUA can be expected to bring about improvement in its imaging performance (as with any array system). In this section, we investigate the effect of bandwidth on the PSF and contrast ratio in imaging a variety of cyst phantoms. The modified Field II PW simulation model was used. A Gaussian impulse response model was assumed for the array elements with

a center frequency of 1 MHz. The bandwidth was varied from 40% to 90% with 10% increments.

In simulation, we used an impulse excitation and a Kaiser window (with a window parameter value of 5) for the aperture apodization. Figure A.1 shows 50-dB images of the PSF in a 50×140 mm^2 region centered at the geometric center for bandwidth values of 40% (a), 60% (b) and 80% (c). Figure A.1(d) shows a lateral profile of the PSF for the 40% case, which shows a pattern of near-end and far-end grating lobes due to the concave geometry of the DMUA [68]. The near-end grating lobes would have formed farther out for a planar array with the same f-number and element-to-element spacing. Both axial and lateral dimensions of the PSF are reduced with increased bandwidth indicating improved resolution. In addition, sidelobe levels are also reduced with increased bandwidth indicating improved dynamic range. These results are further quantified in Figure A.2. As expected, improvement in axial resolution is directly proportional to $1/FBW$ while the improvement in lateral resolution is much less dramatic. This can be explained by the shortening of the imaging pulse duration at increased bandwidth values, which directly affects the axial response at the geometric center. On the other hand, the spatial impulse response of this large-aperture array spreads quickly outside the geometric center. Therefore, the improved bandwidth indirectly improves the array impulse response outside the geometric center. The improved bandwidth reduces constructive interference at the sidelobes (grating lobes) and results in the reduction in their levels as shown in Figure A.2.

To further illustrate the effect of increased bandwidth on image quality, we formed images from simulated SA data from a phantom (40 mm in axial direction and 140 mm in lateral direction) with statistically random-distributed scatterers and a 12mm-diameter cyst. The noise level inside of the cyst visually illustrates the effect of the clutter and the size of the cyst gives a measure related to the resolution. In these simulations, we used uniform apodization in (3.2) without gain compensation. Figure A.3 shows 50-dB images of a 40×140 mm^2 region centered at the geometric focus. One can clearly see the improvement in geometric representation of the cyst with increased resolution as well as the reduction in clutter inside the cyst. In addition, the improvement in speckle cell size can also be visually appreciated. Figure A.4 gives a more quantitative

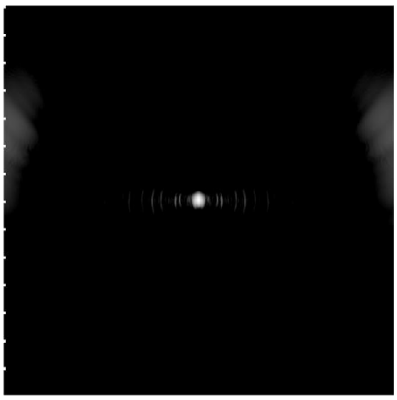

(a) 40% bandwidth

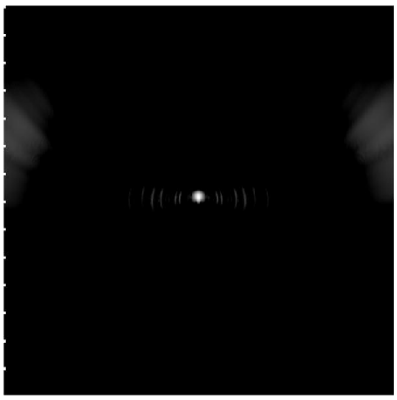

(b) 60% bandwidth

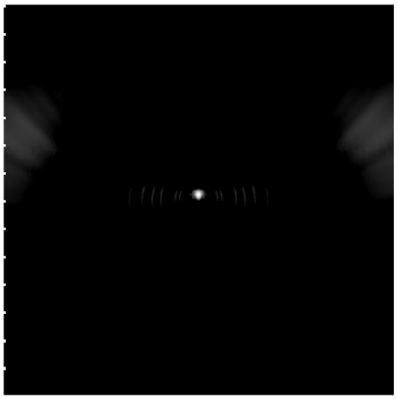

(c) 80% bandwidth

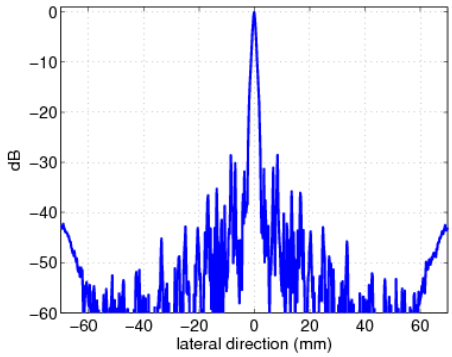

(d) Lateral PSF: 40%.

Figure A.1: Grayscale images (50 dB) of the PSF with 40%, 60% and 80% bandwidths, (a) - (c). A lateral profile of the 40% PSF is shown in (d) to demonstrate the sidelobe structure.

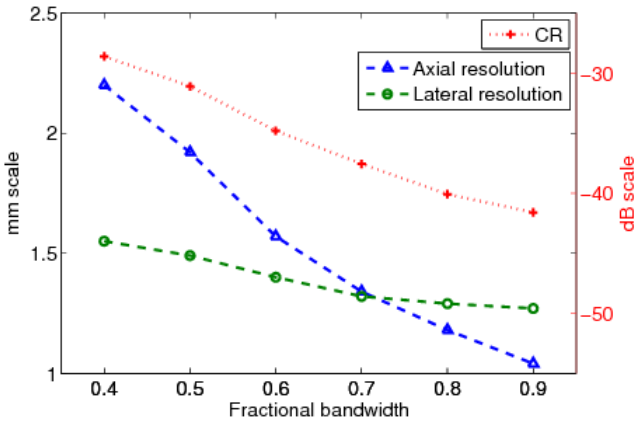

Figure A.2: Axial & lateral resolutions and lateral sidelobe level vs. bandwidth for the 1 MHz DMUA.

view of the improvement in image quality by plotting the log-compressed envelop data along an axial line going through the center of the cyst for different bandwidth levels. The figure shows clearly the improvement in cyst boundary definition and reduction of clutter with increased bandwidth. The cyst diameter was measured at -33 dB to be 8.0, 9.3, and 9.8 mm for 40%, 60%, and 80% bandwidth values, respectively. The contrast ratio was also evaluated to 21.2, 23.0, and 23.7 dB for 40%, 60%, and 80% bandwidth values, respectively. We have also performed cyst phantom images for a variety of cyst locations. Example (50 dB) images are shown in Figure A.5 and Figure A.6. The measured cyst diameters and CR values for the various cyst locations are summarized in Table A.1 and Table A.2, respectively.

A.3 Transducer Geometry

A.3.1 Lateral Sampling

The quality of the beam patterns of the DMUA can be improved by increasing the lateral sampling of the aperture. For the same aperture size, doubling the number of array elements results in element-to-element spacing of $0.6\bar{6}$-λ (instead of $1.3\bar{3}$-λ in the current prototype). This is expected to significantly reduce the grating lobes of the array. To quantify this improvement, we simulated the PSF of a 128-element array having the same geometry as the current DMUA, but with double the lateral sampling of the aperture and assuming a 40% bandwidth. The PSF of the 128-element array is shown in Figure A.7 (50 dB). Comparing this result with Figure A.1(a) shows a significant reduction in the near-end grating lobes and a dramatic reduction in the far-end grating lobes. This results in an overall improvement in the imaging dynamic range. Comparing the near-end grating lobes in Figure A.1(d) and Figure A.7(b), one can see a reduction in peak value from -28.6 to -35.4 dB. The far-end grating lobes are reduced by more than 20 dB.

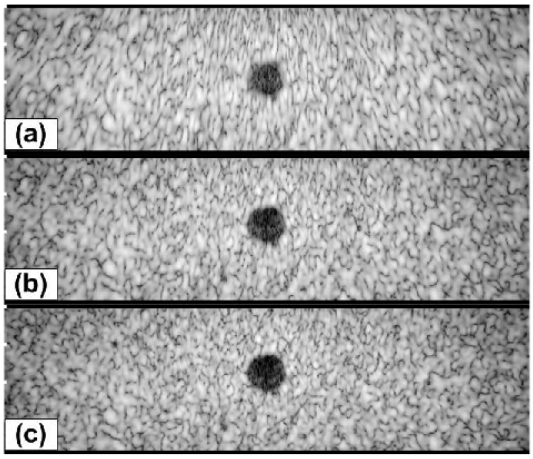

Figure A.3: Grayscale images (50 dB) of a simulated phantom with a cyst at [0 0 100] mm with radius = 6 mm; (a) 40% bandwidth; (b) 60% bandwidth; (c) 80% bandwidth.

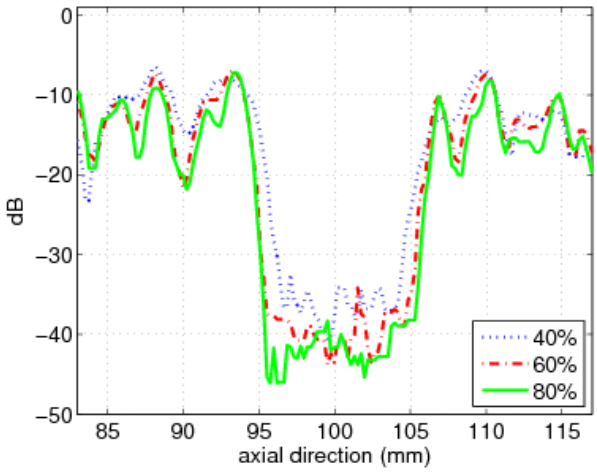

Figure A.4: Axial line plots (at x=0 mm) from the image data shown in Figure A.3(a) - (c).

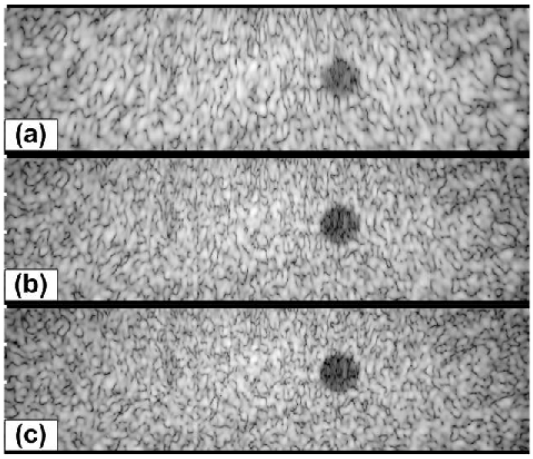

Figure A.5: Grayscale images (50 dB) of a simulated phantom with a cyst at [20 0 100] mm with radius = 6 mm; (a) 40% bandwidth; (b) 60% bandwidth; (c) 80% bandwidth.

	[0 0 70]	**[0 0 100]**	**[0 0 130]**	**[0 0 160]**	**[20 0 100]**
40%	8.4 mm	8.0 mm	8.4 mm	8.9 mm	7.1 mm
60%	8.9 mm	9.3 mm	9.3 mm	8.9 mm	9.3 mm
80%	9.8 mm	9.8 mm	9.8 mm	8.9 mm	9.5 mm

Table A.1: Cyst Diameter Measurement from Image Data.

	[0 0 70]	**[0 0 100]**	**[0 0 130]**	**[0 0 160]**	**[20 0 100]**
40%	15.7 dB	21.2 dB	22.0 dB	25.2 dB	17.9 dB
60%	18.7 dB	23.0 dB	23.6 dB	26.4 dB	18.9 dB
80%	20.4 dB	23.7 dB	23.6 dB	25.2 dB	19.1 dB

Table A.2: CR Values for Cyst Phantom.

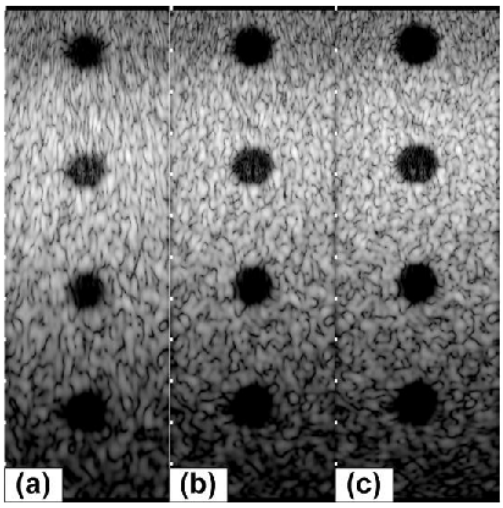

Figure A.6: Grayscale images (50 dB) of a simulated phantom with cysts at [0 0 70] mm, [0 0 100] mm, [0 0 130] mm and [0 0 160] mm with radius = 6 mm; (a) 40% bandwidth; (b) 60% bandwidth; (c) 80% bandwidth;

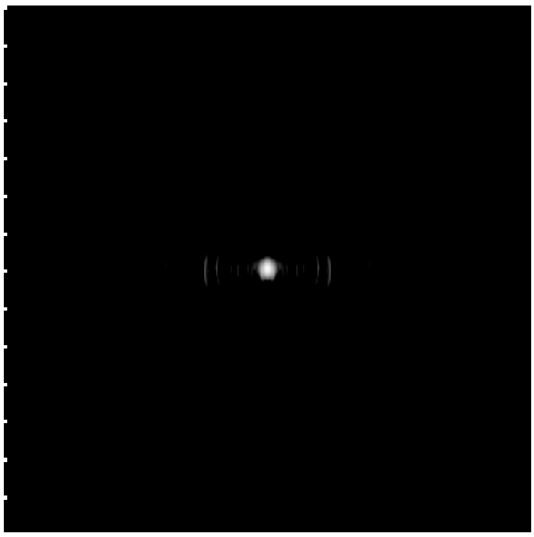

(a) Two-dimensional PSF

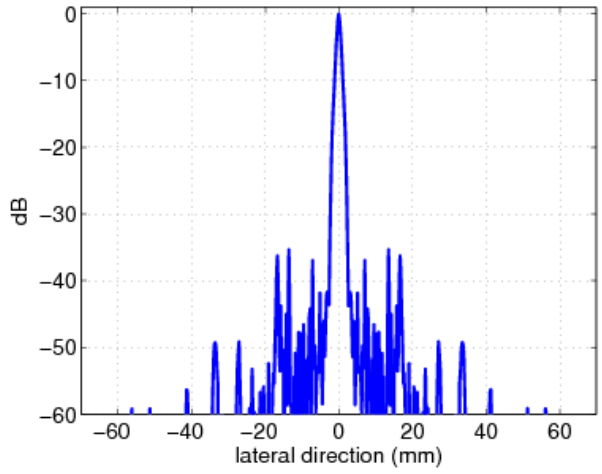

(b) Lateral Profile

Figure A.7: Grayscale image (50 dB) of the PSF of a 128-element, 40% bandwidth DMUA using the same aperture as the current DMUA.

	64-element	**128-element**
Axial resolution	2.2 mm	2.2 mm
Lateral resolution	1.55 mm	1.56 mm
Lateral sidelobe level	-28.6 dB	-35.4 dB

Table A.3: PSF Characteristics for 64- and 128-Element DMUAs.

A.3.2 Elevation f-number

The focusing intensity gain of our DMUA is proportional to the product of its lateral and elevation f-number values. The value of f-number = 2 in the elevation direction was chosen for practical purposes related to minimizing the impedance of the transducer elements as seen by the electrical driving circuit. The elevation focus has an obvious effect on the image quality obtained by the DMUA prototype. Specifically, the slice thickness is nearly 2 mm near the geometric center, but it is significantly larger in the prefocal and postfocal regions. A less obvious effect is the elongation of the geometric impulse response which could impact the array PSF in a manner that may be difficult to predict without the benefit of a good simulation model. The simulation model is an excellent tool to examine this effect on the array PSF and, consequently, on the image quality.

We have simulated the DMUA with the same geometry described in Section A.2 with 40% bandwidth, but varied the height of the elements in the elevation direction. We simulated a 64-element array with element height $h = 50$ mm (corresponding to the current prototype). In addition, we simulated an array with the same geometry but with $h = 25, 10$, and 5 mm. The results of this simulation are summarized in Table A.4, which shows that increasing the elevation f-number from 2 to 4 improves the lateral resolution (with Kaiser window apodization) and reduces the near-end grating lobes. This modest improvement partially validates our earlier design decision to fix the elevation f-number = 2, which was made without the benefit of PW simulation model. However, it also emphasizes the fact that careful modeling will be necessary to optimize the design of more complicated DMUAs. It should be noted that the slice thickness near the geometric center with $h = 25$ mm will be double that of the current DMUA (about 4 mm), but it will be more uniform throughout the *IxFOV*.

A.4 Modified DMUA Design for Improved Image Quality

The simulation results shown in Section A indicate that a more finely sampled aperture with f-number = 4 in the elevation direction (at the geometric focus) with $\approx$ 70% bandwidth offers improved imaging performance compared with the current prototype

	50 mm	**25 mm**	**10 mm**	**5 mm**
Axial resolution	2.2 mm	2.27 mm	2.28 mm	2.28 mm
Lateral resolution	1.55 mm	1.22 mm	1.2 mm	1.2 mm
Lateral sidelobe level	-28.6 dB	-32 dB	-32.2 dB	-32.2 dB

Table A.4: PSF Characteristics for 64-Element DMUA with Different Elevation Heights.

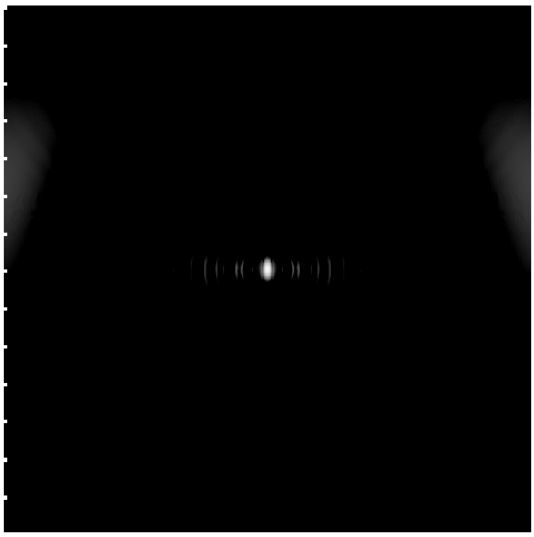

(a) Two-dimensional PSF

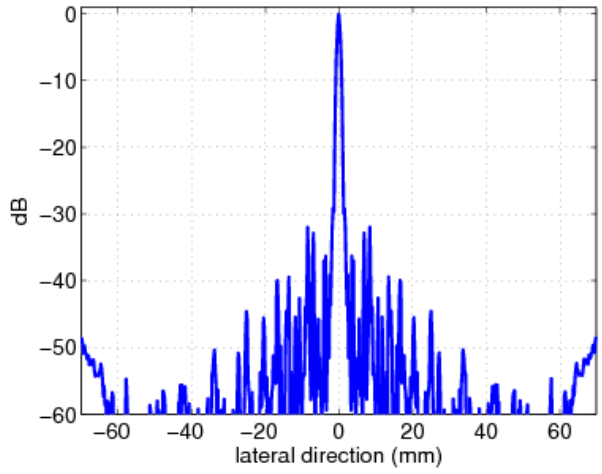

(b) Lateral Profile

Figure A.8: Grayscale image (50 dB) and a lateral profile of the PSF of a 64-element DMUA with element height, $h = 25$ mm (elevation f-number $= 4$).

geometry. For example, a DMUA can be designed with 128 × 4-element lattice by dividing each element in the current design into 2×4 subelements as shown in Figure A.9. In therapy mode, a group of 4×2 subelements can be connected to form 1 low-impedance element. This grouping results in a 64 × 1 array similar to the current prototype. This sub-element grouping scheme may be necessitated by the need to maintain a limited driver channel count and/or manage the impedance of the load for optimum operation. In imaging mode, 2 × 1 subelements (from the two center rows of elements in the elevation directions) can be connected to form one imaging element with $\approx \lambda/2$ width in the lateral direction and $\approx 8\lambda$ in the elevation direction. This grouping results in a 128 × 1 imaging array. This solution allows for the use of more finely sampled array to reduce grating lobes. In addition, the use of larger f-number in the elevation direction extends the *IxFOV* of the DMUA by shortening the geometric impulse responses of the array elements. Figure A.10 shows the PSF of the modified DMUA design with impulse excitation and Kaiser window apodization (with Kaiser window parameter = 5). Figure A.11 shows the image of the wire target array using the modified design (without gain compensation). The 50-dB dynamic range images of the PSF and wire-target array show clearly the reduction in grating lobes, increased target visibility away from the geometric center, and improved axial and lateral resolution compared with the exsiting prototype.

A.5 Conclusion

The use of dual mode ultrasound phased arrays in image-guided surgery is becoming a reality. This chapter presented simulation results for characterization of the imaging capabilities of a 1 MHz prototype DMUA. The simulation model was then used to evaluate the effect of varying DMUA design parameters (FBW and aperture sampling) on the PSF and the contrast ratio of cyst targets positioned at various locations within the IxFOV. Finally, based on this simulation study, we have proposed a modified DMUA design that results in significant enhancement in the imaging performance in terms of spatial and contrast resolution as well as expanded IxFOV. Using simple element

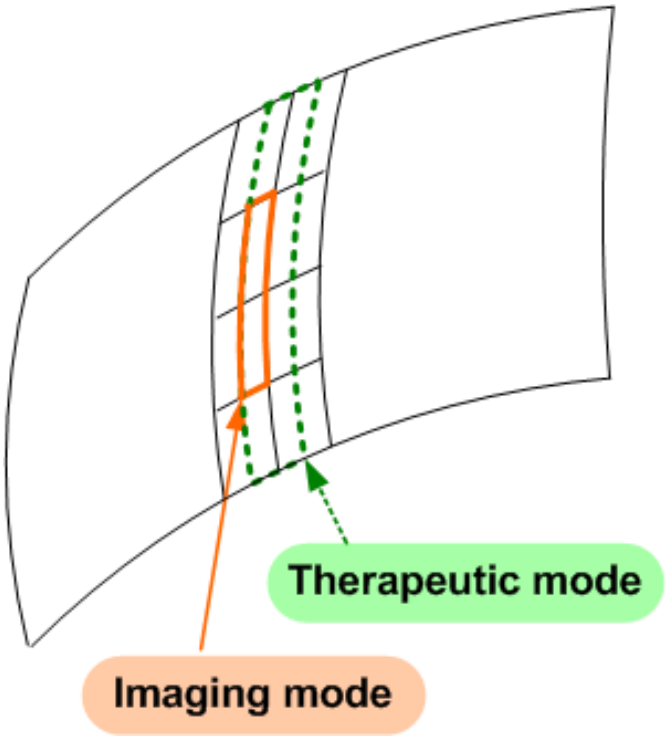

Figure A.9: Geometry of a modified DMUA: a 128 × 4-element array that can be configured as 64 × 1 array in therapy mode and 128 × 1 array in imaging mode.

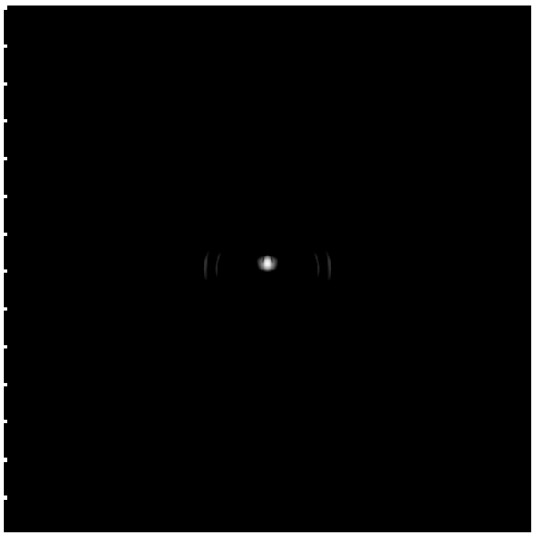

Figure A.10: Grayscale image (50 dB) of the point spread function for the modified DMUA design.

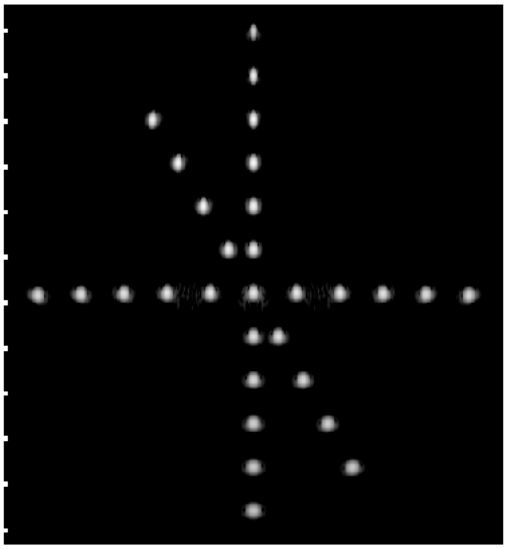

Figure A.11: Grayscale image (50 dB) of the wire target array using the modified DMUA design.

interconnection schemes in imaging and therapy modes, the modified DMUA can achieve this enhancement while simultaneously maintaining the therapeutic aperture sampling of the existing DMUA design that has been optimized for therapy. This implies that the improvements in imaging performance of the DMUA will not significantly compromise its predicted therapeutic performance.

Appendix B

Simultaneous Imaging Tissue Motion and Flow Velocity in Quantitative Vascular Imaging

B.1 Introduction

Vascular imaging is gaining increased attention not only as a means of detection of cariovascular diseases, but also for the evaluation of response to new antiatherosclerotic therapies [102]. Intravascular ultrasound (IVUS) has been shown to provide an effective tool in measuring the progression or regression of atherosclerotic disease in response to therapies. However, IVUS is invasive, potentially risky, and more expensive than noninvasive vascular imaging with ultrasound. Advanced imaging modes on ultrasound scanners have led to increased interest in imaging important quantities like wall shear rate (WSR) using Doppler [107] and tissue/wall motion [108–110] using speckle tracking. The tissue/wall mechanical properties may be good indicators of some sommon vascular diseases such as abdominal aortic aneurysm (AAA) the pulse-wave velocities of the aorta wall using speckle tracking. Recently, there has been increased interest in imaging flow in conjunction with computational fluid dynamic (CFD) modeling the evaluation of large artery hemodynamics [103–105]. In this context, modeling fluid-solid interfaces has been defined as a challenge area in vascular mechanics [105]. Imaging methods capable of

capturing both perivascular (and wall) tissue motion and deformations, together with fluid flow may be the key component in addressing this challenge.

Standard clinical ultrasound uses various Doppler techniques for One-dimensional (1D) blood flow imaging. The velocity measurements depend on the estimation of the angle between the direction of the blood flow and the direction of the beam. This angle dependence and aliasing artifact at high velocities are two major drawbacks for Doppler techniques. People has extended Doppler methods to 2-D such as vector Doppler [111] or combined 1D Doppler for flow imaging with 1D speckle tracking method for tissue imaging [112].

1D speckle tracking has been proposed for accurate estimation of the motion perpendicular to the probe. The axial motion can be obtained with high precision scale of sub-millimeter to tens of microns depending on the ultrasound frequency. The obtained motion information has been extensively used for applications such as elastography, temperature estimation etc [9, 82]. Naturally, the 1D speckle tracking method can be extended to 2-D or 3-D for a better tracking of the actual 3-D motion/flow. For example, 1D speckle tracking has been extended by recorrelating the 1D kernel in a 2D search for obtaining motion fields in 2D, and this method has been supported by aorta and myocardial results [113, 114]. The success of the 1D speckle tracking method is supported by the natural, high sampling data rate in the axial direction in ultrasound imaging. However at the same time, the sampling in the lateral direction (and elevation direction in 3-D) is much coarser compared to the axial direction. This is normally compensated by interpolation, which leads to another important consideration for 2-D/3-D speckle tracking: the high computational cost due to the correlation computation of the interpolated 2-D area or 3-D volume kernel. Therefore, minimizing the computational cost is essential for efficient implementation of multi-dimensional speckle tracking methods in real-time.

Two-dimensional (2D) speckle tracking and vector Doppler are being investigated by several groups as a potentially powerful method for the analysis of tissue motion and deformation, especially in vascular imaging applications [108–111]. In addition to the direct measurements and/or characterization of the vessel dynamics, these investigations may provide tissue displacement fields and underlying anatomical information suitable for important challenge areas such as computational fluid dynamics (CFD) [103–105].

We have proposed a 2D speckle tracking method [29] with subsample displacement estimation accuracy in both axial and lateral directions. The efficiency is obtained by minimal lateral interpolation compared to previously published methods, and this algorithm employs the true 2D complex cross correlation for obtaining the 2D motion information. In this study, we utilize this 2D phase-coupled speckle tracking method in conjunction with a motion-2D (M2D) imaging mode to provide sufficient frame rates for 2D vector displacement tracking. M2D imaging is implemented on a clinical scanner equipped with a research interface for controlling the imaging sequence and streamlining the RF data for performing 2D speckle tracking in the region of interest. Combining 2D speckle tracking with M2D mode imaging allows for fine displacement tracking in both lateral and axial directions. The resulting vector displacement fields are well suited for strain and shear strain calculations with minimum filtering and using relatively small tracking windows to maximize resolution. Therefore, obtaining data using the high frame rate (*e.g.* 300 frames per second) M2D imaging mode and processing the data using the 2D speckle tracking method make it possible to efficiently extract smooth and contiguous displacement fields and strain/sheer strain fields from the flow and surrounding tissue motion simultaneously either in controlled tissue-mimicking flow phantom experiment or human carotid artery *in vivo*. The resulting motion fields can be used for correctly registering the contour of the flow channel/blood vessel and showing the flow information direction, velocity etc., in addition, they provide detailed and instantaneous flow information at region of interest such as vessel area blocked by a plaque, which is obviously with diagnostic importance.

The remainder of this chapter is organized as follows. The 2D phase-coupled speckle tracking method is explained in Section B.2. In Section B.3, we present obtained flow & tissue displacement & strain fields evaluated in a tissue-mimicking flow phantom and *in vivo* in the carotid of a healthy volunteer using the 2D speckle tracking method. Finally, conclusions are given in Section B.4.

B.2 Phase-Coupled 2D Speckle Tracking

The phase-coupled 2D speckle tracking algorithm has been proposed in [29]. The method is based on the gradients of the magnitude and phase of 2D complex correlation in a

search region. The novelty of this approach is that it couples the phase and magnitude gradients near the correlation peak to determine its coordinates with subsample accuracy in both axial and lateral directions. This is achieved with a minimum level of lateral interpolation determined from the angles between the magnitude and phase gradient vectors on the sampled (laterally interpolated) 2D cross-correlation grid. The key result behind this algorithm is that the magnitude gradient vectors' final approach to the true peak is orthogonal to the zero-phase contour. This leads to a 2D robust projection on the zero-phase contour that results in subsample accuracy at interpolation levels well below those needed using previously proposed methods. A full description of the 2D phase-coupled approach is given in [29], including two implementations based on a geometric projection and constrained optimization. It is shown that estimated 2D vector displacement fields obtained using the phase-coupled technique display a full range of values covering the dynamic range without evidence of quantization. In comparison, a previously published method using 1D phase-projection after lateral interpolation produces severely quantized lateral displacement fields (at the same levels of interpolation as the 2D, phase-coupled method).

B.3 Results and Discussion

B.3.1 Data Acquisition

A Sonix RP (Ultrasonix, Canada) ultrasound scanner loaded with custom designed program is used for M2D pulse-echo data collection. Collected data is then streamlined to a controller PC through Gigabit Ethernet for realtime data processing. The data processing computer can easily handle the intensive computations required by high resolution (both spatial and temporal) speckle tracking and separable 2D post filtering by utilizing a many core GPU (nVIDIA, Santa Clara, CA). A linear array probe (LA14-5/38) was used to acquire all data shown in this paper. The center frequency of the transmit pulse on the probe was 7.5 MHz.

Experiments using the ATS Model 524 flow phantom and a Cole-Parmer MasterFlex roller pump were conducted to illustrate the displacement tracking in axial and lateral directions. M2D data was collected using the Sonix RP scanner at a frame rate of hundreds (*e.g.* 325 frames per second). Images of a 4-mm flow channel in the ATS

phantom were collected under controlled fluid flow with an appropriate speed setting of the MasterFlex pump to mimic typical blood flow rates (*e.g.* 336 ml/min) in carotid arteries. Cellulose microspheres where diluted in watter to produce linear scattering from the flow channel during data collection (pure water was also imaged as a control to determine the channel boundaries as a ground truth).

B.3.2 Strain Computation

Strain and shear strain calculations were performed using MATLAB's `gradient` command on the axial and lateral displacement fields obtained using the 2D speckle tracking algorithm. The strain and shear strain computations are followed by a simple Gaussian lowpass filter with size of 3×3 and standard deviation of 1, i.e. minimal post filtering of the strain and shear strain fields.

B.3.3 Experimental Phantom Result for 2D Speckle Tracking

We have imaged the 4-mm flow channel of the ATS Model 524 flow phantom using the LA14-5 probe. In the setup of viewing the cross section of the 4-mm channel, the tracking was targeted at the pulsation movements of the channel walls. As shown in Figure B.1(b), the displacement field clearly illustrates the wall movements (a shrinking movement at this instance) and maps the contour of the channel as given in the Figure B.1(a). The axial strain and the axial shear strain are computed and plotted as in Figure B.2, and the strain fields also give clear definition of the channel walls.

In the case of longitudinal view of the channel, the channel axis is set to be perpendicular to the beam axis, i.e. lateral flow. The displacement fields from the flow in the lateral direction and the pulsating channel wall in the axial direction are obtained from the 2-D phase-coupled speckle tracking algorithm with the M2D imaging and an instance of the motion fields are plotted in Figure B.3(b) and Figure B.3(a) respectively. At this instance, Figure B.3 shows the contraction of the channel wall from the axial displacement field and a mostly uniform flow to the right in the channel from the lateral displacement field. The contour of the lateral flow implies possible narrowing around

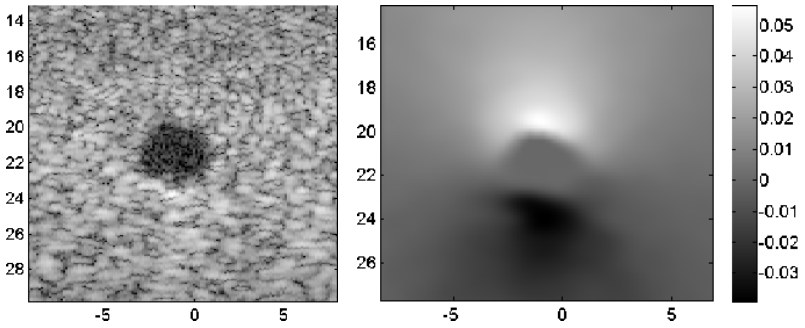

(a) (b)

Figure B.1: The cross sectional grayscale (50 dB) image (a) and the axial displacement field (b) of the 4-mm flow channel in the ATS phantom, the vertical coordinate is axial direction, the horizontal coordinate is lateral direction, both of the axises and color bar are in mm; therefore the displacements are between -39.2 μm and 56.5 μm.

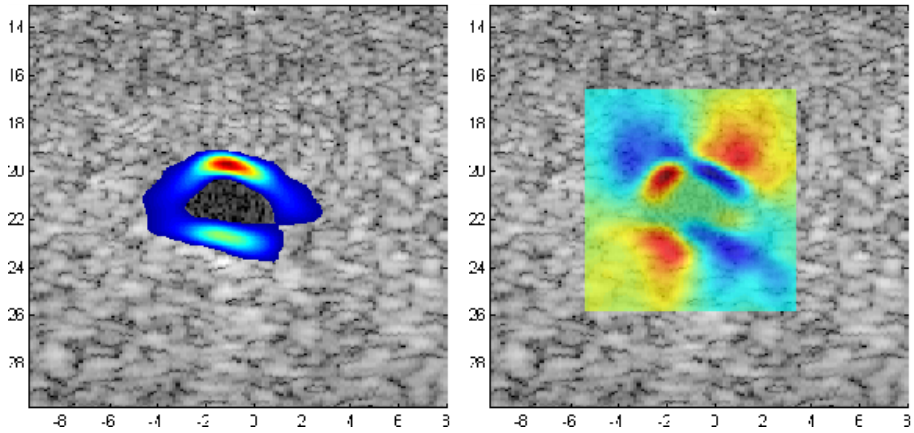

(a) Axial Strain. (b) Axial Shear Strain.

Figure B.2: The axial strain and axial shear strain of the 4-mm flow channel cross sectional walls.

the center of the flow channel which is not indicated by the B-mode image. The resulting strain and shear strain fields are shown in Figure B.4 and Figure B.5. One can see the smoothness of the strain fields which demonstrates the well-behaved nature of the displacement fields. At the same time, we can appreciate the clear demarcation between the channel and the surrounding tissue-mimicking material. Especially, Figure B.5(b) indicates potential usage of the lateral shear strain fields for detecting channel narrowing or blockage due to plaques built in the vessel walls.

The dynamics of the estimated vector flow field are illustrated in Figure B.6 which shows a plot of the channel diameter (obtained from the axial component at the channel walls) and the average lateral flow velocity in the channel for several cycles of pump operation. The average flow velocity is smoothed by a simple low pass filter. The result shows clearly the quasi-periodic nature of the observed flow velocity and the phase relationship between the diameter (pressure in the channel) and flow. The dynamic behavior of the lateral flow along the axis of the imaging beam (at a lateral distance of -3.2 mm) is illustrated by Figure B.7. One can see the smooth, well-behaved nature of the lateral displacement fields consistent with the quasi-periodic pattern shown in Figure B.6. It should be emphasized that the results shown in Figure B.7 are minimally processed, i.e. the continuity and the high SNR of the vector displacement estimation in the fluid and the surrounding tissue is a direct consequence of the proper application of the phase-coupled 2D speckle tracking method. The ability of being able to extract the periodic pattern due to the roller pump setup from both the channel wall and the flow verifies the capability of simultaneous tracking both tissue motion and flow with our approach.

B.3.4 *In Vivo* Experiment

We applied the phase-coupled 2D speckle tracking algorithm on the carotid artery *in vivo* data to characterize the tissue motion field and in the vicinity of the artery and the blood flow inside. The data was collected on a healthy volunteer at frame rates of 93 fps and 325 fps, respectively for the cross sectional view and the longitudinal view.

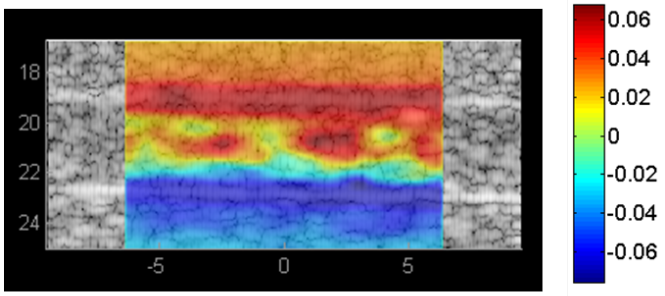

(a) Axial displacement.

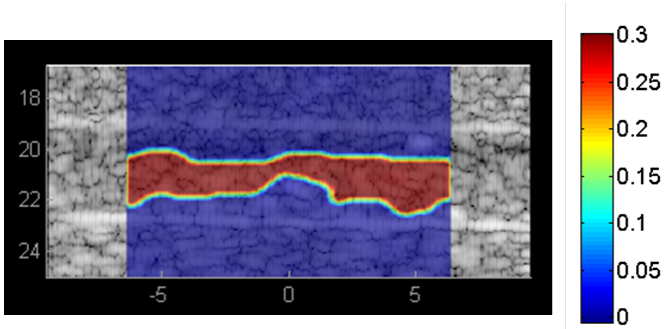

(b) Lateral displacement.

Figure B.3: The axial and lateral displacement fields from the flow phantom results are color-coded and overlaid on the B-mode gray scale images. Distances and displacements are given in mm.

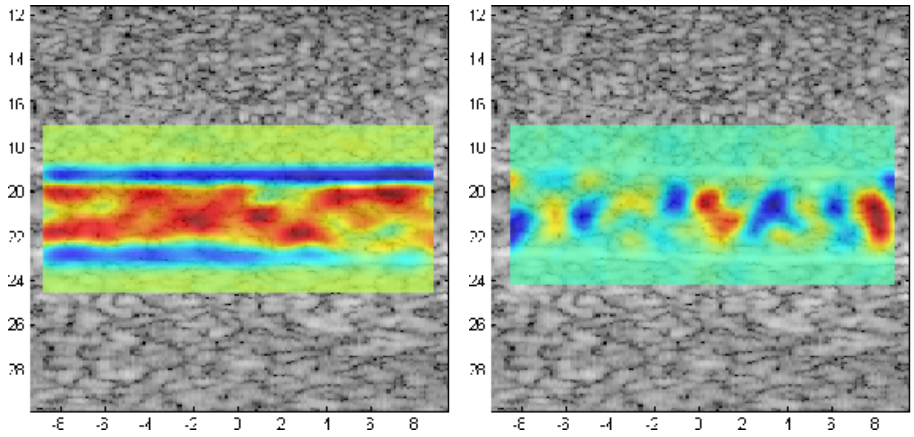

(a) Axial Strain. (b) Axial Shear Strain.

Figure B.4: The axial strain and axial shear strain of the 4-mm flow channel longitudinal walls.

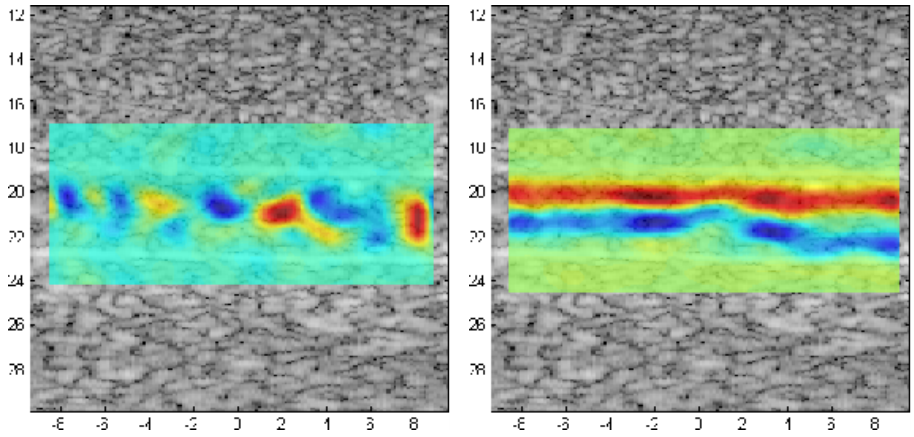

(a) Lateral Strain. (b) Lateral Shear Strain.

Figure B.5: The lateral strain and lateral shear strain of the 4-mm flow channel longitudinal walls.

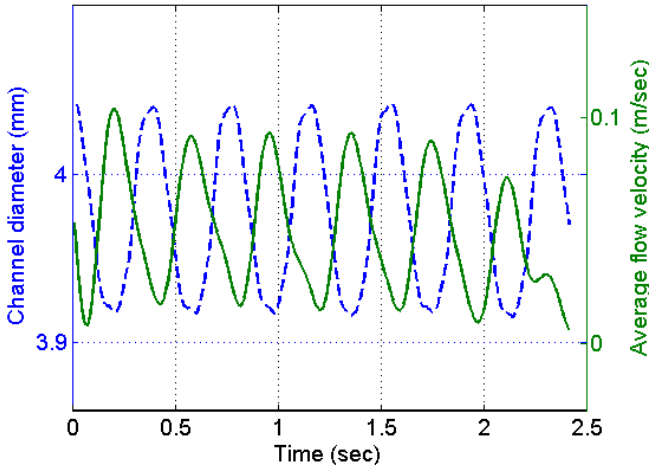

Figure B.6: The periodic average flow velocity obtained from the tracked fluid displacements within the 4-mm flow channel in the ATS phantom and the corresponding periodic channel diameter computed from the tracked channel wall displacements.

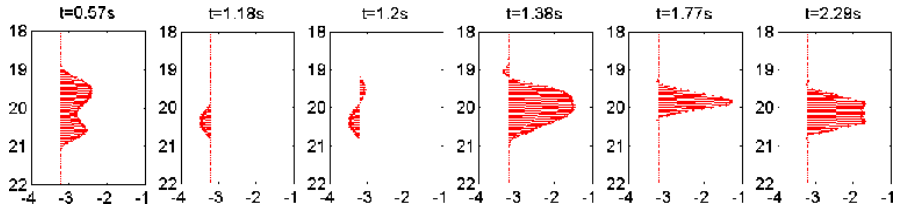

Figure B.7: The total displacement vector waveforms within the channel at different time instances.

When imaging the cross section of the carotid artery, the phase-coupled algorithm tracks the pulsation motion of the vessel wall in both the axial and lateral directions. As shown in Figure B.9, the 2D displacement vectors clearly illustrates the direction and magnitude of the tissue pulsation motion. For example, the algorithm tracked an expanding movement of the wall in both the axial direction as shown in Figure B.9(a) and the lateral direction as shown in Figure B.9(b). Both of the displacement field plots give clear definitions of the boundary of the vessel as shown in Figure B.8. The strains and shear strains in both axial and lateral directions are computed and plotted, respectively in Figure B.10 and Figure B.11.

A longitudinal view of the carotid artery was also obtained using the same imaging system and probe with M2D mode at a frame rate of 325. Figure B.12 illustrates the displacement fields in both axial and lateral directions of the carotid artery using the 2D speckle tracking method. The displacement fileds are color-coded and overlaid on the grayscal B-mode images of the carotid artery segment. The lateral displacement field in Figure B.12(a) gives a good visualization of the moving speckles formed by signals from blood cells; while at the same time, the axial displacement field in Figure B.12(b) clearly marks the vessel wall tissue position and corresponding motion strength. With the ability of tracking motion fields in two dimensions, the tissue motion and flow pattern can be obtained simultaneously with the ultrasound probe positioned at any angle to the tissue structure. Furthermore. the displacement fields are contiguous throughout the region of ineterest, allowing for the computation of the strain and shear strain fields shown in Figure B.13. The axial strain in Figure B.13(a) not only provides an indication of the vessel boundaries but also gives a good measurement of the thickness of the vessel wall. The axial sheer strain pattern in the vessel wall regrion in Figure B.13(b) also shed light on the pulse wave propagation. Local pulse wave velocity can be used for estimating the stiffness of arteries [114–117]. In addition, the lateral strain and the lateral sheer strain in Figure B.13(c) and Figure B.13(d) together with the axial strain and the axial sheer strain could be used for observing local blood clots, plaque and artery wall abnormaties.

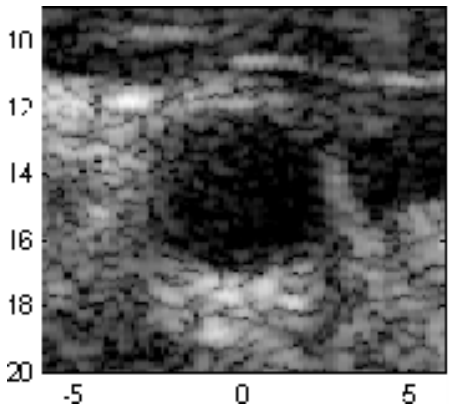

Figure B.8: The cross sectional grayscale (50 dB) image of the carotid artery, the vertical coordinate is axial direction, the horizontal coordinate is lateral direction, both are in mm.

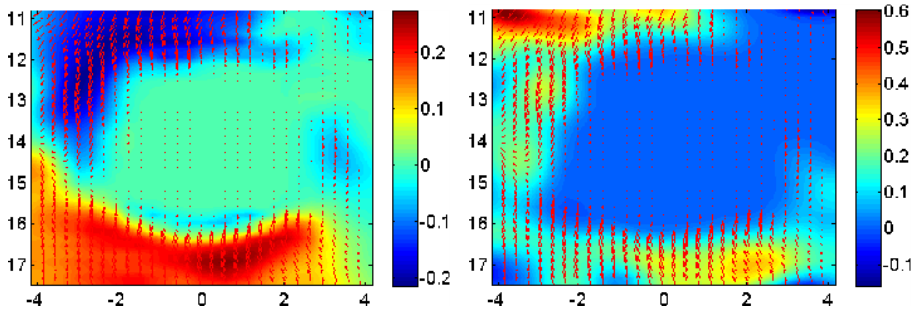

(a) Axial displacement field. (b) Lateral displacement field.

Figure B.9: The axial and lateral displacement fields of the carotid artery cross sectional view, the vertical coordinate is axial direction, the horizontal coordinate is lateral direction, both of the axises and color bar are in mm.

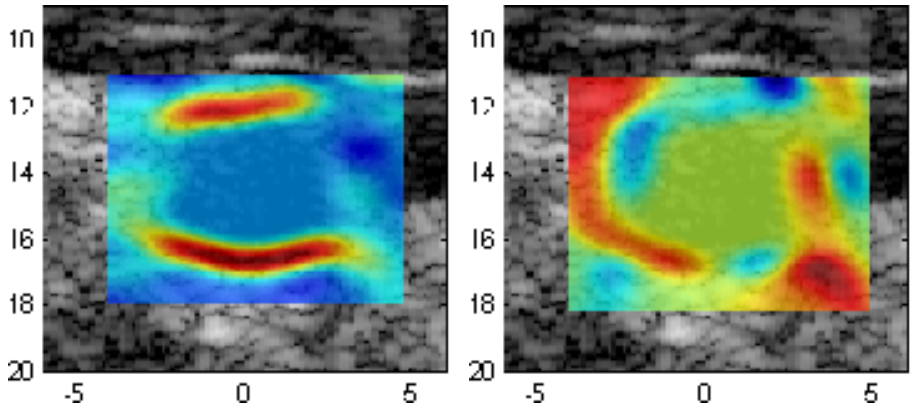

(a) Axial Strain. (b) Axial Shear Strain.

Figure B.10: The axial strain and axial shear strain of the carotid artery cross sectional vessel walls.

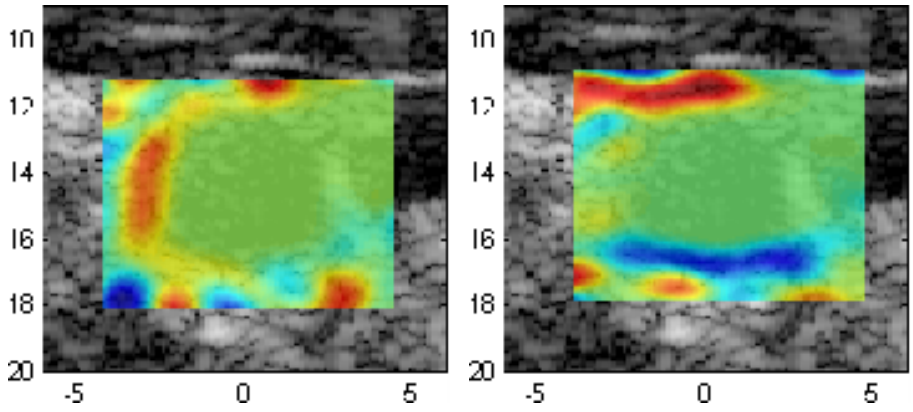

(a) Lateral Strain. (b) Lateral Shear Strain.

Figure B.11: The lateral strain and lateral shear strain of the carotid artery cross sectional vessel walls.

The pulsation pattern of the vessel wall motion and the blood flow can be best illustrated with the change of vessel diameter and average flow velocity plot in Figure B.14. The vessel diameter is obtained from the displacemnts of the upper and lower vessel walls, and the average flow velocity is obtained from the displacements of a small region in the channel. A simple band pass filter is used for eliminating artifacts and outside of band noise. As we expect, the diameter change shows a blood pressure wave-like pattern [116] and the local average flow velocity has a ECG-like waveform pattern. As a reference, the ECG signal for the same patient was taken also using the Sonix RP system, plotted in Figure B.15. These extracted waveform can be used as tools for local detection and staging of arterial diseases resulting in abnormal hemodynamics.

B.4 Conclusion

A new method for simultaneous imaging of flow velocity within vessels and their wall motion has been demonstrated in tissue-mimicking flow phantoms and *in vivo*. The results show that, at sufficiently high frame rates, speckle tracking methods produce well-behaved displacement estimates of both the tissue motion and flow in the vessel. These displacement fields are well suited for strain and shear strain calculations with minimum filtering. We have also demonstrated that time waveforms of flow velocity and pressure follow the quasi-periodic motion of the roller pump in the phantom experiments and ECG recordings from the human subject. Furthermore, the axial wall displacements (indicative of pressure) and average lateral flow velocity in the channel have a clear phase relationship. This indicates that our approach may be useful in obtaining the full dynamic motion fields suitable for solid-fluid interface modeling of vascular mechanics. It may also allow for noninvasive hemodynamic analysis for the detection and staging of vascular diseases.

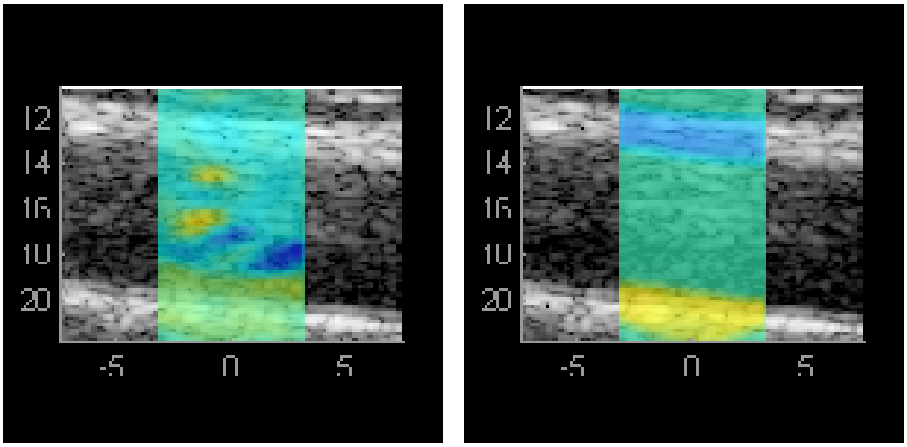

(a) Lateral displacement. (b) Axial displacement.

Figure B.12: The lateral and axial displacements of the carotid artery are color-coded and overlaid on the B-mode gray scale images.

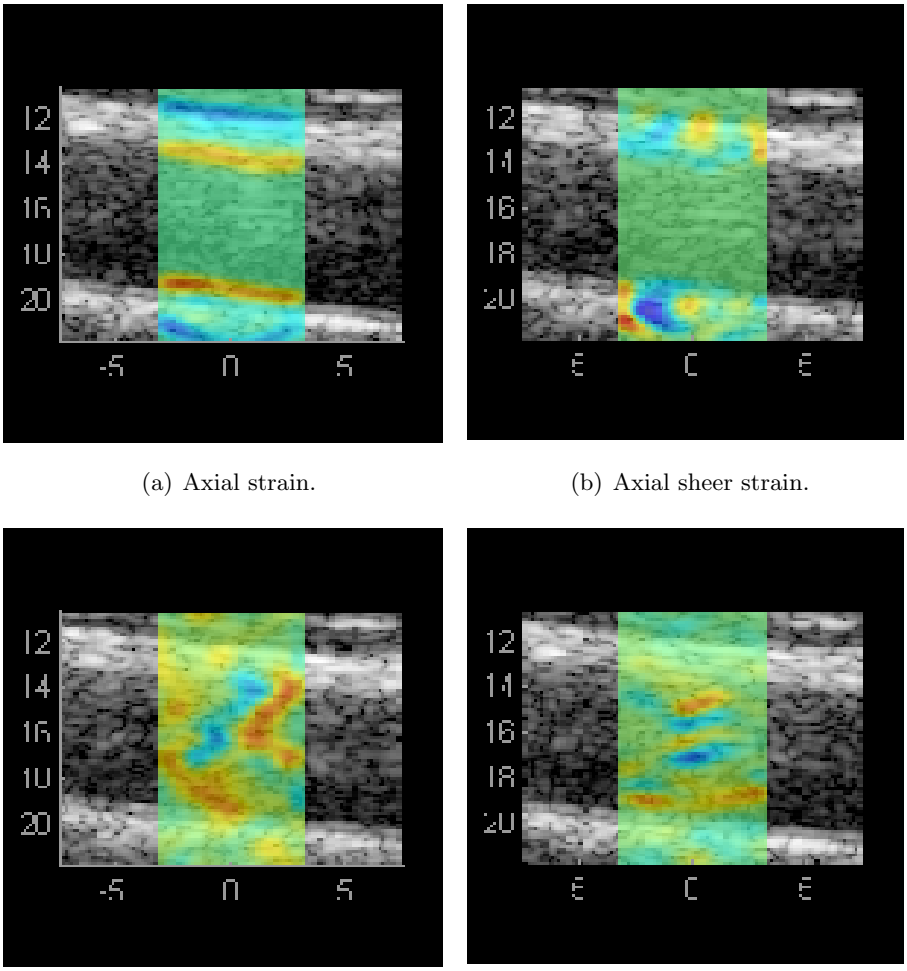

(a) Axial strain.

(b) Axial sheer strain.

(c) Lateral strain.

(d) Lateral sheer strain.

Figure B.13: The lateral and axial strains and sheer strains of the carotid artery are color-coded and overlaid on the B-mode images.

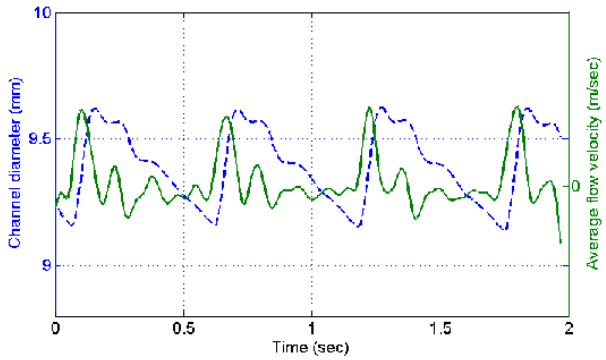

Figure B.14: The change of vessel diameter and average flow velocity obtained from local 2-dimensional displacement field.

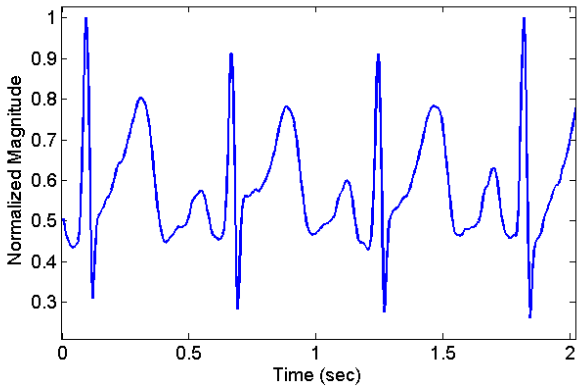

Figure B.15: The ECG signal from the same patient using the Sonix RP system.